Semiempirical Models of Organic Scintillator Response to Neutron Interactions on Hydrogen and Carbon

by

Mark Andrew Norsworthy

A dissertation submitted in partial fulfillment
of the requirements for the degree of
Doctor of Philosophy
(Nuclear Engineering and Radiological Sciences)
in the University of Michigan
2017

Doctoral Committee:

Professor Sara A. Pozzi, Chair
Professor Emeritus Frederick D. Becchetti, Jr.
Dr. Shaun D. Clarke
Professor Igor Jovanovic

Mark Andrew Norsworthy

marknors@umich.edu

ORCID iD: 0000-0003-4057-4546

© Mark A. Norsworthy 2017

Dedication

To Mom and Dad.

Acknowledgements

This dissertation is the culmination of education, support, and influence from far too many people to list. I wish to express the warmest gratitude to all my teachers, coaches, friends, mentors, and colleagues over the years.

I would especially like to thank Professor Sara Pozzi and Dr. Shaun Clarke for their guidance and advice throughout my doctoral program; in good times and bad, you have always supported me, and I will always be grateful. I want to thank all of the NERS faculty and staff for delivering the finest education in nuclear engineering available.

Thank you to all of my colleagues in DNNG for your friendship, collaboration, advice, and support. A special thank you to Dr. Alexis Poitrasson-Rivière and Dr. Marc Ruch for all of your help with the coding and debugging portions of this work.

Finally, thank you to my parents, Mike and Karen, and my brother, Mike, for thirty years of love, support, encouragement, and more than I can find words to express. You made me who I am. Thank you for everything.

This research was performed under appointment to the Nuclear Nonproliferation International Safeguards Fellowship Program sponsored by the National Nuclear Security Administration's Office of International Nuclear Safeguards (NA-241). Thank you to the NNSA, the American taxpayer, Craig Williamson, Nancy Carder, and Nicole Huchet for years of support.

This work was funded in-part by the Consortium for Verification Technology under Department of Energy National Nuclear Security Administration award number DE-NA0002534.

Table of Contents

List of Figures

List of Tables

Abstract

The International Atomic Energy Agency (IAEA) system of international safeguards employs a variety of technical measures to verify compliance with obligations under the Nuclear Non-Proliferation Treaty. Because special nuclear material emits neutrons, neutron detectors comprise a key element of the safeguards system. Currently deployed neutron detection safeguards instruments include coincidence counting systems employing ^{3}He to detect thermalized neutrons.

Fast neutron detection systems that do not require thermalization of neutrons have several potential advantages over thermal systems, and active research is underway to design and characterize such systems. Additionally, the IAEA requires systems that do not rely on the limited supply of ^{3}He. Organic scintillator detectors are promising candidates to address these needs. However, the IAEA has noted the need for robust Monte Carlo simulations of organic scintillator-based systems before they can be authorized for international safeguards deployment.

The response of organic scintillator detectors to neutrons is a complex process; in particular, the scintillation light generated in response to neutron collisions is nonlinear with respect to energy deposited. Accurate models of scintillation response (also called light output) are required for Monte Carlo simulations of organic scintillator-based systems. These models are also used in experiments to convert

collected pulse heights to energy depositions for neutron spectroscopy and imaging applications.

The choice among the several available empirical and semiempirical models for neutron light output can profoundly impact the accuracy of simulated pulse height distributions (PHDs). These models diverge significantly from one another in extrapolations to low energy (less than approximately 1 MeV energy deposition). In this work, EJ-309 light output data from neutrons depositing 1.15 MeV to 5.15 MeV on hydrogen are analyzed using empirical models as well as semi-empirical models based on the work of Birks and Voltz. The models are then tested by comparing a measurement and MCNPX-PoliMi simulation of an EJ-309 detector response to fast neutrons from a ^{252}Cf spontaneous fission source. The agreement between the measured and simulated PHDs varies significantly depending on the light output model used. The best agreement between simulated and measured neutron PHDs is achieved by using the Birks model.

The first measurements of energy-dependent light output from carbon recoils in the liquid organic scintillator EJ-309 are presented. For this measurement, neutrons were produced by an associated particle deuterium-tritium generator and scattered by a volume of EJ-309 scintillator into stop detectors positioned at four fixed angles. Carbon recoils in the scintillator were isolated using triple coincidence among the associated particle detector, scatter detector, and stop detectors. The kinematics of elastic and inelastic scatter allowed data collection at eight specific carbon recoil energies between 2.86 and 3.95 MeV. The light output caused by carbon recoils in this energy range is

found to be approximately 1.14% of that caused by electrons of the same energy, which is comparable to the values reported for other liquid organic scintillators.

The application of semiempirical proton light output models and accurate carbon light output and resolution functions is shown to substantially improve agreement between simulated and experimental detector response of EJ-309 organic liquid scintillators. This improved agreement, and the methods and models used to characterize the response, will support ongoing efforts to realize deployable IAEA safeguards systems based on organic liquid scintillators.

Chapter 1 Introduction

1.1 Nuclear Nonproliferation Treaty

The Treaty on the Non-Proliferation of Nuclear Weapons (NPT) entered into force on March 5, 1970 [1]. Presently, nearly every country in the world is a party to the treaty, with the exceptions of India, Israel, Pakistan, North Korea, and South Sudan. It is the most widely adhered-to arms control treaty in history [2].

The three key objectives of the NPT are to prevent the spread of nuclear weapons, to encourage peaceful nuclear cooperation, and to promote nuclear arms control and disarmament. The countries of the world are divided into two classes by the treaty: those that had manufactured and exploded a nuclear weapon or other nuclear explosive prior to January 1, 1967, (the United States, China, France, Russia, and the United Kingdom, referred to as "nuclear-weapon states"), and those that had not ("non-nuclear weapon states.") [1,2].

Article III of the NPT requires all non-nuclear-weapon States parties to accept comprehensive safeguards, implemented by the International Atomic Energy Agency (IAEA), to verify compliance with the obligations of the NPT. The safeguards system is intended to prevent the diversion of fissile material for weapons use [1,2]. The IAEA defines safeguards as a "set of technical measures to independently verify a State's legal commitment not to divert nuclear material from peaceful nuclear activities to nuclear weapons or other nuclear explosive devices." [3] Nuclear-weapon States parties to the

NPT participate in the safeguards system through voluntary offer safeguards agreements, and some item-specific safeguards agreements are in place in non-party States. More than 200,000 significant quantities of nuclear material are under safeguards around the world [3]. (A significant quantity is "the approximate amount of nuclear material for which the possibility of manufacturing a nuclear explosive device cannot be excluded." [3]).

1.2 Safeguards Research Needs

The IAEA Department of Safeguards' Long-Term Research and Development Plan, covering the period from 2012-2023, identifies three overarching strategic objectives [4]:

> *Deter the proliferation of nuclear weapons, by detecting early the misuse of nuclear material or technology, and by providing credible assurances that States are honouring their safeguards obligations;*
>
> *Contribute to nuclear arms control and disarmament, by responding to requests for verification and other technical assistance associated with related agreements and arrangements; and*
>
> *Continually improve and optimize departmental operations and capabilities to effectively carry out the IAEA's verification mission.*

The plan lists a variety of long term R&D needs, along with perceived priorities (low, medium, or high). Table 1-1 presents two specific capability needs identified in the plan that are supported by ongoing research projects at the University of Michigan (and elsewhere), including this dissertation.

Table 1-1. Excerpt from table of capabilities, milestones, and urgencies in IAEA Long-Term Strategic R&D Plan

Long Term Capabilities Needed	*Milestones*	*Urgency*
5. Ability to deploy equipment at facilities to meet safeguards requirements.	*5.8 Develop alternative [Non-Destructive Assay] NDA instruments, for instance based on liquid scintillators, to improve performance in neutron coincidence counting techniques applied to various types of fissile material.*	*M*
6. Ability to acquire and deploy safeguards equipment that is sustainable, standardized and modular, with increased use of commercial off-the-shelf products.	*6.2 Develop neutron counting systems reducing the use of ^{3}He or offering equivalent functional and technical alternatives.*	*M*

The needs identified in Table 1-1 include the development and deployment of alternative non-destructive assay instruments and safeguards equipment such as neutron counting systems and neutron coincidence counting systems. Milestone 5.8 mentions liquid scintillators specifically, while Milestone 6.2 mentions the reducing the use of He-3, in response to the widespread shortage that occurred in previous years. Several ongoing safeguards projects employ organic scintillators as fast neutron detectors, such as the Liquid-Scintillator Neutron Coincidence Collar (LS-NCC) [5], the Fast Neutron Multiplicity Counter (UM-FNMC) [6–8], radiation portal monitors (RPMs) [9,10], the Dual Particle Imager (DPI) [11–13], and the Handheld Dual Particle Imager (H2DPI) [14,15].

During a workshop on Helium-3 Alternative Technologies for Nuclear Safeguards, the IAEA representative noted that "high fidelity Monte Carlo modeling of the ^{3}He-alternative system must be possible…in order to authorize the use of proposed

^{3}He-alternative technologies." [5]. This requirement is related to the high level of technical certainty that is required to deploy a safeguards instrument; if the instrument is used in an international safeguards context, it is vital that the response of the instrument be well-understood by all parties.

The milestones in Table 1-1 and the IAEA's stated need for high fidelity Monte Carlo modeling provide the motivation for the research presented in this dissertation. The objective of the research is to improve the fidelity of the Monte Carlo modeling of organic scintillator detector response, and demonstrate that improvement by comparing the agreement between simulated and experimentally measured neutron pulse height distributions (PHDs).

1.3 Specific Problem

The specific problem to be addressed in this dissertation is the improvement of the agreement between simulated and experimentally measured neutron PHDs. To establish a baseline, and demonstrate the issues to be addressed, this section shows two sets of PHDs and their accompanying fractional difference plots. The details of the measurements and simulations are given in later chapters.

Figure 1-1 shows the PHDs and fractional difference plot obtained from a measurement of the neutrons from a ^{252}Cf fission source with a 5 in. by 5 in. EJ-309 liquid organic scintillator detector. ^{252}Cf is a common neutron source used as a stand-in for special nuclear material (SNM), because its fission neutron spectrum is similar to that of SNM. Figure 1-2 shows the PHDs and fractional difference plot obtained from a measurement of neutrons produced by 200-MeV protons incident on a soft-tissue phantom, such as might be produced during a proton radiotherapy treatment.

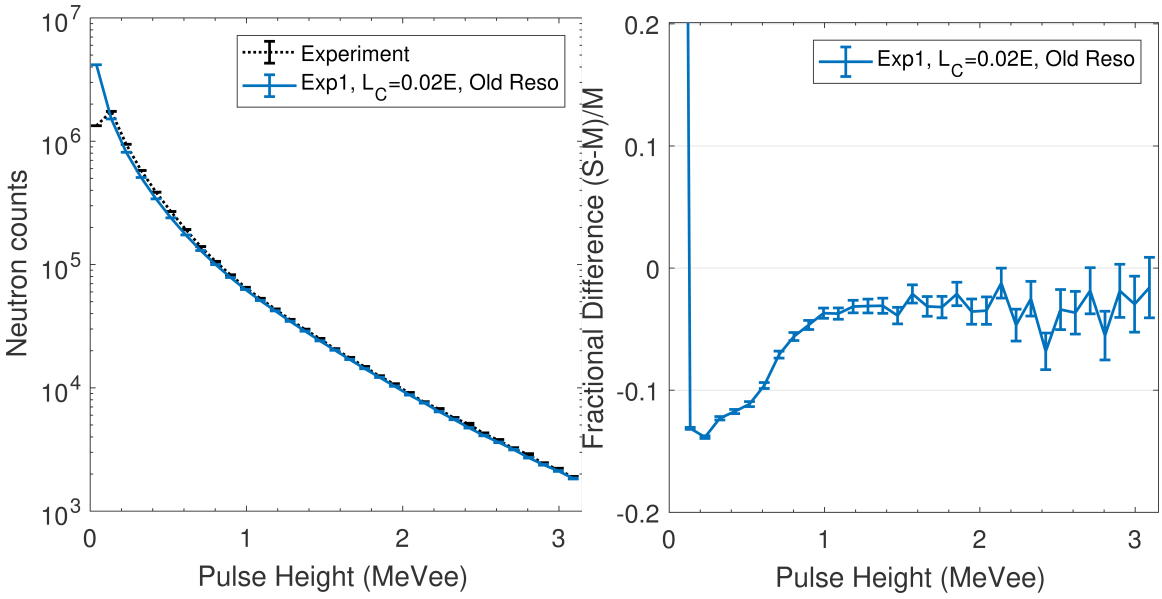

Figure 1-1 Left: Simulated (S) and measured (M) pulse height distributions, 5 in. by 5 in. EJ-309 detector, ^{252}Cf spontaneous fission neutron source. Right: Fractional difference plot.

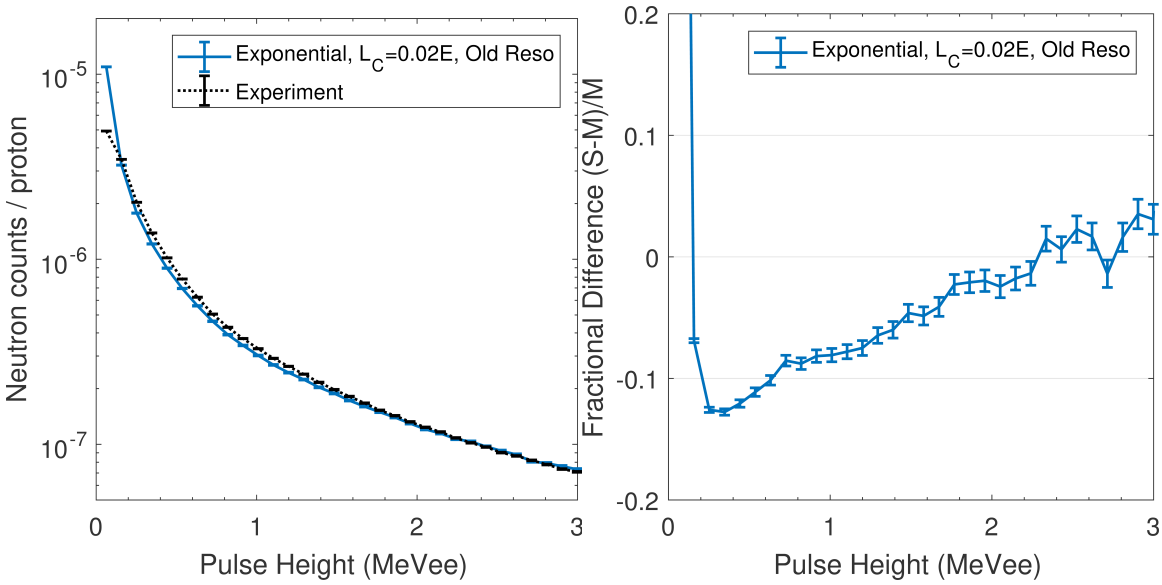

Figure 1-2 Left: Simulated (S) and measured (M) pulse height distributions, 3 in. by 3 in. EJ-309 detector, neutrons produced by 200 MeV protons incident on a soft tissue phantom. Right: Fractional difference plot.

Despite the disparate conditions, some similarities can be observed in the fractional difference plots. Ideal agreement would yield a flat line at a fractional difference of zero. In both cases, there is a significant deficit at low pulse heights in the

simulation. The discovery of these discrepancies served as the specific impetus for the work presented in this dissertation.

1.4 Contributions of the Dissertation

This dissertation presents improvements to organic scintillator detector response modeling in three areas: proton light output, and carbon light output, and detector resolution.

The choice among the several available empirical and semiempirical models for neutron light output can profoundly impact the accuracy of simulated PHDs. These models diverge significantly from one another in extrapolations to low energy (less than approximately 1 MeV energy deposition). In this work, EJ-309 light output data from neutrons depositing 1.15 MeV to 5.15 MeV on hydrogen are analyzed using empirical models as well as semi-empirical models based on the work of Birks and Voltz. The models are then tested by comparing a measurement and MCNPX-PoliMi simulation of an EJ-309 detector response to fast neutrons from a ^{252}Cf spontaneous fission source. The agreement between the measured and simulated PHDs varies significantly depending on the light output model used. The best agreement between simulated and measured neutron PHDs is achieved by using the Birks model.

The first measurements of energy-dependent light output from carbon recoils in the liquid organic scintillator EJ-309 are presented. For this measurement, neutrons were produced by an associated particle deuterium-tritium generator and scattered by a volume of EJ-309 scintillator into stop detectors positioned at four fixed angles. Carbon recoils in the scintillator were isolated using triple coincidence among the associated particle detector, scatter detector, and stop detectors. The kinematics of elastic and inelastic

scatter allowed data collection at eight specific carbon recoil energies between 2.86 and 3.95 MeV. The light output caused by carbon recoils in this energy range is found to be approximately 1.14% of that caused by electrons of the same energy, which is comparable to the values reported for other liquid organic scintillators. The small pulse height peaks of the carbon recoil measurement are used to refine previous estimates of detector resolution.

The application of semiempirical proton light output models and accurate carbon light output and resolution functions is shown to substantially improve agreement between simulated and experimental detector response of EJ-309 organic liquid scintillators. Neutrons produced during proton therapy are measured and used as a test case for demonstrating the improved agreement achieved by employing the light output and resolution functions developed in this work.

1.5 Impact Statement

This research will significantly improve the modeling of organic scintillator detector response for safeguards and other applications. The improved agreement of simulated and experimental neutron PHDs for EJ-309 detectors, and the methods and models used to characterize the response, will support ongoing efforts to realize deployable IAEA safeguards systems based on organic liquid scintillators. The semiempirical proton light output model work is published as an article in *Nuclear Instruments and Methods in Physics Research, Section A,* and is contributing to organic scintillator research at other institutions. The carbon light output response work has recently been submitted for publication. The improvements demonstrated in this

dissertation have been adopted successfully by researchers at University of Michigan and elsewhere.

1.6 Structure of the Dissertation

This dissertation is structured as follows. The present chapter motivates the work and orients the reader.

Chapter 2 provides background information regarding the basic characteristics of the EJ-309 organic scintillator detectors used and the Monte Carlo simulation tools employed.

Chapter 3 presents the proton light output research contribution, which consists of our findings regarding the use semiempirical models for hydrogen recoil response and resulting improved agreement of simulations of detector response to neutrons from Cf-252 spontaneous fission. The results in Chapter 3 represent the most important contribution of the dissertation in terms of improving simulated detector response, especially in the fission neutron energy range. These results were published in 2017 in NIM A [16].

Chapter 4 shifts from proton light output to carbon light output. It is an expanded version of our recently-submitted journal article, "Light Output Response of EJ-309 due to Neutron Elastic and Inelastic Scatter on Carbon," which presents our findings regarding carbon recoil response. Our measurements of carbon recoil response are the first conducted using EJ-309.

Chapter 5 presents an additional result of the carbon light output experiment; an improved detector resolution function, especially at low pulse heights.

Chapter 6 employs each of the above contributions and demonstrates the resulting improvement in agreement between simulated and experimental detector response in a non-traditional, non-safeguards application of organic scintillators: detection of neutrons produced during proton therapy.

Chapter 7 summarizes the work presented, draws conclusions, and consolidates the best estimates for proton light output, carbon light output, and detector resolution for EJ-309 organic scintillator detectors. Chapter 7 also identifies several suggestions for future work.

Chapter 2 Organic Scintillator Detector Response Overview

2.1 Chapter Introduction

This chapter describes the basics of organic scintillator detector response and common methodologies employed within DNNG for experimental and simulated detector response.

The basic framework of organic scintillator detector response is the following:

1. Radiation interacts with the organic scintillator molecules, creating recoil particles (electrons or recoil nuclei).
2. Recoil particles create ionizations and excitations along their track as they slow down and ultimately stop.
3. The ionizations and excitations interact with each other and/or decay, in some cases producing photons of visible light (scintillation).
4. The photons are collected and converted to photoelectrons, amplified, and recorded as a voltage pulse.
5. These pulses are analyzed and classified into groups, for example by pulse shape for pulse shape discrimination, or by time windows for time-of-flight gating.
6. The groups of pulses are histogrammed into a PHD.
7. The features of the PHDs can then be analyzed.

This chapter progresses through these steps providing background information. Some additional background is developed in subsequent chapters as needed.

2.2 Organic Scintillators

Organic scintillator detectors are used as fast neutron detectors in a variety of applications. Detector systems employing organic scintillators exist or are under development with application to nuclear nonproliferation and international safeguards (e.g., instrumentation systems for the IAEA [5]), nuclear medicine (neutron detection in

hadron therapy facilities [17]), nuclear physics (neutrino detection [18], and weakly interacting massive particle (WIMP)/dark matter detection [19–21]), among others. Organic scintillators have several desirable attributes as neutron detectors, including fast timing properties, pulse shape discrimination capabilities, and limited spectroscopic capability due the preservation of information about the energy of incident neutrons.

Several types of organic scintillators have been investigated by safeguards researchers, including plastic, liquid, and crystalline detectors. The two most commonly employed types in our research group are stilbene crystal detectors and EJ-309 liquid organic scintillators. This dissertation focuses on EJ-309. Stilbene has an anisotropic response to neutron interactions that is the subject of active characterization efforts; the technique presented in Chapter 5 will be useful for characterizing stilbene more fully.

2.2.1 Basic properties

EJ-309 is similar in composition to EJ-301/NE-213, but has been modified to have a high flash point to eliminate the fire hazard associated with EJ-301 and other low-flash point liquid scintillators [22]. EJ-309 is therefore an attractive liquid scintillator material for nonproliferation and safeguards applications, among others. The basic properties of EJ-301 and EJ-309 are listed in Table 2-1 [22].

Table 2-1. Basic properties of EJ-301 and EJ-309 liquid organic scintillators.

Properties	*EJ-301*	*EJ-309*
Light Output (% Anthracene)	*78*	*80*
Scintillation Efficiency (photons/1 MeV e-)	*12,000*	*12,300*
Wavelength of Maximum Emission (nm)	*425*	*424*
Mean Decay Times of First 3 Components (ns)	*3.16* *32.3* *270*	*-*
Bulk Attenuation Length	*(2.5-3)*	*>1*
Refractive Index	*1.505*	*1.57*

Flash Point (°C)	*26*	*144*
Boiling Point (°C at 1 atm)	*141*	*290-300*
Vapor Pressure (mm Hg. At 20°C)	*-*	*0.002*
No. of H Atoms per cm³	*4.82*	*5.43*
No. of C Atoms per cm³	*3.98*	*4.35*
No. of Electrons per cm³	*2.27*	*3.16*

EJ-309, like all organic scintillators, is composed of hydrocarbon molecules. When radiation interacts with EJ-309, it interacts with either H nuclei, C nuclei, or electrons. If sufficient energy is imparted to these particles, they can be knocked free of their molecular bonds to travel some distance through the scintillator as a recoil. The subsequent interactions of these recoil particles with the other scintillator molecules gives rise to visible light that can be collected with a device such as a photomultiplier tube (PMT) or silicon photomultiplier. Other competing processes can suppress the amount of visible light produced. The next few subsections discuss these phenomena in greater detail.

2.2.2 Photon interactions

Figure 2-1 [23] shows the dependence of the three major types of gamma-ray interaction on the atomic number Z of the absorber material. Organic scintillators are low-Z detectors. If the incident radiation is a photon, the typical mode of interaction is Compton scattering on electrons. At very low energies, such as characteristic X-ray interactions, photoelectric absorption becomes competitive. The low probability of photoelectric absorption, and thus the lack of photopeaks, makes calibration of an organic scintillator somewhat more challenging than high-Z detectors. Chapter 3 discusses calibration of an organic scintillator using the Compton edge.

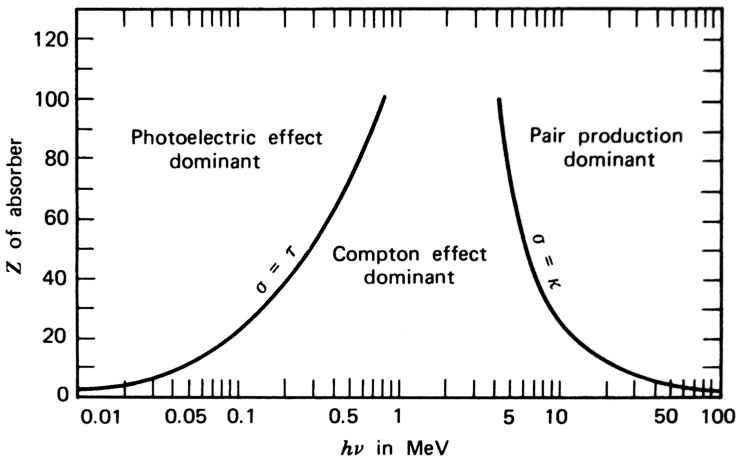

Figure 2-1 The relative importance of the three major types of gamma-ray interaction. The lines show the values of Z and hν for which the two neighboring effects are just equal. From [23], Fig. 2.20.

2.2.3 Neutron interactions

Neutrons deposit energy in the scintillator through elastic and inelastic scattering on hydrogen and carbon nuclei, and the recoiling nuclei interact with the scintillation molecules to produce scintillation light. Figure 2-2a shows the cross sections for three interaction channels: elastic scatter on hydrogen and elastic and inelastic scatter (to the

first excited state) on carbon, for the energy range from 0.1 to 20 MeV. At low energies, the hydrogen cross section dominates, but as neutron energy increases the carbon elastic scatter cross section approaches and then surpasses hydrogen. The inelastic scatter cross section exhibits a lower threshold because the incident neutron must have sufficient energy to excite the carbon nucleus to its first excited state.

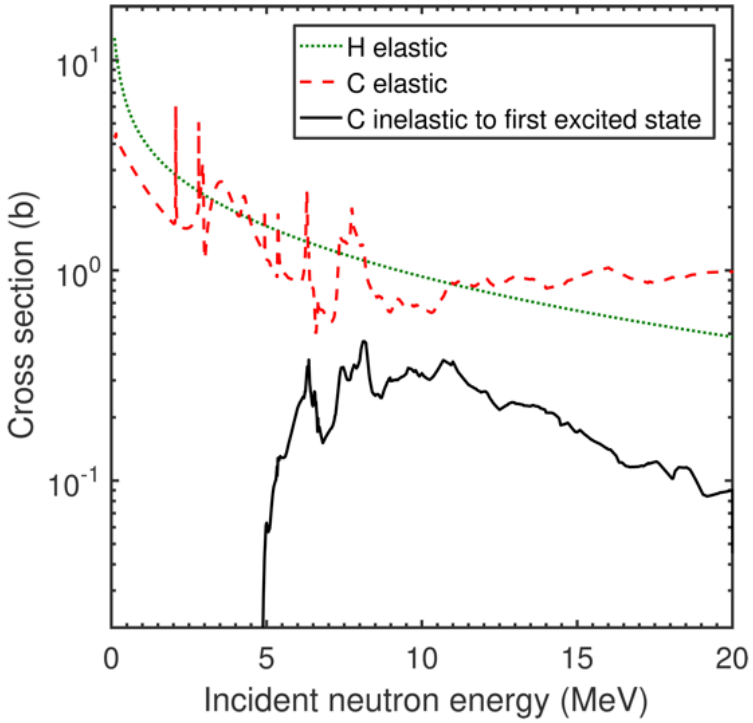

Figure 2-2 Elastic and inelastic neutron reaction cross sections on hydrogen and carbon [13].

Other neutron interaction channels, such as $^{12}C(n,\alpha)^{9}C$ or $^{12}C(n,n')3\alpha$ are not considered in this dissertation, but are mentioned in Chapter 7 for future work.

2.2.4 Scintillation

When a scintillator molecule is excited, two types of states can be created: singlet states and triplet states. Figure 2-3 shows a conceptual level diagram for a scintillator molecule. The primary states of interest are S10 and T10. Higher levels decay rapidly to

these levels, and the photons of interest are produced by the S10 decay to S0, called "fluorescence." These are the photons that are emitted in the visible light portion of the electromagnetic spectrum and collected, for instance by the photocathode of a PMT. The majority of the singlet excitations occur during the initial track of the recoil ion, and decay promptly. The light collected is therefore primarily in the "prompt" portion of a pulse.

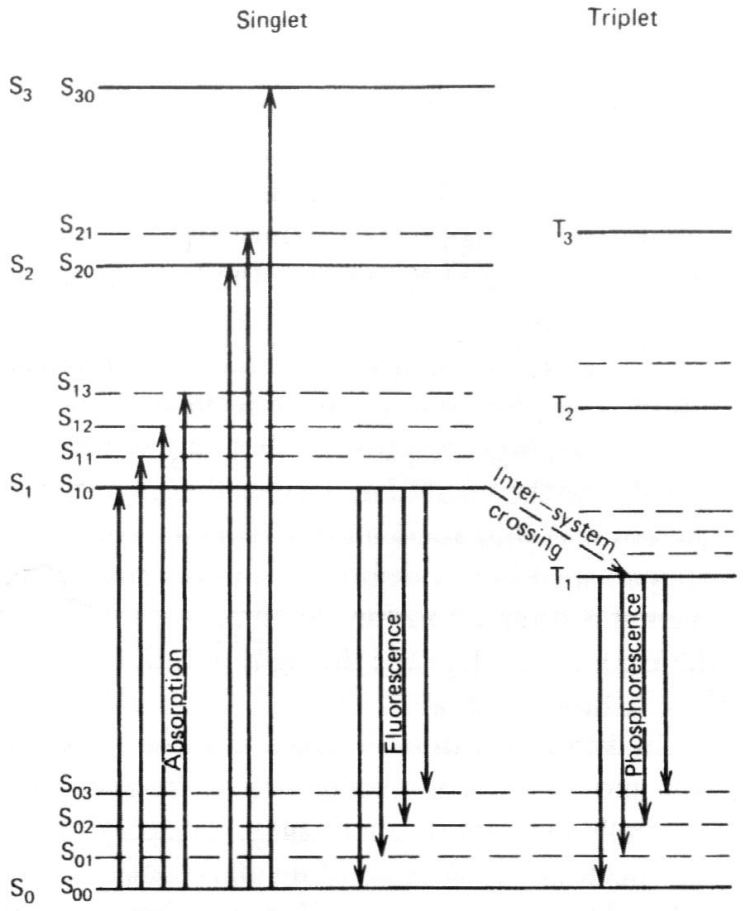

Figure 2-3. Energy levels of an organic molecule with pi-electron structure. Reproduced from [24].

Triplet state behavior is more complex. Triplets can decay directly to ground, through phosphorescence, but the transition is "forbidden" and therefore occurs with a much longer half-life on the order of microseconds. The wavelength of phosphorescence

light is also different, typically longer than fluorescence light. Phosphorescence creates a long-lived low-intensity background of light whose wavelength is mismatched with the optimum acceptance of the photocathode; therefore, it is ignored in most applications, as well as in this work.

The most relevant triplet interaction is when one triplet state interacts with another. The result is that one molecule goes to ground, while the other is left in a super-excited singlet state. This state quickly falls to S10, and then S00. This final decay emits a photon in the fluorescence wavelength, but occurs at a later time (following triplet creation, migration, and triplet-triplet interaction). Thus, these photons are called "delayed fluorescence." Another factor contributing to the delay is that triplet states themselves are often the result of the recombination of ionized (as opposed to excited) molecules.

Singlet state and triplet state creation and decay behavior are strongly influenced by ionization density, giving rise to a phenomenon called ionization quenching, discussed in the next section.

2.2.5 Ionization Quenching

Ionization quenching results in a reduction in the amount of light produced versus the amount produced by a gamma ray depositing equal energy. Quenching is proportional to ionization density: if the ions and excited states are created closer together, they are more likely to find each other and recombine. Recoil electrons in general have low stopping powers; therefore, the light can be considered largely unquenched. Protons have dramatically higher stopping powers, which leads to higher ionization densities and increased quenching compared to electron recoils. Heavier particles such as alpha

particles and carbon ions have even higher stopping powers, so they produce less light. Figure 2-4 shows the total stopping powers in EJ-309 of electrons, protons, and carbon ions, as determined by the use of the SRIM software package [25,26] and the NIST ESTAR database [27]. These are the stopping power values used throughout this work.

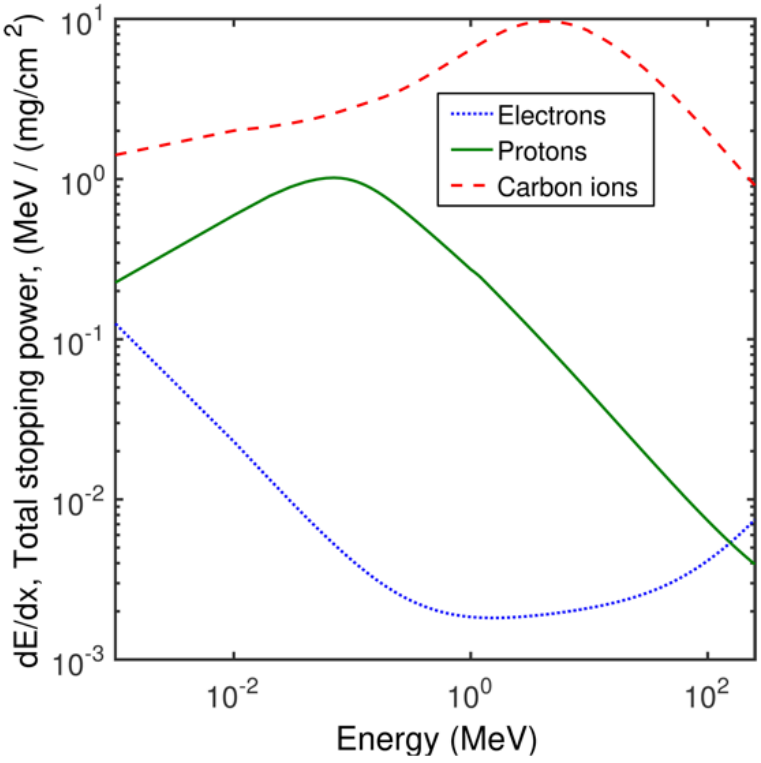

Figure 2-4 Total stopping power of electrons and protons in EJ-309 liquid scintillator, generated using the NIST ESTAR database [14] and the SRIM-2012 package [15,16].

2.2.6 Pulse Shape Discrimination

Organic scintillator detectors are sensitive to both neutrons and photons through different interaction mechanisms[23]. The scintillator molecules are excited by charged particle recoils: electrons in the case of incident photons, and recoil nuclei in the case of incident neutrons. The light generated by the decay of the excited states is collected and converted to a voltage pulse by photomultiplier tubes. Because the detectors are

hydrocarbons, the recoil particles from neutrons can be hydrogen (protons) or carbon nuclei.

Some organic scintillators, including the ones used in this study, are capable of pulse shape discrimination (PSD), whereby the voltage pulses generated by recoil electrons and protons have different shapes [24,28]. This effect is primarily due to the higher stopping power of recoil protons compared to electrons, so the protons deposit their energy in a smaller volume of scintillator. The increased ionization density causes several effects, including quenching of prompt singlet states and increased production of delayed singlet states by triplet-triplet annihilation. The net effect is that proton recoil pulses, induced by incident neutrons, have a larger fraction of "delayed" or "tail" light than electron recoil pulses, induced by incident photons. Figure 2-5 shows two digitized pulses from a stilbene scintillator detector: one classified as a gamma-ray pulse and one as a neutron pulse to illustrate the different tail behavior.

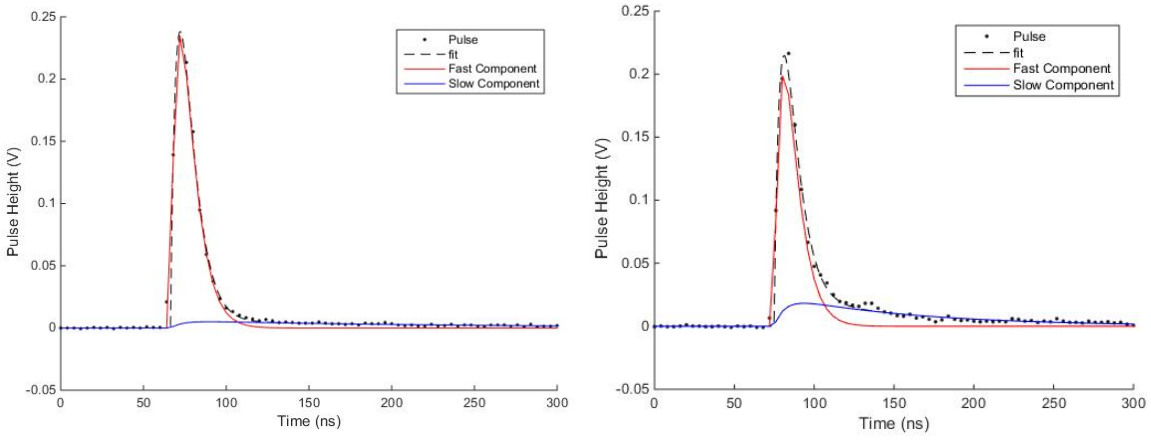

Figure 2-5. The left panel shows a typical gamma-ray pulse (in this case from a stilbene detector), with fast and slow components fit according to [29]. The right panel shows a neutron pulse with a similar pulse height; the tail component of the neutron pulse is significantly larger.

Figure 2-6 shows a two-dimensional histogram of the tail and total integrals of a set of measured neutrons and gamma rays from one of the EJ-309 detectors. The PSD line is also shown: the pulses above the line are classified as neutrons, while those below the line are classified as gamma rays. The PSD line can be determined visually, but for this plot we utilized the SlicePSD algorithm to select the line [30]. For smaller pulses, the groups begin to overlap. In this region, any line will result in some particle misclassification (photons misclassified as neutrons and vice versa). The effect of this misclassification is that experimental neutron PHDs will be lower than the simulated ones for small pulse heights.

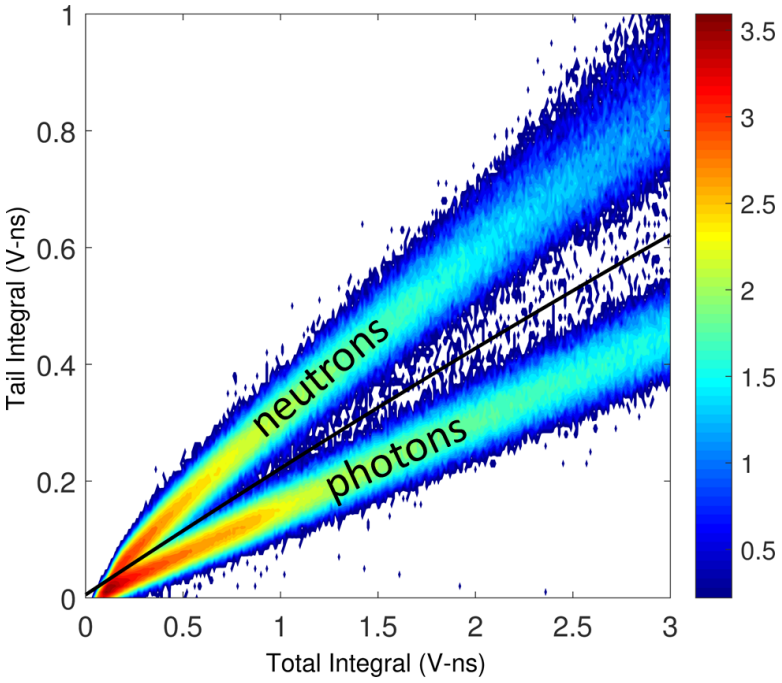

Figure 2-6 Experimental data: 2-D histogram of neutron (above black discrimination line) and gamma ray (below black discrimination line) pulses from an EJ-309 liquid scintillator.

2.2.7 Pulse Height Distributions

After the collection and classification of a large number of pulses, the pulses are histogrammed. The histogram is called a PHD; subsequent analysis can reveal

information about the incident radiation. The PHD is the basic output of a radiation measurement that this dissertation seeks to accurately understand and reproduce in simulation; in particular, we are interested in matching neutron PHDs.

It should be noted that in this work, as in [31], the term 'pulse height' refers to the maximum of the digitized pulse, as opposed to the pulse integral. Pulse height is not always proportional to pulse integral, so it is not in general possible to easily translate between pulse height and pulse integral based light output functions. However, although the absolute values will vary, the methodologies used in this dissertation would also be applicable to pulse integral data.

Accurate simulation of PHDs requires accounting for the variety of processes that contribute to the features of the distribution. Figure 2-7 shows some of the key features that need to be accounted for in a simulation of a neutron PHD. Figure 2-7(a) shows scintillator nonlinearity, which, in this case, refers to the nonlinear light output of proton recoils—the light produced is not a linear function of proton recoil energy. This is discussed in detail in Chapter 4. Figure 2-7(b) indicates one of the effects of carbon scattering, particularly in the context of multiple scatter events (e.g. a carbon scatter followed by a hydrogen scatter). Carbon scatters are considered in detail in Chapter 5. Figure 2-7(c) shows the broadening of what would otherwise be a sharp edge due to maximum energy transfer from a monoenergetic neutron source. This resolution function is discussed in Chapter 6.

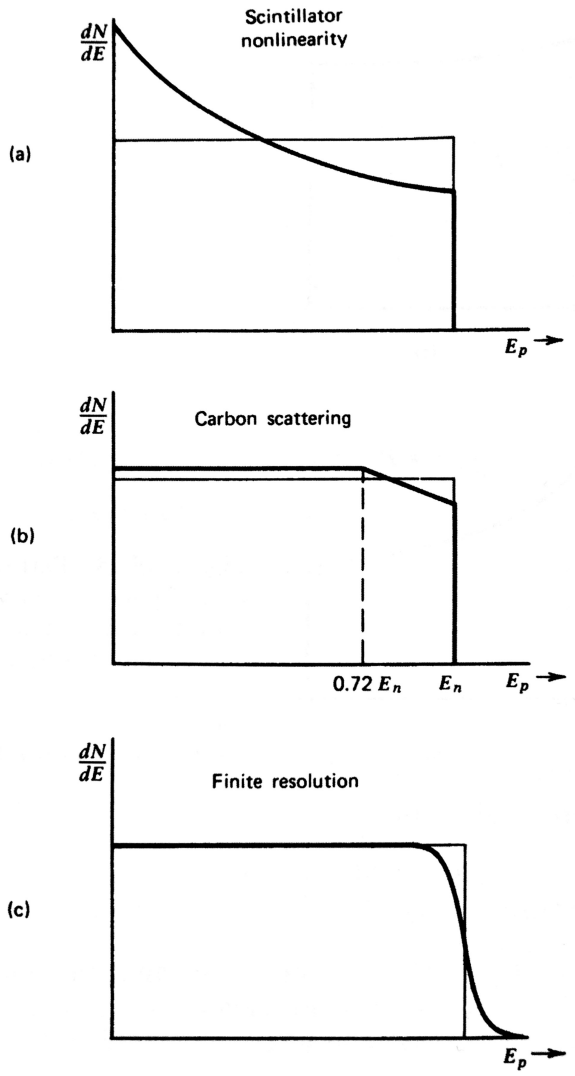

Figure 2-7. From [23]: "Distortions to the rectangular recoil proton energy spectrum due to three separate factors." Three aspects of a neutron pulse shape distribution in an organic scintillator that must be considered in modeling, namely scintillator nonlinearity, carbon scattering, and finite resolution, each of which are addressed in later chapters of this dissertation.

2.3 MCNPX-PoliMi and MPPost

All of the above discussion related to the real-world detection of radiation using organic scintillators. As indicated in Chapter 1, the ability to accurately simulate these physical processes and the resulting detector response output is important for a variety of applications, including the design of international safeguards instruments and the interpretation of measured results. The simulation code used in this work is MCNPX-

PoliMi, in conjunction with post-processing tools, the most important of which is MPPost.

MCNPX-PoliMi and the MPPost post-processing tool have been extensively tested and used for applications in nuclear nonproliferation and safeguards, nuclear physics, and medical physics [32–34]. The MCNPX-PoliMi code generates a data file of all neutron and photon events in specified cells. Using accurate calibration and light output relationships, one can use MPPost to generate a histogram of pulse heights, or PHD. These PHDs can then be validated against the experimental PHDs. Table 2-2 and Fig 2-8 show an excerpt of the MCNP-PoliMi data file (MCNP-PoliMi was the predecessor to MCNPX-PoliMi) and a flowchart of the MPPost pulse processing algorithm.

The generation of pulse height from individual collision events is a nonlinear process and cannot be accomplished with simple MCNPX tallies; the PTRAC feature of MCNPX could be used to extract the information in the data files, but the PoliMi data file format is more convenient to use.

Table 2-2. Reproduced from [35], excerpt of MCNP-PoliMi output file. MCNPX-PoliMi output is identical except for the addition of a 15th column that shows incident energy in MeV.

MCNP-PoliMi output file: excerpt

History number	Particle number	Projectile type[a]	Interaction type[b]	Target nucleus[c]	Cell number	Energy deposited (MeV)	Time (shakes)	Collision position (x, y, z)			WGT	Generation number	Number scatterings	Code
—	—	—	—	—	—	—	—	—	—	—	—	—	—	—
16	97	1	−99	1001	2	0.5309	8.095	43.57	4.88	1.84	1	3	5	0
16	97	1	−99	1001	2	0.0553	8.395	44.29	5.57	1.85	1	3	6	0
16	97	1	−99	1001	2	0.0014	11.722	44.92	5.04	3.78	1	3	9	0
109	1	1	0	6000	5	8.398	1.798	43.98	−7.52	6.31	1	0	0	0
132	1	1	−99	1001	5	13.9313	1.778	42.06	−2.98	1.42	1	0	2	0
132	1	1	−99	1001	5	0.1036	2.075	42.55	−2.34	2.88	1	0	3	0
132	1	1	−99	1001	5	0.0281	2.264	42.25	−2.39	3.44	1	0	4	0
132	1	1	−99	1001	5	0.0131	2.372	42.16	−2.22	3.63	1	0	5	0
335	58	1	−99	6000	4	0.0019	3.72	43.98	0.16	9.54	1	3	5	0
335	58	1	−99	1001	3	0.0042	4.069	42.64	−0.01	9.13	1	3	6	0
485	1	1	−99	1001	5	8.2582	1.872	48.08	−2.19	7.51	1	0	1	0
495	24	2	1	6	2	0.1461	1.036	43.87	3.46	5.06	1	1	2	0
495	24	2	1	6	2	1.2823	1.036	43.95	3.47	5.08	1	1	3	−1
495	24	2	1	6	2	0.038	1.038	43.41	3.8	5.12	1	1	4	−1
495	24	2	1	1	2	0.0793	1.038	43.28	3.76	5.08	1	1	5	−1
495	24	2	1	6	2	0.0421	1.042	43.69	3.19	5.93	1	1	6	−1

[a] 1 = neutron; 2 = photon.
[b] −99 = elastic scattering; 1 = Compton scattering; 0 = absorption.
[c] 1001 and 1 = hydrogen; 6000 and 6 = carbon.

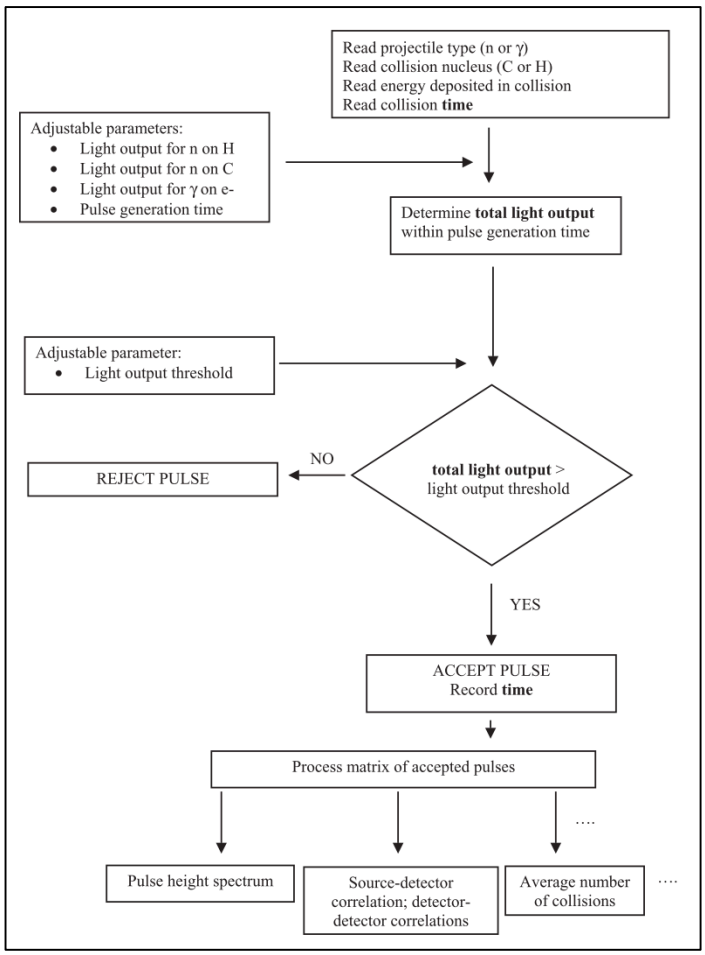

Figure 2-8. Reproduced from [35]. Block diagram of post-processing code for the MCNP-PoliMi code. The algorithm for MPPost is essentially the same, with the addition of some additional adjustable parameters such as time and energy resolution.

2.3.1 Thresholds, Pulse Heights, and Resolution

MPPost accepts the PoliMi data file and converts the energy deposited in collisions (MeV) to light (MeVee). The upper and lower experimental thresholds, determined in units of MeVee, are applied in the Detector Information section of the input file. These thresholds are used to determine whether or not a pulse is written to the PHD output.

Within a history, energy depositions in MeV are converted to light in MeVee, and then summed to give a pulse height value. The relationships and coefficients for proton light output and carbon light output that were typically employed for EJ-309 are presented here. The proton values are based on the work of Enqvist et al [31], and are of the form,

$$L(E) = aE - b[1 - \exp(-cE^d)], \tag{2-1}$$

with coefficients listed in Table 2-3. The carbon constant was set to 0.02 MeVee per MeV in the early days of PoliMi [36].

Table 2-3. Typical light output coefficients, for *L* in MeVee and *E* in MeV.

Detector Size	***Recoil***	***a***	***b***	***c***	***d***
3x3	***Proton***	***0.817***	***2.63***	***0.297***	***1.000***
5x5	***Proton***	***0.748***	***2.41***	***0.298***	***1.000***
Both	***Carbon***	***0.02***			

Table 2-2 also presents the former resolution coefficients for the detector energy resolution for 3x3 and 5x5 EJ-309 detectors, determined in [31]. The resolution function is of the form,

$$\frac{\Delta L}{L} = \sqrt{\alpha^2 + \frac{\beta^2}{L} + \left(\frac{\gamma}{L}\right)^2} \tag{2-2}$$

Where ΔL is the full-width at half-maximum (FWHM) and L is the light in MeVee. However, in MPPost, the implementation is of a different form, adapted from [37] where L is now in keVee:

$$\frac{\Delta L}{L} = \frac{AL + B\sqrt{L} + C}{100L}, \tag{2-3}$$

with coefficients presented in Table 2-4.

Table 2-4. Previous resolution coefficients, for $\Delta L/L$ where L is in keVee.

Detector Size	α	β	γ		A	B	C
3x3	*0.113*	*0.065*	*0.060*		*9.8532*	*0*	*4738.6643*
5x5	*0.102*	*0.102*	*0.035*		*10.6092*	*11.2033*	*3923.0106*

In Chapters 3, 4, and 5 of this dissertation, I present new relationships for proton light output, carbon light output, and detector resolution for the EJ-309 detectors commonly used in DNNG.

2.3.2 Light Output and this Thesis

In organic scintillators, interactions with hydrogen produce the majority of the neutron-induced scintillation light; the amount of light produced is a nonlinear function of the energy deposited. The light output function affects every neutron event in both Monte Carlo simulations and the interpretation of experimental data. In experiments, it is used to convert collected light (proportional to pulse height) to energy deposited, which is a key parameter in neutron spectroscopy and imaging applications. In Monte Carlo simulations, the energy deposited by each neutron interaction is known, and the light

output function is used to simulate pulse heights. More accurate light output functions would yield more accurate simulations of detector response, more reliable simulated neutron efficiency, and improve the results obtained when using simulated response matrices for spectrum unfolding. Ultimately, these improvements would benefit the design of detection systems for inspections, treaty verification activities, nuclear material accountancy, and other safeguards programs.

Chapter 3 Proton Recoil Response

3.1 This Chapter

An accurate model of the nonlinear detector response of organic scintillators to neutrons is required to correctly simulate fast neutron detection, as well as interpret measured pulse height data. Several empirical and semi-empirical models are available to fit measured scintillator light output data. In this work, EJ-309 light output data from neutrons depositing 1.15 MeV to 5.15 MeV on hydrogen were analyzed using empirical models as well as semi-empirical models based on the work of Birks and Voltz. Although all tested models fit the experimental light output data well in the measured range, the models were observed to diverge in low-energy extrapolation. The models were then tested by comparing a measurement and MCNPX-PoliMi simulation of an EJ-309 detector response to fast neutrons from a ^{252}Cf spontaneous fission source. The agreement between the measured and simulated PHDs varied significantly depending on the light output model used. The best agreement between simulated and measured neutron PHDs was achieved by using the Birks model. The bin-by-bin agreement was better than 5% over the range 0.08 to 2.18 MeVee, and better than 10% from 2.18 to 3.13 MeVee. The integral count rate over the range 0.08 to 3.14 MeVee differed by less than 1% in absolute units.

This chapter presents a lightly edited version of the 2017 publication in NIM A, Evaluation of Neutron Light Output Response Functions in EJ-309 Organic Scintillators.

3.2 Introduction

In organic scintillators, interactions with hydrogen produce the majority of the neutron-induced scintillation light; the amount of light produced is a nonlinear function of the energy deposited. The light output function affects every neutron event in both Monte Carlo simulations and the interpretation of experimental data. In experiments, it is used to convert collected light (proportional to pulse height) to energy deposited, which is a key parameter in neutron spectroscopy and imaging applications. In Monte Carlo simulations, the energy deposited by each neutron interaction is known, and the light output function is used to simulate pulse heights. More accurate light output functions would yield more accurate simulations of detector response, more reliable simulated neutron efficiency, and improve the results obtained when using simulated response matrices for spectrum unfolding. Ultimately, these improvements would benefit the design of detection systems for inspections, treaty verification activities, nuclear material accountancy, and other safeguards programs.

Careful measurements are required to generate the light output function. These measurements usually result in a discrete set of data points relating energy deposition to light output. To fill in gaps between data points, as well as to extrapolate to lower and higher energies, these data are fitted using a variety of functional forms ranging from simple polynomials [31], rationals of polynomials [31], power laws [38], and exponential functions [31,39] to semi-empirical models such as those proposed by Birks and Voltz [24,28,40,41].

This paper demonstrates that the choice of functional form for the light output function for neutron interactions on hydrogen profoundly impacts the accuracy of

simulated PHDs. The choice of neutron light output function also alters the calculation of neutron detection energy thresholds, and has direct consequences on neutron unfolding, dosimetry, and imaging results. In particular, this paper concerns the divergence of the various light output models in extrapolation to low energies, and the corresponding effect on simulated PHDs.

We revisit the EJ-309 light output data of Enqvist and colleagues [31] and fit them to various functional forms. We show that many forms can be chosen that give good fits to the measured light output data points, but they diverge significantly from one another in extrapolation. We then use the code MCNPX-PoliMi [33] to simulate EJ-309 detector response to neutrons from a ^{252}Cf spontaneous fission source, and we use the post-processing code MPPost [34] to apply the different light output functions to generate neutron PHDs. We compare the simulated PHDs to measured data and conclude that the semi-empirical functional forms perform significantly better than the commonly used empirical forms.

3.3 Background

Birks [24], Voltz [40], Craun [42], and others have proposed equations for light output that include quenching terms that are proportional to the stopping power of the recoil particle in the detector material, dE/dx.

Kornilov and colleagues [43] showed that a rational function of polynomials could give a good fit for a quick estimate, but for calculations demanding higher degrees of accuracy, more complex equations were required. Kornilov and colleagues [43] and Enqvist and colleagues [31] made use of an exponential functional form. The former also explored one of the semi-empirical functional forms, based on Birks' Law, achieving

better agreement with experimental data. All of these forms are tested in this work, in addition to a relationship proposed by Voltz and colleagues [28,40,41]. Table 3-1 shows all of the functional forms that are examined in this work, where E is the neutron energy deposited on hydrogen, and L is the light produced in the scintillator. The coefficients a, b, c are computed in the fits.

Table 3-1. Neutron light output equations tested in this work.

"Polynomial"	$L(E) = aE^2 + bE + c$	*(3-1)*
"Rational"	$L(E) = \frac{aE^2}{E+b}$	*(3-2)*
"Power Law"	$L(E) = aE^b$	*(3-3)*
"Exponential"	$L(E) = aE - b\left[1 - exp\left(-cE^d\right)\right]$	*(3-4)*
"Birks"	$L(E) = \int \frac{a}{1+b\left(\frac{dE}{dx}\right)} dE$	*(3-5)*
"Voltz"	$L(E) = a\int[(1-c)\,exp\left[-\frac{b(1-c)dE}{dx}\right] + c]\,dE$	*(3-6)*

The two semi-empirical functions are based on the concept of ionization quenching: a reduction in the amount of light produced versus that which would be produced by a gamma ray depositing equal energy to a recoil electron. In both models, quenching increases with increasing ionization density, which in turn increases with stopping power (dE/dx). Fig. 3-1 shows the stopping power of protons and electrons in EJ-309, as determined by the use of the SRIM software package [25,26] and the NIST ESTAR database [27], respectively. These are the stopping power values used throughout this work.

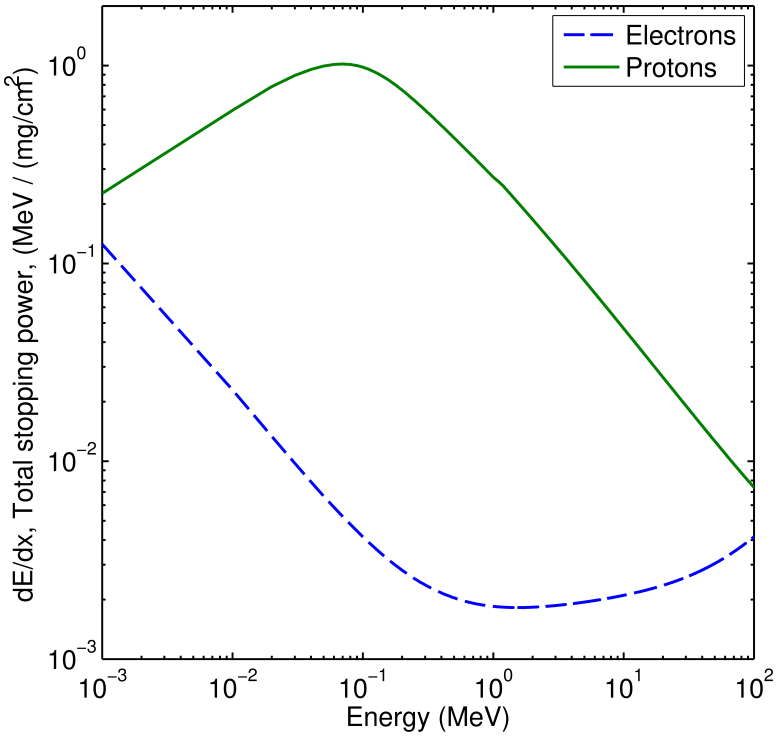

Figure 3-1. Total stopping power of electrons and protons in EJ-309 liquid scintillator, generated using the NIST ESTAR database [25] and the SRIM-2012 package [23,24], respectively.

The forms used in this work for Birks' Law (Eq. 3-5) and the Voltz model (Eq. 3-6) are the integrals over energy of Eq. 3 and Eq. 6 in Brooks and colleagues' review paper [28]. Because our work is far from relativistic energies, we introduce an approximation of the Voltz model in which F_s (c in Eq. 3-6) is fitted as a constant instead of a function of charge and energy as in Ahlen and colleagues [41].

3.4 Light Output Fitting Methodology

We reconstructed light output data points as a function of energy deposited, *L(E)*, from a time-of flight measurement performed at the Edwards Accelerator Facility at Ohio University [13]. The measurement was performed with a 12.7 cm thick x 12.7 cm diameter EJ-309 liquid scintillator detector coupled to a Photonics XP4512B photomultiplier tubes (PMT). The data were generated using a 10-meter flight path and

neutrons were generated using the $^{27}Al(d,n)$ reaction resulting in a white source containing a wide range of energies. The pulses were digitized using a 250-Mhz, 12-bit CAEN Electronics V1720 digitizer. Time-of-flight was used to sort neutrons with energies from 1.15 to 5.15 MeV in 100 keV-wide bins. Because neutrons can deposit any fraction of their energy in each collision on hydrogen, it can be difficult to determine the pulse height corresponding to a single full-energy transfer; however, as will be seen later in this work, the light output function is concave in this energy range, meaning that a single scatter yields more light than any two smaller scatters depositing the same total energy. Following Kornilov [43], the binned PHDs were smoothed, differentiated, and a Gaussian was fitted to the rightmost peak of the derivative. The mean of the Gaussian was taken as the pulse height corresponding to a neutron scattering once on hydrogen and depositing all of its energy.

It should be noted that in this work, as in [31], the term 'pulse height' refers to the maximum of the digitized pulse, as opposed to the pulse integral. Pulse height is not always proportional to pulse integral, so it is not in general possible to easily translate between pulse height and pulse integral based light output functions. However, although the absolute values will vary, the methodology used here would also be applicable to pulse integral data.

Generation of the empirical fits was performed using the MATLAB Curve Fitting Toolbox [44]. Enqvist and colleagues fixed the exponent to 1.0, as did Takada [31,45]. Byrd and Urban [38] cite Madey [46], who determined an exponent of 0.9. To explore the range of behaviors associated with different exponents when using the exponential

functional form (Eq. 3-4), the variable *d* was fixed to discrete values ranging from 0.9 to 1.1.

In order to fit coefficients for the semi-empirical models, the integrals in Eqs. 3-5 and 3-6 were evaluated numerically using the trapezoidal rule. The resulting sets of ordered pairs of energy and light output could then be interpolated to determine the light output (MeVee) corresponding to the measured data points' energy (MeV) values. The curve fitting toolbox was used to vary the coefficients and compare the light output to the measured values using a nonlinear least squares algorithm.

All of the fitted light output equations are displayed in Table 3-2; a subset of the fits is displayed in Fig. 3-2. The fit from Enqvist and colleagues [31] is shown for reference.

Table 3-2. 12.7 cm thick x 12.7 cm diameter EJ-309 detector neutron light output model coefficients and goodness of fit values. Italics indicate coefficients that were fixed during the fitting process.

Form	*a*	*b*	*c*	*d*	*SSE*	*R^2*	*RMSE*	*ID*
Exponential	*0.748*	*2.41*	*0.298*	*1.000*	*0.0037*	*0.9998*	*0.0096*	*Exponential1**
	0.944	*6.25*	*0.144*	*0.900*	*0.0028*	*0.9998*	*0.0087*	*Exponential2*
	0.782	*2.98*	*0.251*	*0.950*	*0.0024*	*0.9998*	*0.0080*	*Exponential3*
	0.634	*1.45*	*0.427*	*1.050*	*0.0028*	*0.9998*	*0.0086*	*Exponential4*
	0.605	*1.24*	*0.477*	*1.100*	*0.0031*	*0.9997*	*0.0091*	*Exponential5*
Rational	*0.7836*	*5.523*			*0.0026*	*0.9998*	*0.0082*	*Rational6*
Polynomial	*0.03937*	*0.2062*	*-0.1454*		*0.0031*	*0.9997*	*0.0090*	*Polynomial7*
Birks	*2.277*	*33.84*			*0.0062*	*0.9995*	*0.0126*	*Birks8*
	1	*11.12*			*0.0635*	*0.9947*	*0.0398*	*Birks9*
Voltz	*0.9134*	*6.854*	*0.07178*		*0.0026*	*0.9998*	*0.0083*	*Voltz10*
	1	*8.345*	*0.09375*		*0.0033*	*0.9997*	*0.0093*	*Voltz11*
Power Law	*0.1387*	*1.618*			*0.0055*	*0.9995*	*0.0119*	*Power***

** Fit from* [31].
*****Power Law fit was not used during post-processing using MPPost of MCNPX-PoliMi simulations.***

From examination of Table 3-2, it is apparent that most of the models give "good" fits to the data points (high R^2, low SSE). It would be difficult to choose the best

parameterization in a non-arbitrary way based on these metrics. Fig. 3-2 shows the measured light output data and six of the models on a log-log scale covering proton recoil energies from 10 keV to 7 MeV. It is clear that different models shown diverge significantly from one another, especially at low energy, while they all fit the measured data points well.

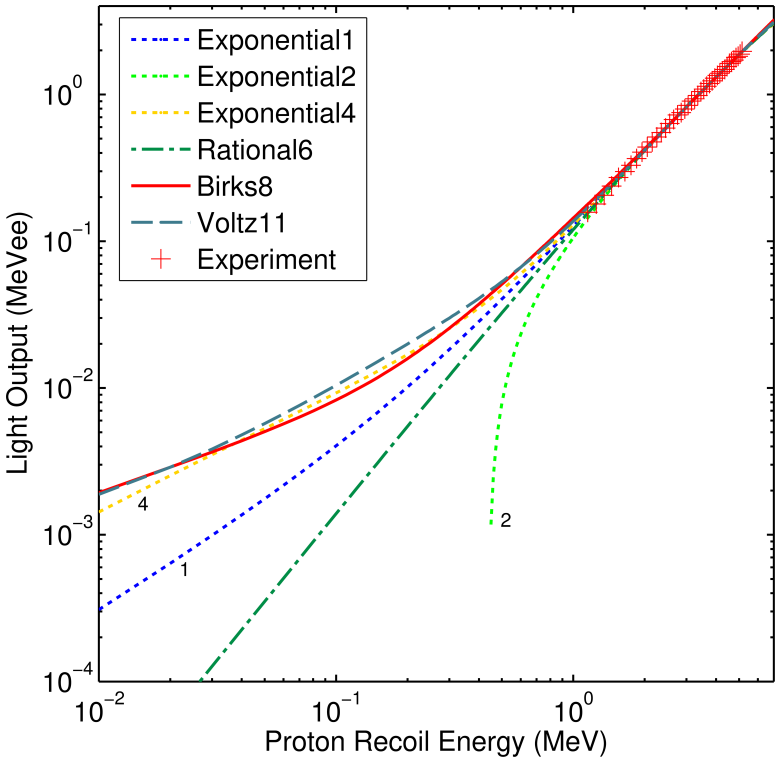

Figure 3-2. Log-log plot showing the measured light output data points for the 12.7 cm thick by 12.7 cm diameter EJ-309 detector as well as a subset of the various fits extrapolated from 0.01 to 7 MeV proton recoil energy. For legibility, not all fits tested are plotted. The fits shown were selected to illustrate the divergent behavior at low energy.

Further, the extrapolations of the exponential functional form are sensitive to the value of variable *d*. The later sections of this paper show that an exponent greater than 1 is required to give the best results at low energies; a possible explanation for this based on the behavior of the proton stopping power will be discussed in Section 5.0.

In light of the many options available, choosing a model is challenging. An independent way to test and validate, or at least inform, the choice of model is required. The nonlinear nature of the light output requires consideration of each individual neutron scatter event in the detector. For our work we used the Monte Carlo code, MCNPX-PoliMi [33]. Each energy deposition was converted to light using an enhanced version of the post-processing code MPPost [34] that allows the use of the Birks and Voltz models.

3.5 Validation Measurement Methodology

In order to test light output coefficients, a validation measurement using a well-known source was conducted as a baseline. We measured spontaneous fission neutrons from a recently manufactured ^{252}Cf source, calibrated by the vendor with a 5% tolerance. At the time of the measurement, the source strength was calculated to be 5.44 mCi, with a spontaneous fission rate of 6.23×10^6 fissions/s and a corresponding neutron emission rate of 2.34×10^7 neutrons/s. The uncertainty on these values is estimated to be 5%.

The same 12.7cm thick x 12.7 cm diameter cylindrical EJ-309 liquid detector coupled to a Photonics XP4512B PMT that was used for the *L(E)* measurement was used to measure the ^{252}Cf source. The detector was placed at a distance of 116.4 cm from the source. A 7.62cm thick x 7.62cm diameter cylindrical EJ-309 liquid detector coupled to a ET-Enterprises 9821B PMT was also used and placed 112.7 cm from the source.

The voltage output was measured from the anode of the PMT and digitized using a CAEN DT5720 12-bit 250-MHz waveform digitizer. Neutron and photon pulses were discriminated using the charge-integration method [47], in which the integrals of two different time windows corresponding to the “tail” and the “total” pulse are compared. Fig. 3-3 shows a log-scale histogram of a subset of the measured data plotted with the tail

integral versus the total integral. The upper distribution means the pulse had a larger "tail" component than in the lower distribution, so the upper distribution corresponds to neutron pulses and the lower corresponds to photon pulses. For this work we utilized the software tool, SlicePSD [30] to generate the discrimination line in a robust and repeatable way. The SlicePSD generated discrimination line is displayed as the red line on Fig. 3-3.

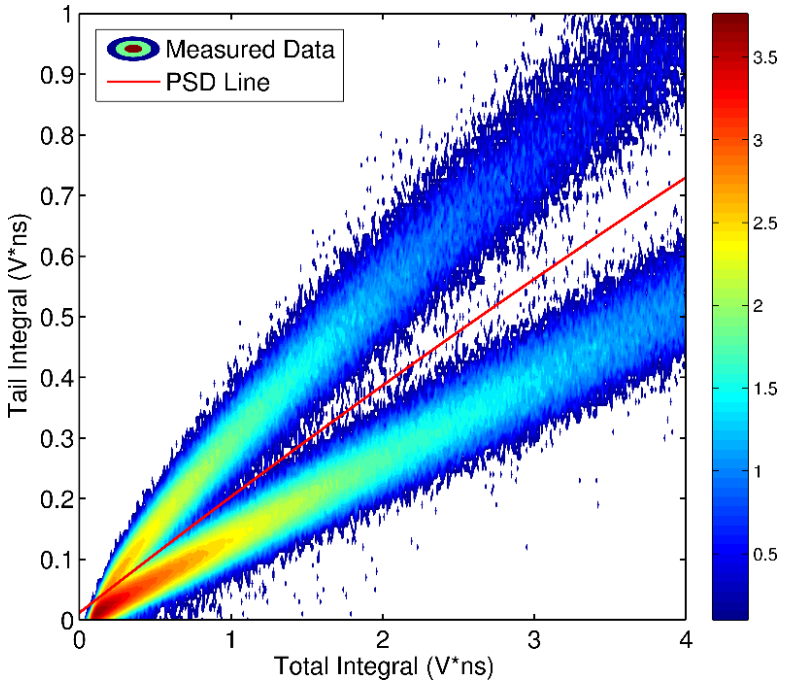

Figure 3-3. Log10 scale histogram of 252Cf pulses measured using the 12.7 cm thick x 12.7 cm diameter EJ-309 detector. The ordinate shows the integral of the "tail" of the pulses, while the abscissa shows the "total" integral of the pulses. The upper band corresponds to neutron pulses while the lower band corresponds to photon pulses. The discrimination line is shown in red.

The lower threshold was set to 0.02 V, which corresponded to approximately 32 keVee. The upper threshold was approximately 3.15 MeVee, due to the 2-V dynamic range of the digitizer.

The measured neutron PHD is shown in Fig. 3-4. The error bars shown are from counting statistics, corresponding to one standard deviation. The peak in the distribution is at ~0.08 MeVee – below that pulse height, particle misclassification is more prevalent.

The pulse shape discrimination (PSD) line was chosen to capture as many true neutrons as possible while avoiding the densest part of the gamma ray distribution to avoid excessive gamma ray misclassification (false positive neutrons). This line results in reduced neutron efficiency in this pulse height region, but greater confidence that the pulses selected were true neutrons rather than misclassified gamma rays.

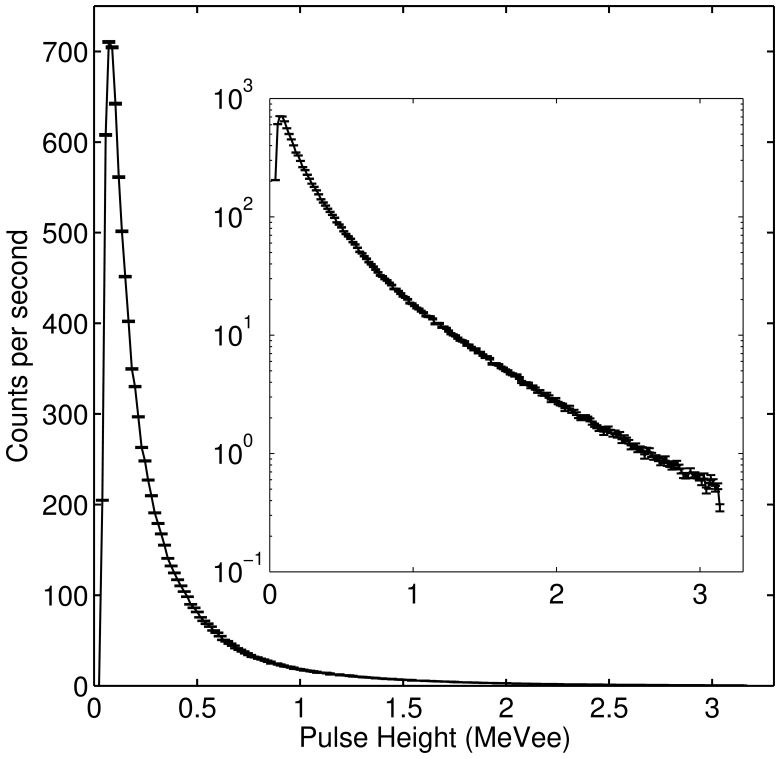

Figure 3-4. Measured ^{252}Cf neutron PHD. Error bars shown are based on counting statistics and correspond to one standard deviation. The inset shows the same data on a semi-log scale. The detector size is 12.7 cm thick x 12.7 cm diameter.

3.6 Simulation and Post-Processing: 12.7 cm x 12.7 cm Detector

A simplified model of the detector was created in MCNPX-PoliMi. PoliMi's built-in ^{252}Cf source was used, and energy depositing events were recorded in the cylindrical detector cell. MCNPX-PoliMi outputs a data file that tracks particle collisions, allowing the proper nonlinear light output to be generated due to multiple neutron events in the same history. For example, in the 12.7 cm x 12.7 cm detector, 68% of simulated

neutron events had at least two hydrogen scatters in the first three interactions. These data highlight the importance of treating the nonlinear light output correctly.

An enhanced version of MPPost was used to post-process the data files and generate PHDs. The modifications allowed the use of the Birks and Voltz light output equations in addition to the pre-existing polynomial, rational, and exponential forms. Gaussian resolution broadening was applied using the following relationship:

$$\frac{\Delta L}{L} = \sqrt{\alpha^2 + \frac{\beta^2}{L} + \left(\frac{\gamma}{L}\right)^2}, \tag{3-7}$$

with $\alpha = 0.102$, $\beta = 0.102$, and $\gamma = 0.036$ [13].

Fig. 3-5 shows the fractional error of simulated PHDs using the light output relationships in Table 3-2 as compared to measured data. Substantial variation in simulated PHDs occurs when the different fits are employed. In order to enhance the ability to determine the best agreement between simulated and measured PHDs, fractional difference plots were generated. These plots show the quantity $(S\text{-}M)/M$ in each bin, where S is the simulated number of counts and M is the measured number of counts.

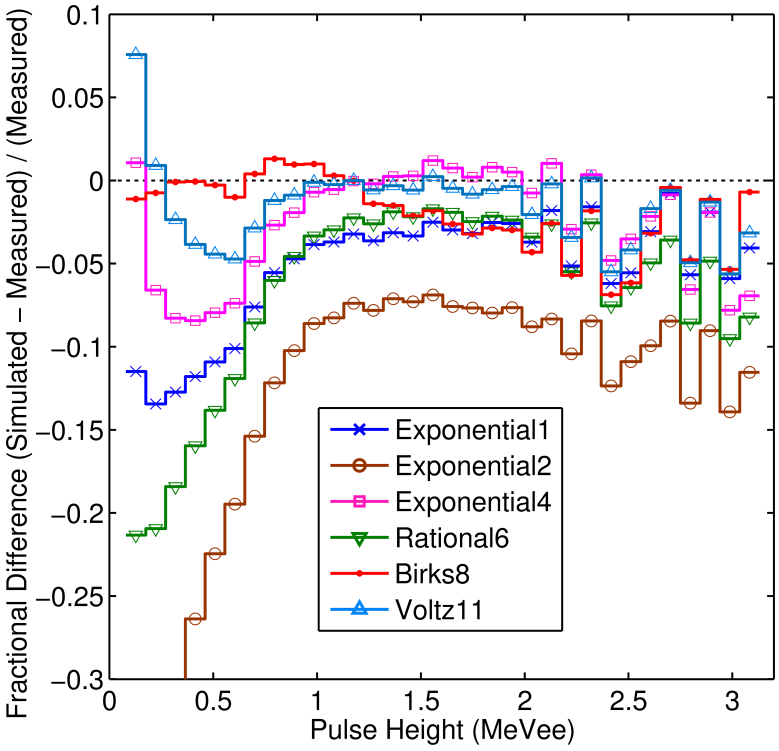

Figure 3-5. Fractional error of simulated PHDs for a selection of the tested light output functions. The best overall results were obtained using Birks8.

The exponential functional form with *d* equal to 1.05 (Exponential4) results in the best agreement of the tested exponential models, but still has a tendency to under-predict the count rate at lower pulse heights. Birks8 performs the best over the full range of energies and pulse heights considered here. Using Birks8, we achieved better than 5% bin-by-bin agreement between simulated and measured PHDs over the range 0.08 to 2.18 MeVee, and better than 10% bin-by-bin agreement between 2.18 and 3.13 MeVee.

The simulated PHD with Exponential2 (*d* equal to 0.9) significantly under-predicts the measured PHD over the full range. These results demonstrate that the low-energy behavior of the light output fit affects the whole PHD, even when the fit and the *L(E)* data points agree well in their energy range. The Exponential2 model has a rapid dropoff in light output below the fitted range, which results in two main effects: an

increased minimum neutron energy deposition to exceed the threshold, and, importantly, a reduction in the total light produced for many neutron pulses due to multiple scatter events. The reduction in light from the secondary scatters in multiple scatter events accounts for the underprediction of the simulation at pulse heights higher than ~1 MeVee, even though the fit in Fig. 3-2 agrees well in that range.

We also compared the simulated total counts from 0.08 to 3.13 MeVee to the experimental data. The results are presented in Table 3-3. The total counts agree within 1% using the Birks8 model, while the previous Exponential1 model differs by 11%. Below 0.08 MeVee, the simulated PHD exceeds the measured PHD due to particle misclassification in the measurement.

Table 3-3. Comparison of simulated (ΣS) and measured (ΣM) total counts from 0.08 to 3.13 MeVee for the 12.7 cm x 12.7 cm detector.

Model	$\frac{\Sigma S - \Sigma M}{\Sigma M}$
Exponential1	*-11.0%*
Exponential2	*-33.6%*
Exponential4	*-3.5%*
Rational6	*-17.4%*
Birks8	*-0.7%*
Voltz11	*+1.8%*

Fig. 3-6 reprises Fig. 3-2 but adds data from the classic reference for neutron light output on protons, carbon, and alphas, Verbinski and colleagues [48], and expands the high-energy extrapolation to 50 MeV. The Birks fit (Birks8) can be seen at higher energies to approach and then exceed the line L(E)=E, which is not physical. The best Voltz fit (Voltz11) and the best exponential fit (Exponential4) both behave more plausibly in the high energy extrapolation. In order to explore that region more fully, a

similar experiment and simulation validation would need to be conducted at high energies.

There are significant differences between the detectors and measurement techniques used in this work and the ones from Verbinksi's, so the Verbinski data are not expected to perfectly agree with our data. However, it can be seen that these fits follow the general S-shape of the Verbinski data on log-log axes. This shape is inferred to be characteristic of proton light output in organic scintillators. The proton stopping power in EJ-309 liquid scintillator reaches a peak at 0.07 MeV. Below 0.07 MeV, the stopping power and thus quenching, is reduced, so the maximum quenching occurs near 0.07 MeV, causing an inflection point in the light output. In the case of Birks and Voltz, the stopping power is used directly, so this effect is captured. In the case of the exponential, this reduction in very low energy quenching could explain the better agreement achieved by setting the exponent d greater than 1.

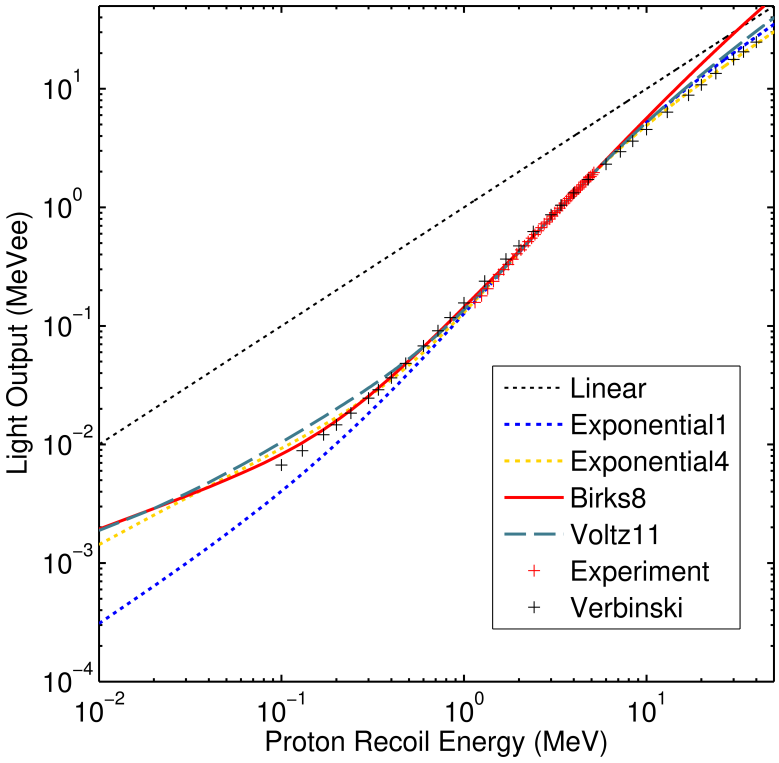

Figure 3-6. Log-log plot showing the measured light output data points for the 12.7 cm thick by 12.7 cm diameter EJ-309 detector as well as the various fits extrapolated from 0.01 to 7 MeV proton recoil energy. Additionally, the NE-213 neutron light output data from Verbinski is shown. [48]

3.6.1 Results for 7.62 cm x 7.62 cm EJ-309 Detector

We also reexamined the neutron light output data from Enqvist and colleagues [31] for the 7.62 cm x 7.62 cm detector, but used an updated energy deposition calibration point. We used the following calibration method for all of the data presented in this work, but the effects of miscalibration are most clearly demonstrated by the 7.62 cm x 7.62 cm data, so we present it here.

We determined that the Cs-137 Compton edge calibration point used to generate the fit in [13] was 0.290 V, corresponding to 478 keVee. To check that calibration point, we used a method similar to that of [49]; we simulated an unbroadened PHD due to Cs-137 gamma-ray interactions in the detector, applied varying resolution functions, and

scaled and matched the measured PHD to the simulation to determine the appropriate calibration point.

Fig. 3-7 shows the new calibration point determined using this method. The black dotted line shows the simulated PHD due to Cs-137, with no resolution broadening applied. The Compton edge is located at the straight vertical line. After applying resolution broadening, the fractional edge of the broadened peak corresponding to the Compton edge could be determined by finding the intersection of the vertical line and the broadened distribution. This fractional edge value was then applied to the measured PHD, and the distributions scaled to match the peak heights. This process was iterated over a variety of resolution functions and the best agreement was chosen by visual inspection; in future work an automated test of agreement can be used. A resolution function with a value of 15% at 478 keV resulted in a fractional edge of 83% and a calibration point of 0.3065 V.

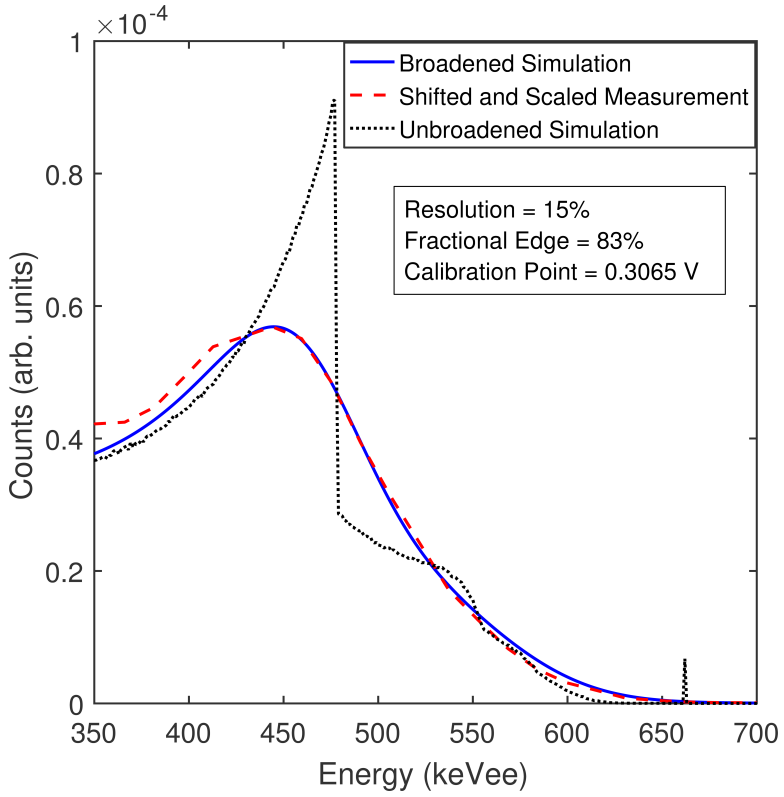

Figure 3-7. The calibration point for the 7.62 cm x 7.62 cm EJ-309 detector used in the L(E) measurement. The black dotted line shows the simulated PHD due to Cs-137 662 keV gamma rays in the detector, without resolution broadening. The solid blue line and dashed red line show the broadened simulation and calibrated measured PHDs.

The new calibration point resulted in a reduction of 5.7% of the light output for each energy-light output pair compared to [31]. The new light output data points were fitted to the exponential, Birks, and Voltz models. The coefficients for the resultant fits are listed in Table 3-4. The fractional differences between the validation measurement of ^{252}Cf neutrons and the simulated PHD are shown in Fig. 3-8. The agreement using any of these fits is a significant improvement over the function in [31] (Exponential1). The integrated counts from 0.09 to 3.2 MeVee agreed to within 3.5% using Birks8, 2% using Voltz11, and within less than 1% using Exponential2 (d = 1.05), while the previous exponential fit, Exponential1, differed by 13%. The fractional difference curves of Fig. 3-8 are not as "flat" as the ones shown in Fig. 3-5 for the 12.7 cm by 12.7 cm detector. The

slight remaining slope in Fig. 3-8 could be due to detector-specific variation (the detector used for the validation was the same type as the one used to measure the light output, but not the identical detector) or to an unknown systematic error in the original experimental data.

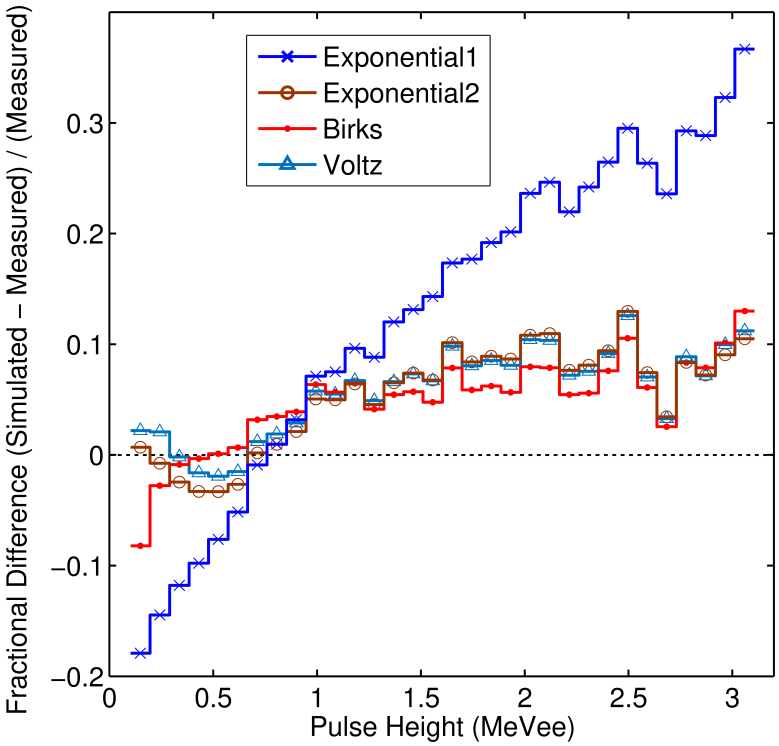

Figure 3-8. Fractional error of simulated PHDs for a selection of the tested light output functions. The detector size is 7.62 cm thick x 7.62 cm diameter.

Table 3-4. Light output model coefficients for the 7.62 cm thick x 7.62 cm diameter EJ-309 detector. Italics indicate coefficients that were fixed during the fitting process.

Form	*a*	*b*	*c*	*d*	*SSE*	*R^2*	*RMSE*	*ID*
Exponential	*0.817*	*2.63*	*0.297*	*1.000*	*0.1694*	*0.9694*	*0.0764*	*Exponential1**
	0.668	*1.63*	*0.387*	*1.050*	*0.0040*	*0.9993*	*0.0121*	*Exponential2*
Birks	*1.903*	*26.03*			*0.0043*	*0.9992*	*0.0124*	*Birks*
Voltz	*1*	*8.447*	*0.1072*		*0.0039*	*0.9993*	*0.0183*	*Voltz*

Fit from [31].

Table 3-5. Comparison of simulated (ΣS) and measured (ΣM) total counts from 0.08 to 3.13 MeVee for the 7.62 cm x 7.62 cm detector.

Model	$\frac{\Sigma S - \Sigma M}{\Sigma M}$
Exponential1	*-11.7%*
Exponential2	*-0.2%*
Birks	*-3.3%*
Voltz	*+1.6%*

3.7 Discussion

It is necessary to use a light output model that is robust in extrapolation to low energies. Typically, accurate light output measurements at low energies become difficult due to accelerator, source, or geometric constraints, imposing an effective threshold. Creative experiment design can alleviate some of these issues, and indeed there is a need for robust measurement of the light output from neutrons depositing low amounts of energy. In any event, if one chooses a model that is physics-based and realistic, one can be more confident in extrapolation to energies below the measured light output data points.

We performed a comprehensive study of a variety of possible scintillator light output models. Our results add to the body of work supporting the theory that light output quenching is proportional to stopping power. Both of the semi-empirical models we tested account for this effect.

The stopping power data are readily available in the SRIM package. Once the initial integration functions are established, the semi-empirical forms are not difficult to use. The lookup table of L(E) that is generated can be used in both directions.

An advantage of the semi-empirical forms is that some of the coefficients are material dependent, while others are expected to be detector and calibration dependent. It may be the case that the same parameterization can be used for multiple detectors of the same type, and it may further be possible to adjust for detector-to-detector variations in a logical way by adjusting only the detector-dependent parameters.

The determination of the MeVee/MeV calibration scale is of great importance in this type of work. A difference as small as 0.01 V in the identified Compton edge location can significantly change the "steepness" of the light output curve, affecting the fitted coefficients and in turn the simulated PHDs and other derived parameters. The best effort to calibrate to the true Compton edge, accounting for detector resolution and multiple scatters, must be made. Uncertainties in this area can be mitigated by ensuring that the calibration method used for the generation of the light output curve is the same as that used for the validation measurement, but it is clearly preferable that the calibration point be as close as possible to the "true" Compton edge pulse height.

We suspect that some difficulties previously encountered with neutron unfolding on the basis of simulated response matrices may be ameliorated by the use of more accurate light output models. The light output changes the effective thresholds and strongly influences energy-dependent efficiency, which is a key parameter in unfolding algorithms.

In general, researchers should make every effort to obtain the best possible light output data for their specific detectors, generate fits using the semi-empirical forms, and test their results using a Monte Carlo code such as MCNPX-PoliMi (available through RSICC). If measuring the light output directly is not an option, caution must be utilized

when applying light output functions and coefficients generated by other researchers—even a small difference in calibration or measurement technique can cause significant deviations. While the entire process is highly sensitive, we have shown that if great care is taken, excellent agreement between simulation and measurement can be obtained.

3.8 Summary and Conclusions

The neutron light output data of Enqvist and colleagues [31] were analyzed with a variety of light output equations. The extrapolations of these equations were shown to diverge widely, especially at low energy. A measurement of neutrons from a ^{252}Cf source and simulation of the same were validated against each other, utilizing the various equations. The best equations resulted in the best agreement between simulation and measurement. We achieved better than 5% bin-by-bin agreement between simulated and measured PHDs over the range 0.08 to 2.18 MeVee, and better than 10% agreement between 2.18 and 3.13 MeVee. The integrated counts from above 0.08 MeVee agree within 1% using the Birks8 model, while the previous Exponential1 model differed by 11%. Below 0.08 MeVee, the simulated PHD exceeds the measured PHD due to particle misclassification in the measurement.

We have demonstrated that the choice of model to represent the neutron light output from organic scintillators as a function of energy deposited is a critical step in detector characterization. A wide variety of models can be chosen from the literature, and most allow good fits to measured light output data. It is not possible, therefore, to select among them only on the basis of fit quality. A good fit to the data is necessary, but not sufficient.

Extrapolation to lower energies is particularly sensitive to the functional form used. Low-energy collisions cannot be neglected because neutrons can undergo multiple scatters in organic scintillators; multiple sub-threshold scatters can generate an amount of light that exceeds the threshold, and sub-threshold scatters can be present in larger pulses as well. The summation is nonlinear and the result depends strongly on the light output model used.

Therefore, the use of a detector response code to thoroughly test the selected model and fitted coefficients is beneficial. MCNPX-PoliMi and MPPost have been shown to be effective codes for this purpose, in conjunction with validation experiments using a neutron source with a well-known energy spectrum and emission rate, such as a recently-calibrated ^{252}Cf spontaneous fission source.

The semi-empirical light output equations proposed by Birks and Voltz are grounded in theory and make use of stopping power data to model quenching. The stopping power dependence enables fitting of coefficients at light outputs where the data are easier to obtain and/or more reliable and guides extrapolation to low energies with greater confidence than that provided by the more arbitrary parameterizations. We have shown that the Birks model works particularly well for EJ-309 liquid scintillation detectors of two different sizes (right cylindrical cells, 12.7 cm x 12.7 cm and 7.62 cm x 762 cm), and achieved excellent agreement between our simulated and measured ^{252}Cf neutron PHDs.

Chapter 4 Carbon Recoil Response

4.1 This Chapter

In this chapter, we present the first measurements of energy-dependent light output from carbon recoils in the liquid organic scintillator EJ-309. For this measurement, neutrons were produced by an associated particle deuterium-tritium generator and scattered by a volume of EJ-309 scintillator into stop detectors positioned at four fixed angles. Carbon recoils in the scintillator were isolated using triple coincidence among the associated particle detector, scatter detector, and stop detectors. The kinematics of elastic and inelastic scatter allowed data collection at eight specific carbon recoil energies between 2.86 and 3.95 MeV. We found the light output caused by carbon recoils in this energy range to be approximately 1.14% of that caused by electrons of the same energy, which is comparable to the values reported for other liquid organic scintillators. A comparison of the number of scattered neutrons at each angle to a Monte Carlo N-Particle eXtended simulation indicates that the ENDF/B-VII.1 evaluation of differential cross sections for 14.1 MeV neutrons on carbon has discrepancies with the experiment as large as 55%, whereas those reported in the JENDL-4.0u evaluation agree with experiment.

These results were recently submitted for publication as a journal article, “Light Output Response of EJ-309 due to Neutron Elastic and Inelastic Scatter on Carbon,” [50].

4.2 Introduction

Organic scintillator detectors are used as fast neutron detectors in a variety of applications. Detector systems employing organic scintillators exist or are under development with applications including nuclear nonproliferation and international safeguards [5], nuclear medicine [17], neutrino detection [18], and weakly interacting massive particle (WIMP)/dark matter detection [20,21,51]. Organic scintillators have several desirable attributes as neutron detectors [28] including fast timing properties, pulse shape discrimination capabilities, and some spectroscopic capability because of the preservation of information about the energy of incident neutrons.

As the application space for organic scintillators expands, the demands for increasingly accurate light output data increase. Advanced neutron imaging detection systems rely on light output data to accurately reconstruct neutron source locations [12]. Dosimetry systems use light output data to determine the energy deposited in each event, enabling energy-dependent flux-to-dose conversions [52]. In many nonproliferation applications, it is desirable to reduce the detection threshold to increase the efficiency of the detector system, which typically increases the sensitivity and reduces the required measurement time.

A large body of work exists about characterizing the light output in organic scintillators because of the interactions between neutrons and hydrogen nuclei [16,31,43,48,53–56]. However, in some application areas, improvements to carbon light output data would benefit the analysis of experimental data and the fidelity of Monte Carlo simulated detector response. For example, in some WIMP studies, interactions with carbon are expected to provide the sought-after signal [20,51]. In neutron detection

applications, as neutron energy increases, so does the importance of accurately accounting for the light from carbon recoils; at higher energies, the interaction cross section for carbon exceeds that of hydrogen. Examples of the use of high-energy neutrons include active interrogation systems that use 14.1 MeV neutrons from deuterium-tritium (D-T) neutron generators for nonproliferation applications and external beam radiation therapy systems for medical applications that produce neutrons with energies as high as 250 MeV.

Publications reporting the light output resulting from carbon interactions are scarce [48,53,57,58]. One contributing factor is the difficulty of isolating instances of carbon-only interactions. The carbon signal is usually dominated by the hydrogen signal, and careful experimental design is required to isolate and extract the carbon signal. This paper reports an effective method for characterizing the light output from single-scatter events on carbon nuclei in organic scintillator detectors that uses both elastic and inelastic scatter reactions and presents the first measurements of the light output for carbon recoils in EJ-309 [22] in the energy range of 2.86–3.95 MeV.

4.3 Background

Neutrons deposit energy in organic scintillators through scattering on hydrogen and carbon nuclei, and the recoiling nuclei interact with the scintillation molecules to produce scintillation light. Figure 4-1(a) shows the cross sections for three interaction channels: elastic scatter on hydrogen and elastic and inelastic scatter (to the first excited state) on carbon, for the energy range from 0.1 to 20 MeV. At low energies, the hydrogen cross section dominates, but as neutron energy increases the carbon elastic scatter cross section approaches and then surpasses hydrogen. The inelastic scatter cross section

exhibits a low-energy threshold because the incident neutron must have sufficient energy to excite the carbon nucleus to its first excited state.

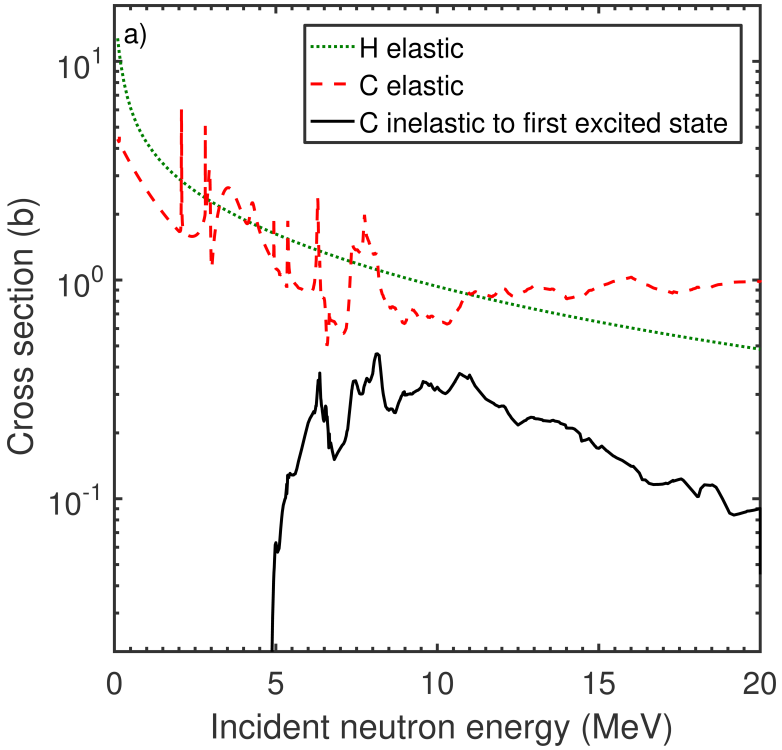

Figure 4-1 (a) Elastic and inelastic neutron scattering cross sections on hydrogen and carbon [59].

In previous characterization of proton light output in scintillators [16,31,60], the investigators used the approach of Kornilov [43] to identify the pulse heights corresponding to single proton recoils. The method uses the time-of-flight of neutrons from a white neutron source to determine the incident energy. Neutrons can deposit any fraction of their energy to recoil protons, so each neutron energy bin produces a broad PHD. Moreover, multiple scatter events are common in organic scintillators of appreciable size, carbon scatter events occur, and detector resolution broadens what would otherwise be a clear "edge" corresponding to full-energy depositions to a single

proton. Therefore, to determine the appropriate pulse height-to-energy relationship, one must either take a fraction of the edge or use Kornilov's approach of taking the derivative of the PHD and fitting a Gaussian to the result, where the mean of the Gaussian corresponds to the single full-energy proton event. However, these techniques cannot be used to determine carbon light output because the carbon signal is dominated by the proton and multiple-scatter signals.

In 1964, Steuer and Wenzel [58] measured carbon recoil detector response in NE-102 and NE-213 using deuterium-deuterium and D-T neutrons and a backscatter geometry. They discriminated against inelastic scatters by using detector bias in their stop detectors to only accept pulses from the higher-energy neutrons following elastic scatter and considered the remaining contribution negligible. In 1968, Verbinski et al. [48] presented light output data for NE-213 for proton, α, and carbon recoil ions, which remain the reference for the EJ-301 (same composition as NE-213) specification sheet today [61]. The details of the carbon light output measurement can be found in [53]. The authors used D-T neutrons, a scatter angle of 110°, a high bias in the stop detectors to remove the inelastic scatter events. More recently, as part of the WIMP search, the KamLAND liquid scintillator was characterized using a monochromatic neutron beam and forward-scattering angles, and the authors used time-of-flight to reject inelastic events [18].

No studies were identified that characterized carbon recoil response in EJ-309 or that used both the elastic and inelastic scatter events. EJ-309 is similar in composition to EJ-301 and NE-213, but EJ-309 was modified to have a high–flash point to eliminate the fire hazard associated with EJ-301 and other low–flash point liquid scintillators [22]. EJ-

309 is therefore an attractive liquid scintillator material for nonproliferation and safeguards applications.

4.4 Experimental Design

Figure 4-2 shows a schematic diagram of the experimental setup. A monoenergetic neutron source is placed some distance from the detector being characterized, which is referred to as the scatter detector). Another detector (the stop detector) is placed some distance away from the scatter detector, and coincidences between the scatter and stop detectors are used to identify neutrons that scattered at the specific angle (θ) in the laboratory frame of reference, defined by the direction of the incoming and outgoing neutron.

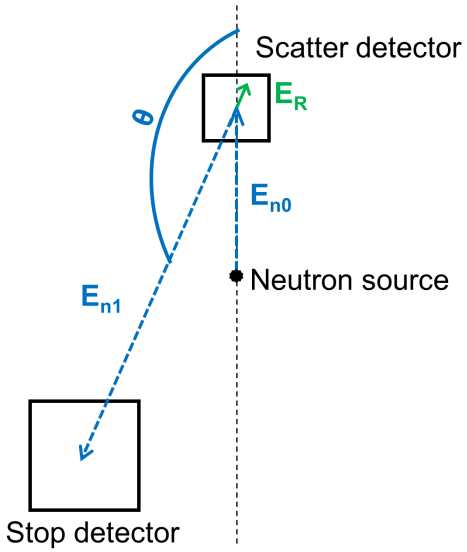

Figure 4-2 Schematic diagram of the experimental setup and nomenclature.

4.4.1 Scattering kinematics

When neutrons elastically scatter on hydrogen or carbon, the energy of the scattered neutron can be expressed using Eq. 4-1,

$$E_{n1} = E_{n0} * \left[\frac{\cos\theta + \sqrt{A^2 - \sin^2\theta}}{A+1}\right]^2, \tag{4-1}$$

where E_{n0} is the incident neutron energy, E_{n1} is the outgoing neutron energy, θ is the scattering angle, and A is the mass number of the scattering nucleus.

In the case of neutrons scattering on hydrogen, scattering angles greater than 90° are not possible because of the nearly equal masses of neutrons and protons. Moreover, the maximum energy deposition on carbon occurs in a backscatter, when θ is equal to 180°.

Unlike hydrogen, neutrons can excite carbon nuclei via inelastic scatter. In this case, Eq. 4-2 (Shultis and Faw [62] Eq. 3.25) must be used to account for the Q-value of the excitation:

$$\sqrt{E_{n1}} = \frac{1}{A+1} * \left[\cos\theta \sqrt{E_{n0}} \pm \sqrt{E_{n0}(\cos^2\theta + A^2 - 1) + A(A+1)Q}\right]. \tag{4-2}$$

In Eq. 4-2, only the positive square root gives meaningful results for elastic scattering and most inelastic scattering. The minus sign only gives physical results when a neutron with energy only slightly greater than Q is inelastically scattered, a case that is not applicable in this work.

Figure 4-3 shows the variation of energy deposited and recoil ion energy with neutron scattering angle for carbon, for elastic scatter and inelastic scatter to the first state (Q = 4.439 MeV).

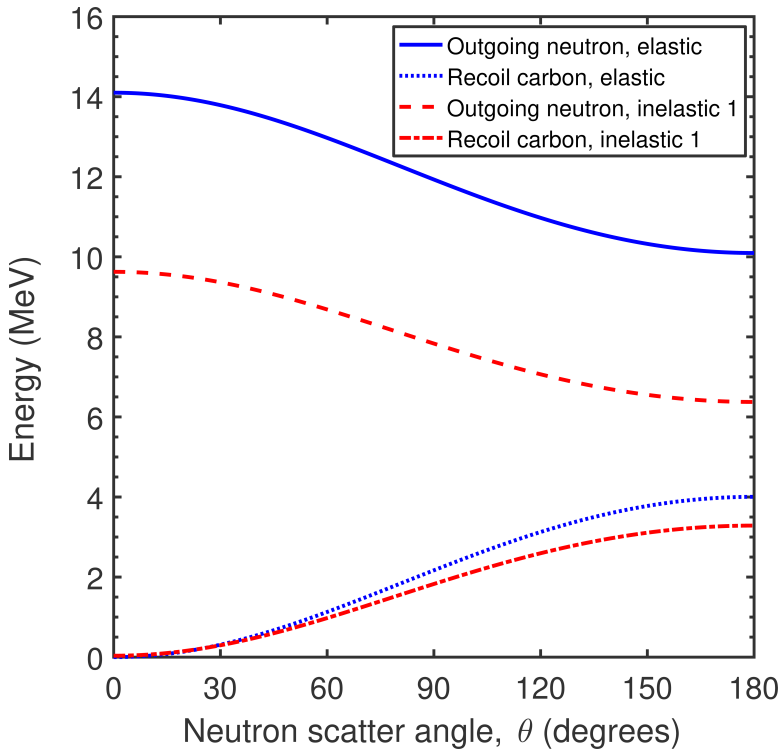

Figure 4-3 Outgoing neutron and recoil carbon energies as a function of neutron scatter angle for incident 14.1 MeV neutrons on carbon.

If the time between two neutron events is known, the time and distance between interactions can be used to determine the velocity and in turn the kinetic energy of the neutron, a technique known as neutron time-of-flight. Equation 4-3 presents this equation in relativistic terms. (The difference is ~1% at 14 MeV compared to the non-relativistic form).

$$E_n = \frac{m_n c^2}{\sqrt{1-(v/c)^2}} \quad (4\text{-}3)$$

Using the above relationships for scattering angle, energy deposition, and neutron kinetic energy, the single neutron scatters on carbon can be isolated by performing correlation measurements at fixed angles. As a consequence of Eq. 4-1, in a single elastic scatter on carbon, a neutron can deposit at most 28.4% of its energy. Therefore, we elected to use a D-T neutron generator, whose 14.1 MeV neutrons can deposit up to 4.0 MeV on carbon nuclei to create detectable pulses when interactions with carbon occur. We designed the experiment to use scattering angles of 132°, 140°, 155°, and 162°. The flight path was sufficiently long between the scatter and stop detectors to allow the neutrons following elastic and inelastic scatter to be distinguished from each other based on time-of-flight.

4.4.2 Experimental Facility and Equipment

The experiment was conducted at Oak Ridge National Laboratory in laboratory space operated by the Nuclear Material Detection and Characterization Group. A Thermo Fisher Scientific API-120 associated particle D-T neutron generator was used to generate 14.1 MeV neutrons. The D-T generator emitted an estimated 3.40×10^6 neutrons per second, over all angles. A YAP:Ce scintillator embedded in the D-T generator was used to detect α particles and identify neutrons emitted in the direction of the scatter detector. The associated neutrons were emitted in a cone with a half-angle of approximately 2°. The use of the α detector to electronically collimate the neutron source by requiring

coincidence between the α detector and the scatter detector served to reduce chance coincidences and overall data collection rates.

The active volume of the scatter detector was a 7.62 cm diameter × 7.62 cm depth right circular cylindrical cell of EJ-309 liquid scintillator viewed by an ET-Enterprises 9821B photomultiplier tube. The stop detectors were 12.7 cm diameter × 12.7 cm depth EJ-309 liquid scintillator cells coupled to Photonis XP4512B photomultiplier tubes.

Figure 4-4(a) shows a schematic diagram of the experiment performed at Oak Ridge National Laboratory. Figure 4-4(b) is a photograph of the experimental layout. The scatter detector was placed 72 cm from the D-T generator. The stop detectors were placed 200 cm ± 1 cm from the scatter detector. Four stop detectors were employed, placed at scattering angles of 132°, 140°, 155°, and 162°. Backscatter angles were employed to maximize the size of the carbon recoil pulses and the separation between the elastic and inelastic pulses. Shallower angles would allow measurement for lower carbon recoil energies, as well as proton recoil peaks (if less than 90°).

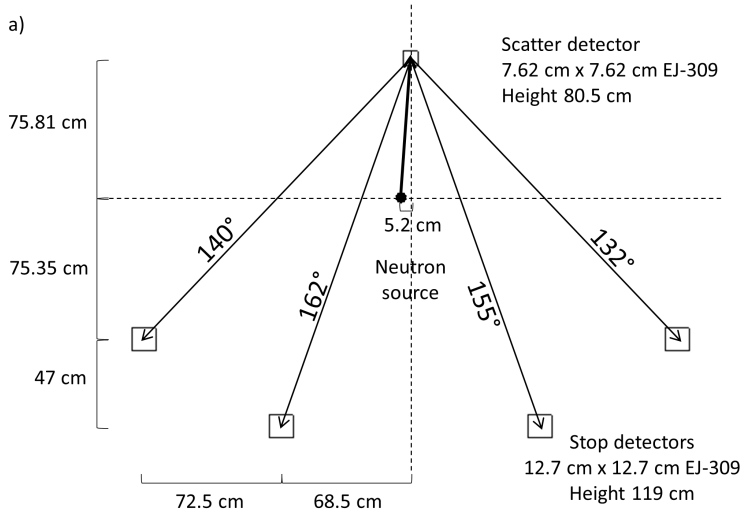

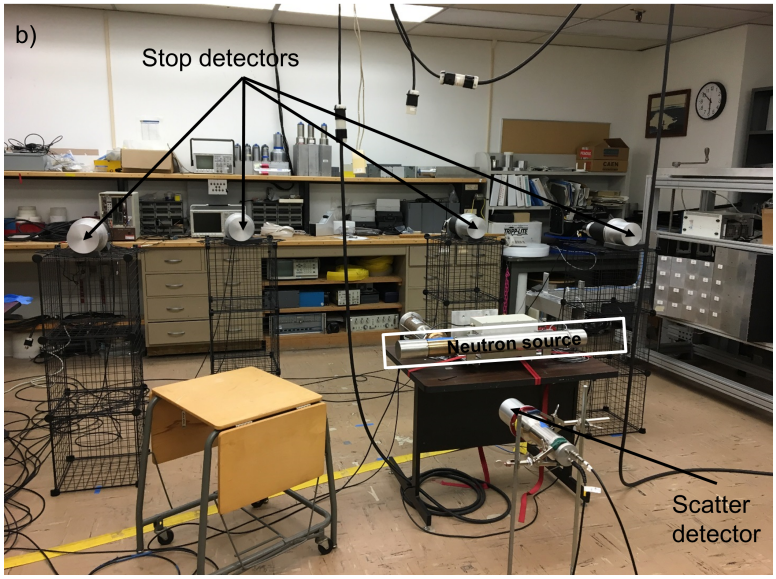

Figure 4-4 a) Detailed experimental schematic showing detector center positions and scattering angles. b) Photograph of the experimental setup.

Pulses from all six detectors (α, scatter, and stop) were digitized using a CAEN Electronics DT5730 desktop digitizer. The DT5730 is a 14-bit 500 MHz digitizer. Each channel can be set to a dynamic range of either 0.5 V or 2.0 V. The digitizer was programmed to require coincident triggers on the α, scatter and at least one stop detector to record waveforms to the hard drive.

4.5 Experimental Results and Analysis / Data Processing

4.5.1 Data Collection

The detectors were calibrated before and after the experiment using a ^{137}Cs γ ray source affixed to the center of the detector face. The light produced in organic scintillators is typically expressed in units of keVee or MeVee, where "-ee" refers to "electron-equivalent," or the amount of light that would be produced by a recoil electron of the corresponding energy. The scatter detector was calibrated to a relatively "high

gain" setting so that the 478 keV Compton edge was located near 0.57 V using the 2.0 V dynamic range; subsequently, the 0.5 V dynamic range was used for the scatter detector to allow better resolution at small pulse heights.

Figure 4-5 shows the calibration point determined using a methodology similar to Dietze and Klein [49]. The Monte Carlo N-Particle eXtended (MCNPX) [63] is used to simulate the photon transport and resulting PHD with no resolution applied. Then resolution is iteratively applied, and the simulation and measurement are normalized so that their maxima match. The intersection of the simulation and measurement indicates the correct Compton edge location.

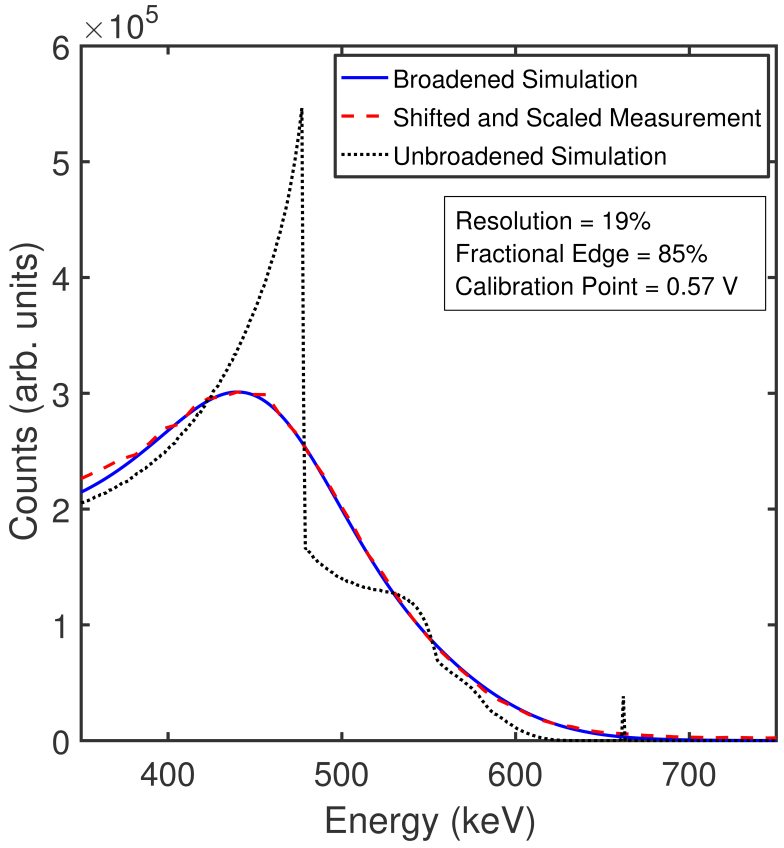

Figure 4-5 Calibration of scatter detector using ^{137}Cs Compton edge.

The calibration point drifted from 0.57 V before the measurements to 0.58 V. A value of 0.575 V is used for the remainder of the analysis. The stop detectors were calibrated to lower gain settings to avoid clipping the full energy deposition pulses of 6–10 MeV neutrons of interest. The Compton edges for these detectors were set to either 0.14 or 0.25 V.

Coincidence data were acquired for 18.5 hours, yielding a total of 2.26×10^{11} emitted neutrons. Figure 4-6 shows a histogram of the measured time-of-flight of γ rays and neutrons from the scatter detector to the stop detector at 162°. The peaks corresponding to neutron elastic and inelastic scatter can be seen at 49 and 61 ns.

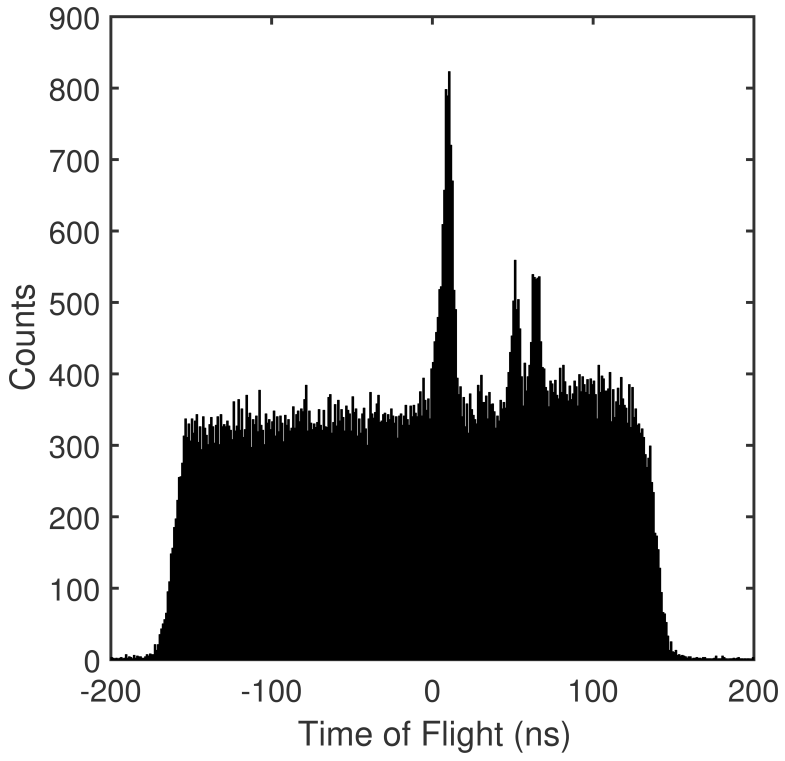

Figure 4-6 Measured time-of-flight between the scatter detector and the stop detector at 162°.

4.5.2 Data Analysis

Several gates were applied to the data to improve the signal-to-noise ratio. First, cuts were applied using charge-integration pulse shape discrimination [64]. Figure 4-7 shows the scatter detector tail-to-total ratio versus pulse height for all coincidences where the time-of-flight to a stop detector was between 40 and 70 ns. A tail-to-total ratio greater than 0.09 was required for the stop detector, and a tail-to-tail ratio greater than 0.05 was needed for the scatter detector. Additional gates required the pulse heights to be less than 0.2 V in the scatter detector and required the time between the α detector trigger and the scatter detector trigger to fall within the range of 12–18 ns.

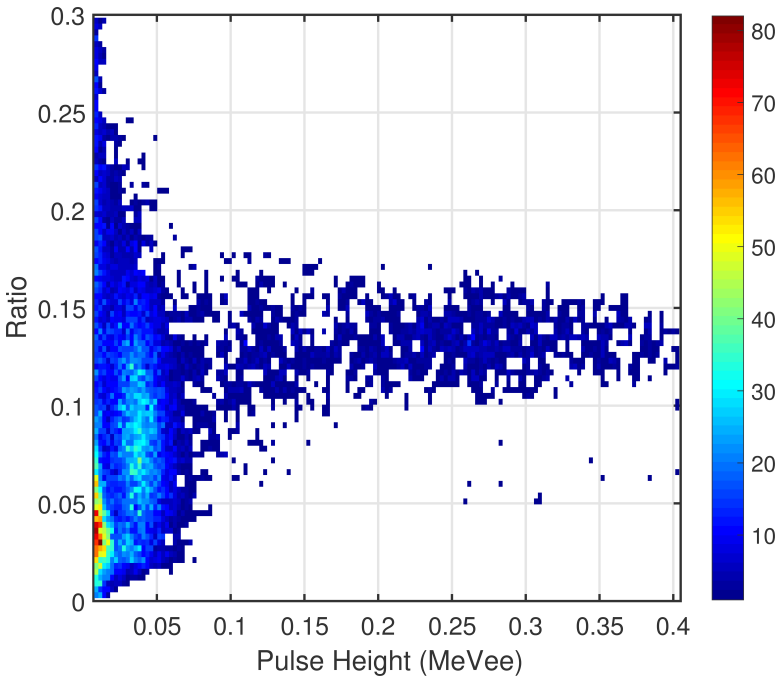

Figure 4-7 Histogram of scatter detector tail/total ratio versus pulse height for all coincidences where the time-of-flight to a stop detector was between 40 and 70 ns.

The resulting histogram after the above gates were applied is shown in Fig. 4-8. Now the peak-to-chance background ratio is substantially improved. The red region delineates the time-gated elastic scatter pulses, and the blue region delineates the time window used to extract pulses defined as chance coincidence background.

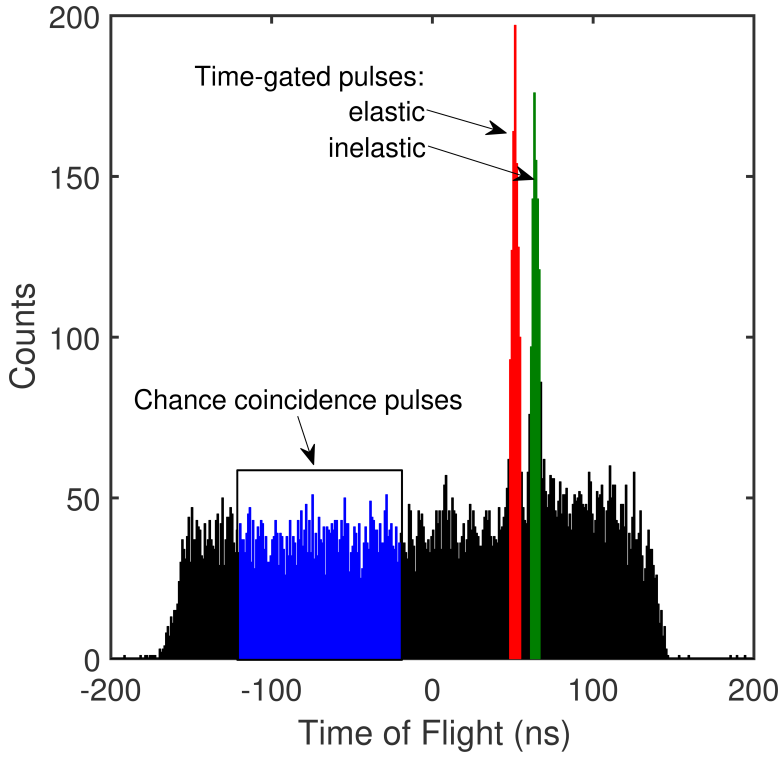

Figure 4-8 Measured time-of-flight between the scatter detector and the stop detector at 162°, after application of pulse shape, pulse height, and alpha time-of-flight gates. The red region indicates the time window for elastic scatter pulses, the green region indicates the time window for inelastic scatter pulses, and the blue region indicates the time window used to estimate the chance coincidence background pulses.

Fig. 4-9(a) shows the PHD of the corresponding pulses in the scatter detector. The chance coincidence PHD is scaled by the ratio of the time windows and then subtracted from the peak PHD. A Gaussian function is then fitted to the peak in the net PHD; Fig. 4-9(b) shows the net PHD and Gaussian fit for elastic scatters to the 162° stop detector, corresponding to 3.95 MeV carbon recoils. The same analysis is performed for the green

region, delineating the time-gated inelastic scatter (first state) pulses, shown in Figs. 4-9(c)–(d). Figures 4-10 through 4-12 show the remaining cases.

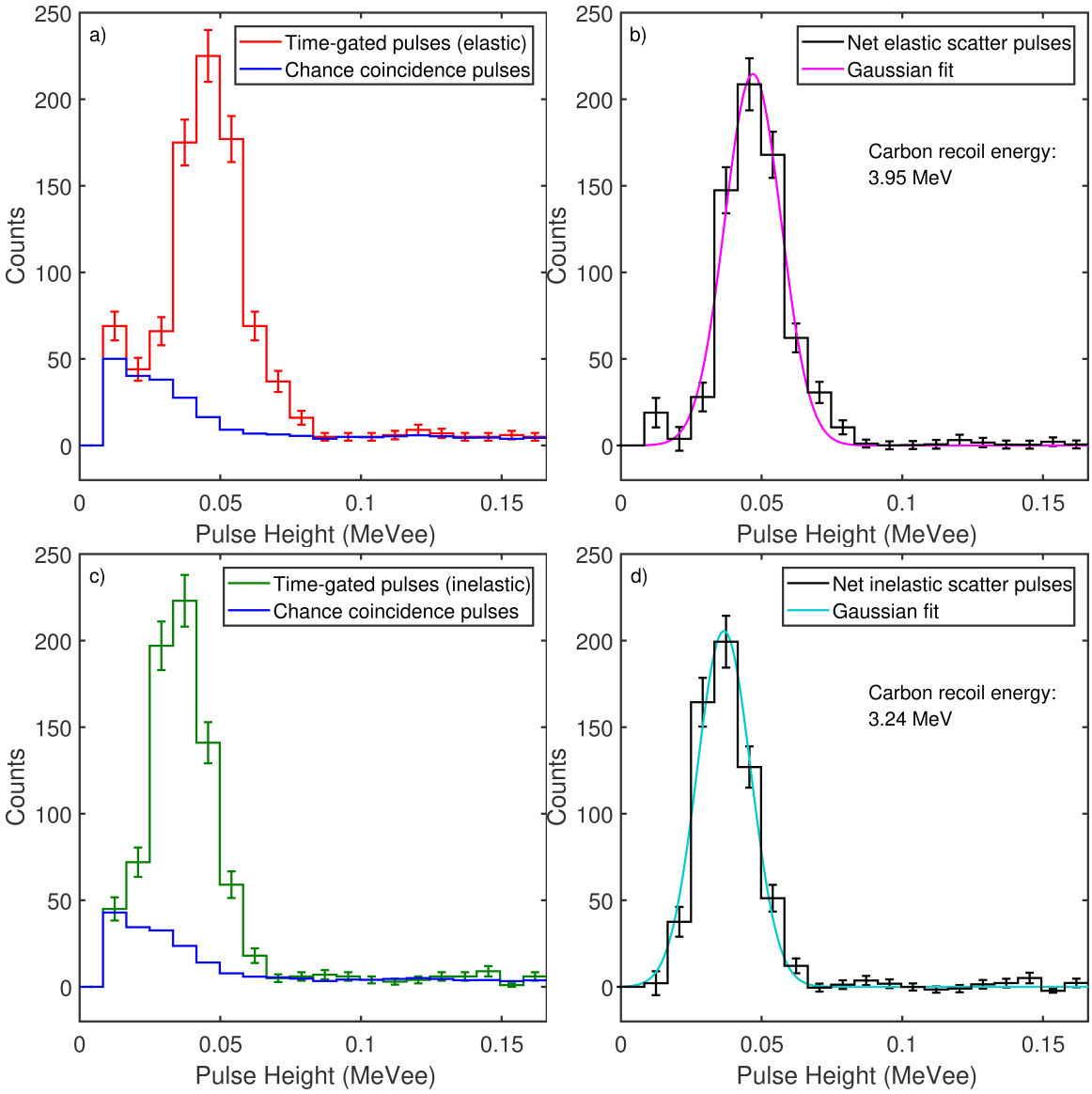

Figure 4-9 (a) The PHDs of time-gated elastic scatter pulses and chance coincidence pulses (adjusted by the ratio of the gate widths) in the 162-degree scatter detector, corresponding to the red and blue regions on Fig. 4-8. (b) The net PHD after subtraction of the chance coincidence background from the time-gated elastic scatter pulses, and the Gaussian fit to the result. (c) The PHDs of time-gated inelastic scatter pulses and chance coincidence pulses (adjusted by the ratio of the gate widths) in the 162-degree scatter detector, corresponding to the green and blue regions on Fig. 4-8. (d) The net PHD after subtraction of the chance coincidence background from the time-gated inelastic scatter pulses, and the Gaussian fit to the result.

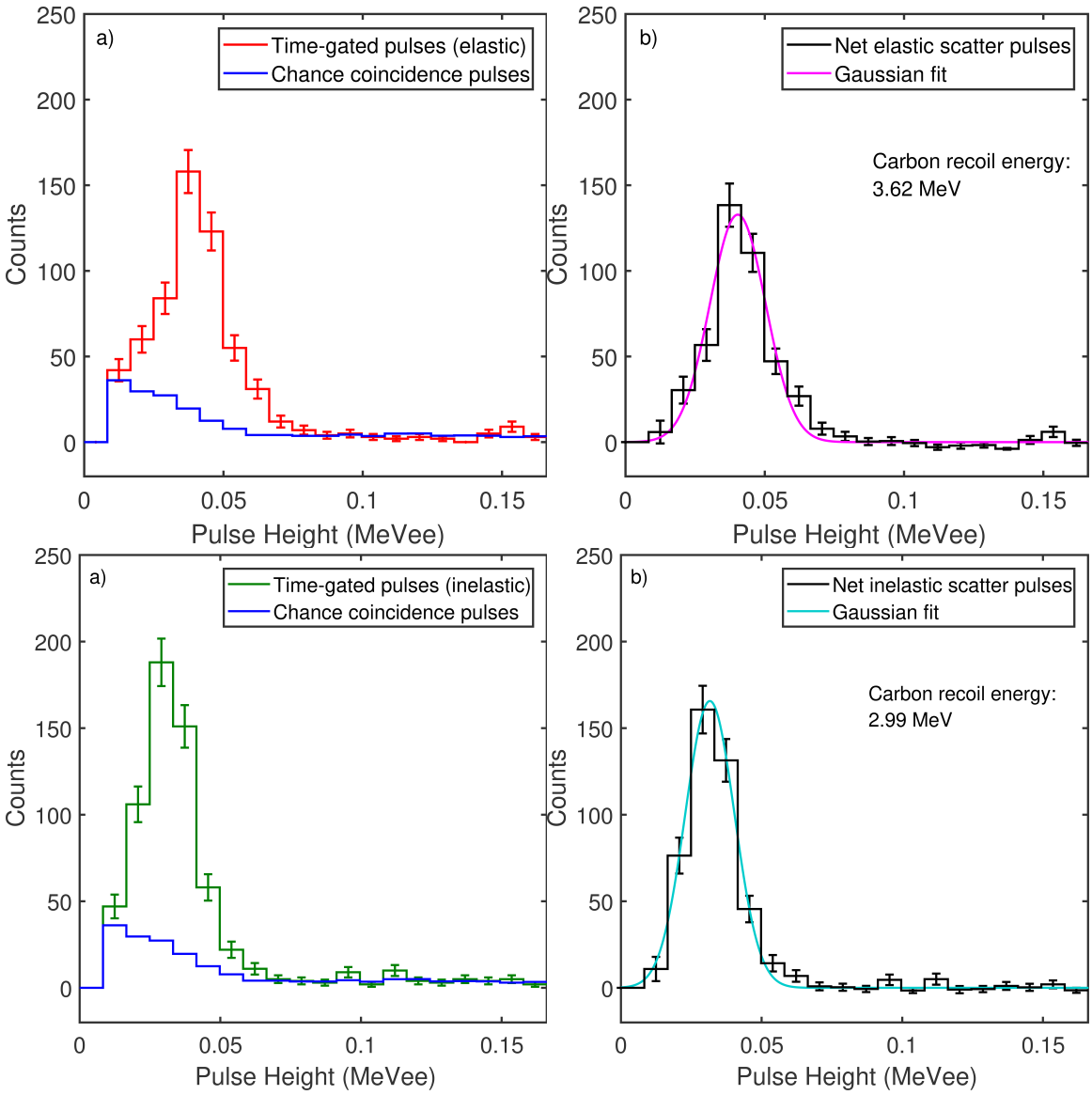

Figure 4-10 (a) The PHDs of time-gated elastic scatter pulses and chance coincidence pulses (adjusted by the ratio of the gate widths) in the 140-degree scatter detector. (b) The net PHD after subtraction of the chance coincidence background from the time-gated elastic scatter pulses, and the Gaussian fit to the result. (c) The PHDs of time-gated inelastic scatter pulses and chance coincidence pulses (adjusted by the ratio of the gate widths) in the 140-degree scatter detector. (d) The net PHD after subtraction of the chance coincidence background from the time-gated inelastic scatter pulses, and the Gaussian fit to the result.

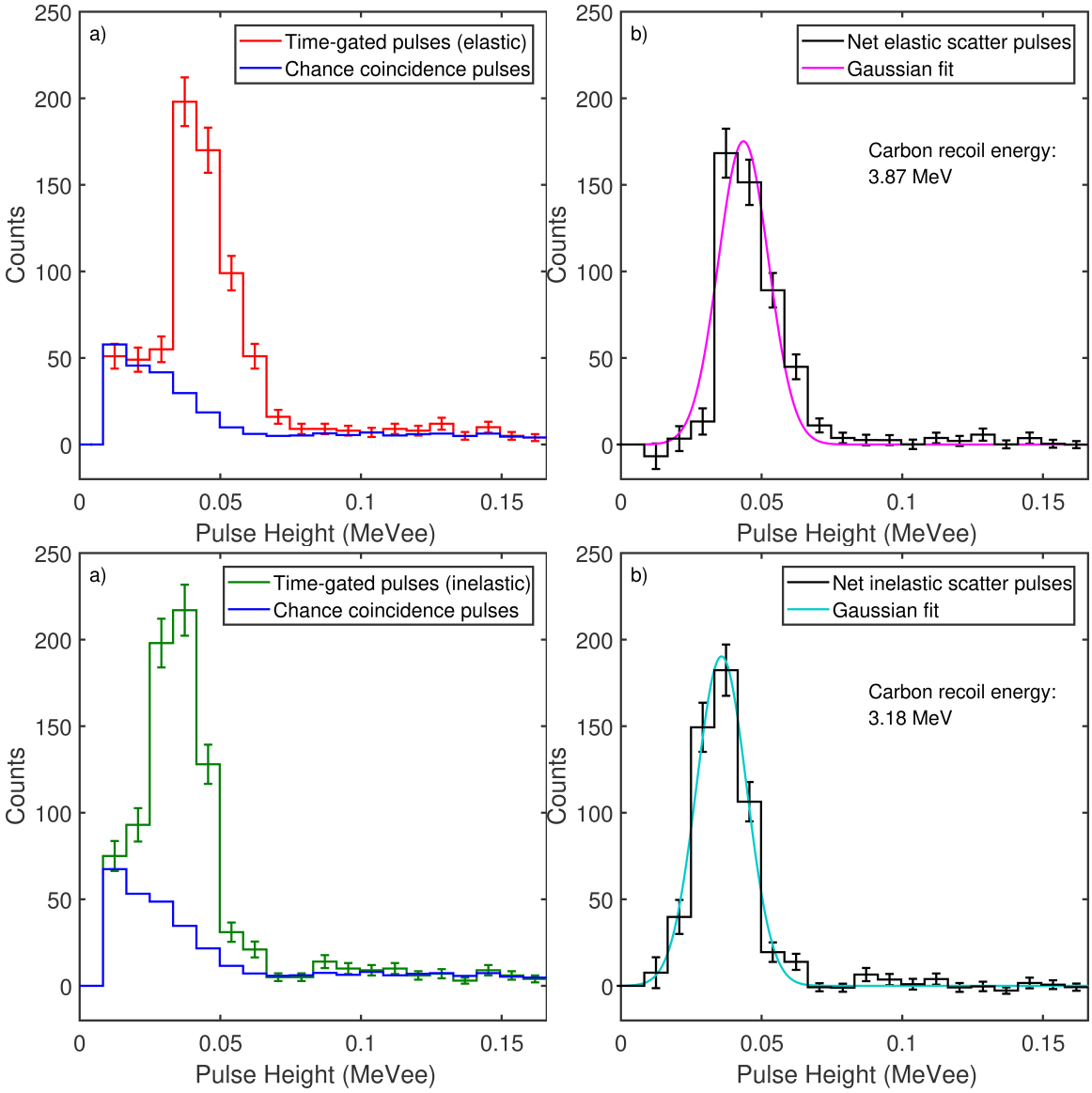

Figure 4-11 (a) The PHDs of time-gated elastic scatter pulses and chance coincidence pulses (adjusted by the ratio of the gate widths) in the 155-degree scatter detector. (b) The net PHD after subtraction of the chance coincidence background from the time-gated elastic scatter pulses, and the Gaussian fit to the result. (c) The PHDs of time-gated inelastic scatter pulses and chance coincidence pulses (adjusted by the ratio of the gate widths) in the 155-degree scatter detector. (d) The net PHD after subtraction of the chance coincidence background from the time-gated inelastic scatter pulses, and the Gaussian fit to the result.

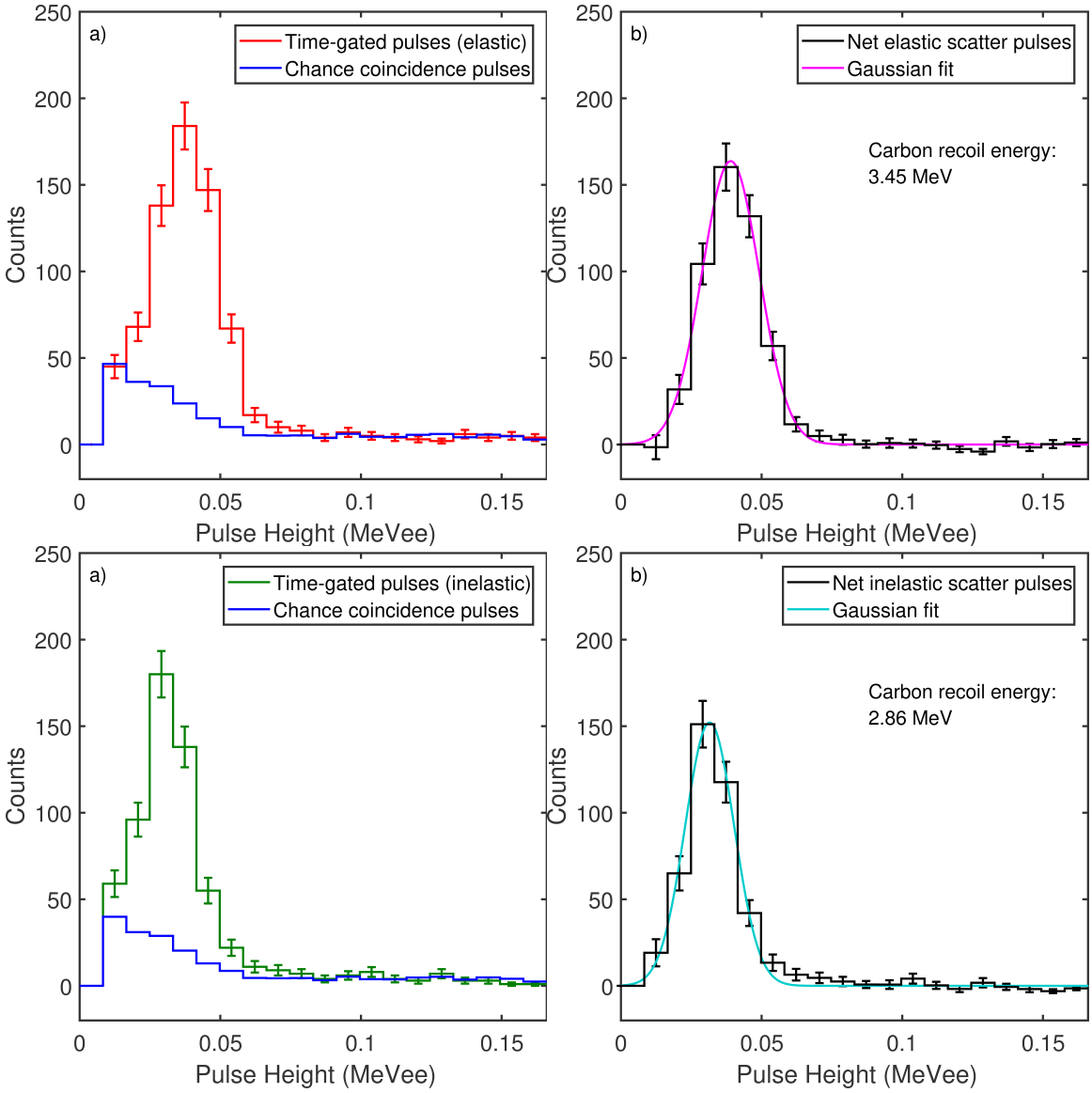

Figure 4-12 (a) The PHDs of time-gated elastic scatter pulses and chance coincidence pulses (adjusted by the ratio of the gate widths) in the 132-degree scatter detector. (b) The net PHD after subtraction of the chance coincidence background from the time-gated elastic scatter pulses, and the Gaussian fit to the result. (c) The PHDs of time-gated inelastic scatter pulses and chance coincidence pulses (adjusted by the ratio of the gate widths) in the 132-degree scatter detector. (d) The net PHD after subtraction of the chance coincidence background from the time-gated inelastic scatter pulses, and the Gaussian fit to the result.

The data were analyzed for all four angles and for both elastic and inelastic scatter on carbon. The fitted peak pulse heights versus the carbon recoil energy are shown in Fig. 4-13. Table 4-1 shows the relevant numerical values used to generate Fig. 4-13. The fit

on Fig. 4-13 was generated after weighting the data points by the inverse of the carbon recoil energy variance, $1/\sigma_{ER}^2$. The linear fit equation was $L(E) = 0.0138E - 0.0084$. Use of a linear fit for carbon recoil light output is adequate for many purposes. The carbon stopping power is sufficiently high that nonlinear equations such as Birks' Law [24] tend to saturate. However, it has been shown that at very low recoil energies an enhancement in light output is observed, and modifications to Birks' Law have been proposed [19] to address this issue. If extrapolation to lower or higher energies is required with high accuracy, a nonlinear semiempirical fit is recommended.

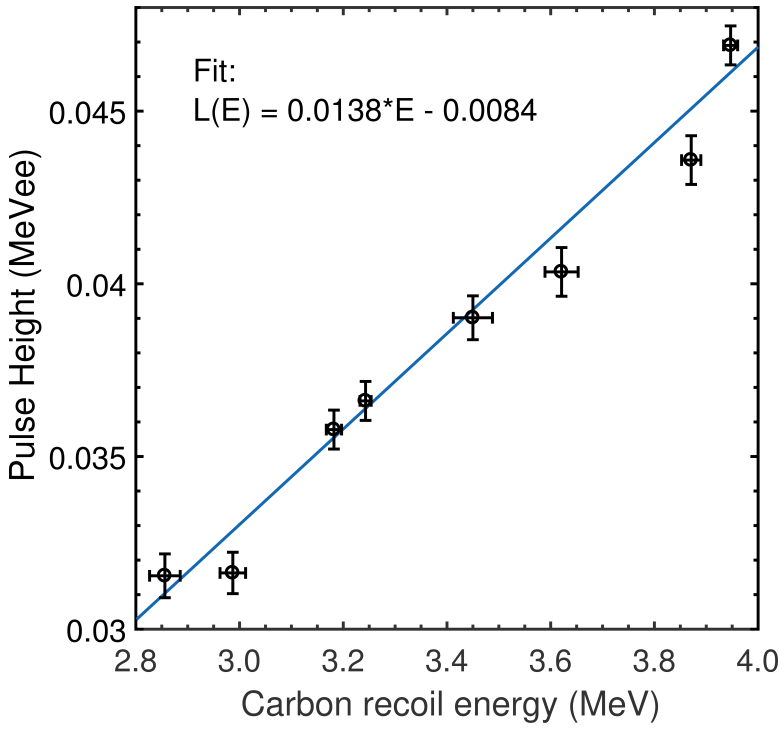

Figure 4-13 Scintillation light output as a function of recoil carbon energy.

Table 4-1. All results

Angle and scatter type	*132 inelastic*	*140 inelastic*	*155 inelastic*	*162 inelastic*	*132 elastic*	*140 elastic*	*155 elastic*	*162 elastic*
C recoil energy, E_R (MeV)	*2.856*	*2.987*	*3.182*	*3.243*	*3.450*	*3.621*	*3.871*	*3.947*
C recoil	*0.0295*	*0.0247*	*0.0147*	*0.0107*	*0.0378*	*0.0319*	*0.0186*	*0.0136*

energy standard deviation, σ_{ER} (MeV)								
Mean pulse height (MeVee)	*0.0315*	*0.0316*	*0.0358*	*0.0366*	*0.0390*	*0.0403*	*0.0436*	*0.0469*
Bootstrapped mean standard deviation (MeVee)	*0.0006*	*0.0006*	*0.0006*	*0.0006*	*0.0006*	*0.0007*	*0.0007*	*0.0006*
Light Resolution ($\Delta L/L$)	*0.651*	*0.652*	*0.586*	*0.616*	*0.615*	*0.586*	*0.482*	*0.502*

4.5.3 Uncertainty Analysis and MCNPX-PoliMi Simulation

The error bars in Figs. 4-9 through 4-12 on the PHDs correspond to one standard deviation based on counting statistics. To determine the uncertainty in the fitted mean value, we implemented a bootstrapping algorithm. The array of triple coincidences was resampled, with replacement, 150,000 times. On each iteration, the same analysis as demonstrated in Figs. 4-8 through 4-12 was performed to calculate the net PHD and fit the peak with a Gaussian. The standard deviation of the distribution of bootstrapped means is shown as the vertical error bars in Fig. 4-13.

The carbon recoil energy was originally determined using Eqs. 4-1 and 4-2, where the scatter angle was calculated from the D-T generator location to the centers of the scatter and stop detectors. It was necessary to estimate the uncertainty on this carbon recoil energy. The main contributor to this uncertainty is the experimental geometry, specifically the size of the detectors. The minimum and maximum possible scatter angles were determined for each detector pair, and the corresponding minimum and maximum carbon recoil energy were calculated. The variance can then be calculated if this range is

taken as a uniform distribution. However, uncertainty calculated in this manner is overly conservative, because the different scattering angles are not equally probable.

Instead, an MCNPX-PoliMi [33] model of the experiment was generated to simulate the scatter reactions and determine the most probable recoil energy and the distribution of recoil energies. Using MCNPX allows the geometry and cross-section considerations to be accurately taken into account.

The MPPost postprocessing tool [34] was used to extract the simulated coincident events in the scatter and stop detectors. Fig. 4-14 shows the experimental and simulated time-of-flight distributions. The 162° peaks using the JENDL 4.0u evaluated data library [65] were used to normalize the simulated count rate, yielding an estimated overall neutron source strength of 3.40×10^6 neutrons per second, which is consistent with the expected strength. A constant chance background was added, as measured for each channel. The simulated time resolution was 2.7 ns, experimentally determined with a ^{22}Na coincidence measurement.

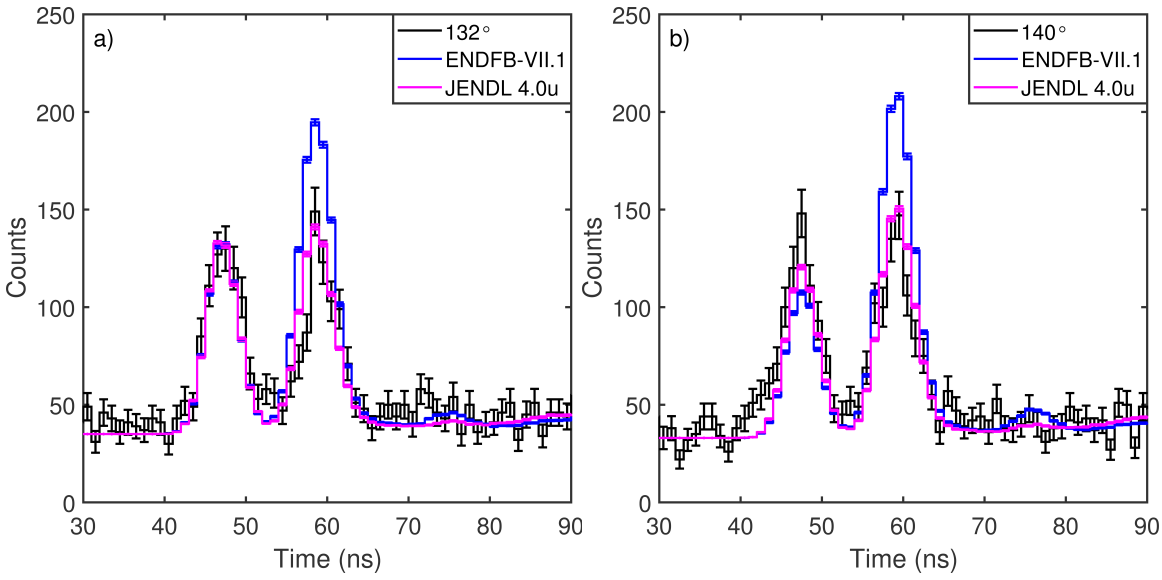

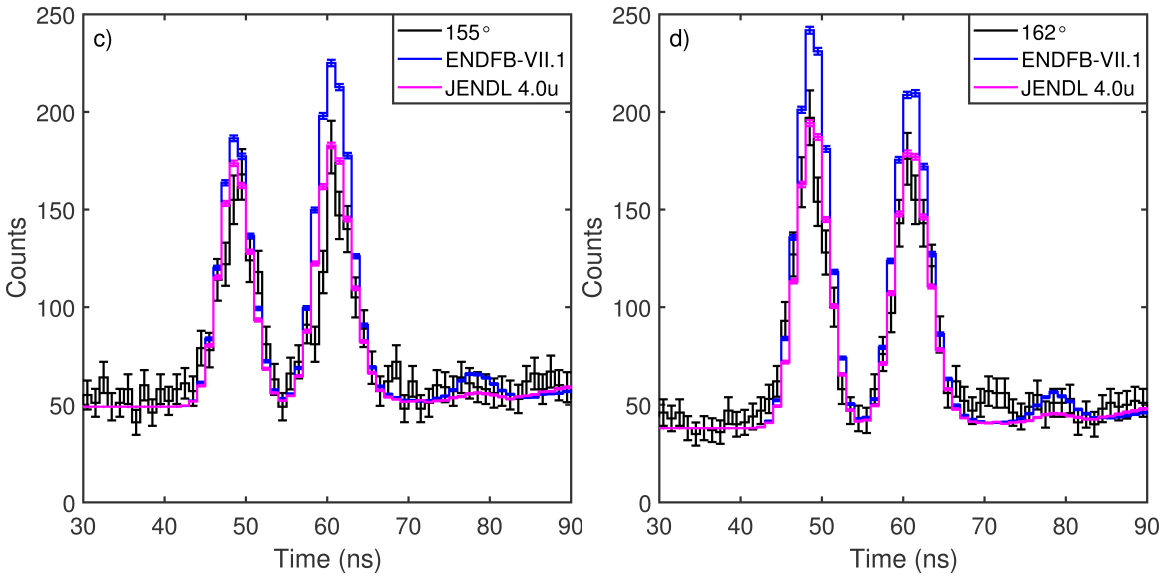

Figure 4-14 Experimental and MCNPX-PoliMi simulated time-of-flight distribution between the scatter detector and the stop detector at (a) 132°, (b) 140°, (c) 155°, and (d) 162°. The simulations were conducted using both the ENDF/B-VII.1 and JENDL-4.0u natural carbon neutron cross sections. The simulations are normalized to a calculated source strength of 3.40×10^6 neutrons per second.

The simulations illustrated an issue with the ENDF/B-VII.1 [38] natural carbon differential cross sections, with the simulated counts showing varying degrees of disagreement with the experiment. In particular, the 140° case showed a major discrepancy. Börker, Mannhart, and Siebert [67] measured the elastic and inelastic scattering differential cross sections of carbon at 14 MeV and identified similar discrepancies with ENDF, also showing the greatest discrepancies at ~140°. The JENDL-4.0u [65] cross sections are based on the data of Haouat and colleagues [68], which are comparable to the Börker data; an ACE-formatted version of JENDL is available from the Nuclear Data Center at the Korea Atomic Energy Research Institute [69]. The use of the JENDL natural carbon cross section resulted in excellent agreement for seven out of eight peaks, as seen in Fig. 4-14; the simulated elastic peak at 140° remains low compared to the experiment.

The good agreement between the simulated and experimental time-of-flight distributions indicates that the particle transport within the experiment is well understood and the geometry is accurately modeled. Figure 4-15 shows the simulated energy distributions of carbon recoils in the scatter detector, corresponding to elastic and inelastic scatter for all four detector angles using the same time-gate widths that were applied to the experimental results. Each distribution was fitted with a Gaussian, and the mean and standard deviation values are reported in Table 4-1 and Fig. 4-13. The widths of the distributions increase at shallower angles, consistent with detector orientation effects and the increasing slope of the E(θ) curves in Fig. 4-3.

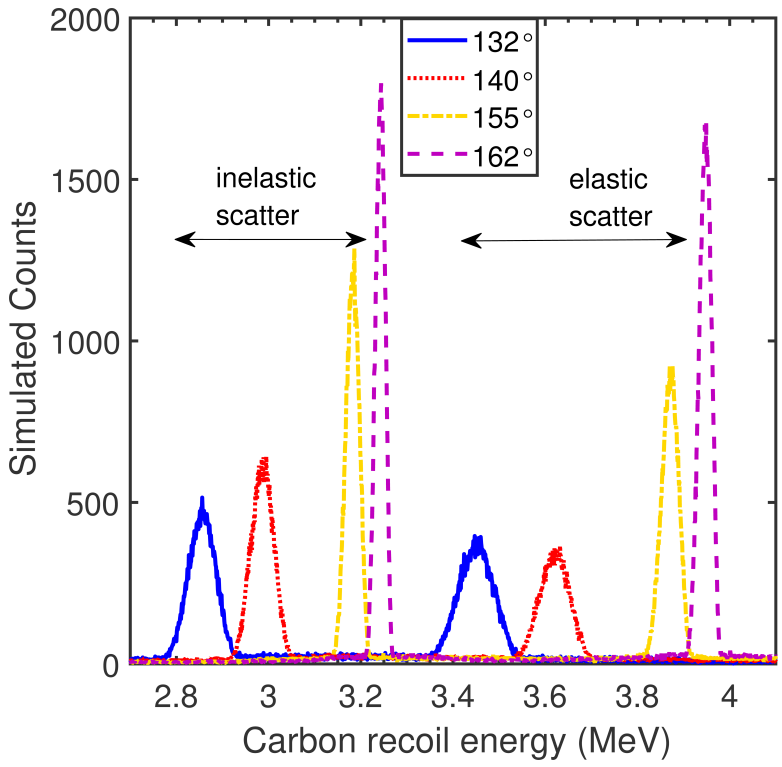

Figure 4-15 MCNPX-PoliMi simulated distributions of carbon recoil energies in the scatter detector, corresponding to the time-gated coincidences with the stop detectors. The shallower scattering angles result in broader distributions of recoil energy, as expected due to the cosine dependence of the kinematics.

Additional systematic uncertainties that were not accounted for in the analysis are the variation in the initial neutron energy (14.1 MeV was used in all cases) and the measurement errors in the geometry. The latter was judged to be negligible because of the agreement shown in Fig. 4-14. The DROSG2000 code [70] was used to calculate the D-T reaction kinematics and estimate the neutron energy bounds as 14.08 ± 0.05 MeV. The neutron energy spread could contribute up to an additional 0.5% uncertainty on the carbon recoil energies.

4.6 Summary and Conclusions

The data presented in this paper comprise the first measurement of carbon recoil light output in EJ-309; we found the ratio of the pulse heights in million electron volts electron-equivalent and the carbon recoil energy in million electron volts to be 0.0114 ± 0.0003 in the energy range from 2.84 to 3.92 MeV. Using a monoenergetic neutron source along with multiple detectors at fixed angles enabled convenient isolation of specific carbon recoil energies. This approach included trigger logic using triple-coincidences and with time-of-flight, pulse height, and pulse shape discrimination gates, which reduced the number of chance coincidences. A bootstrapping technique was used to estimate the statistical error on the measured light output response.

MCNPX simulation of the experiment allowed accurate determination of the energy distribution of carbon recoils in the scatter detector for each stop detector, accounting for detector size and interaction cross sections. The mean carbon recoil energy values determined in this manner agreed within 1% with those determined by analytic calculation, assuming the center of each detector as the interaction locations. However, analytic calculation of the spread in the energy distributions by calculating

minimum and maximum possible angles (i.e., using the corners of the detectors as the bounds of a uniform distribution) overestimated the spread in energy by as much as 90%.

The simulated and measured time-of-flight distributions agreed excellently using the JENDL-4.0u library; consequently, we conclude that the JENDL-4.0u neutron differential cross sections for natural carbon are more accurate than those of ENDF/B-VII.1. This finding may be of particular interest to users of 14 MeV neutrons, such as the fusion community and those researching D-T active interrogation.

The triple-coincidence method demonstrated in this work can be applied to characterize any organic scintillator detector, for any interaction with a direct relationship between neutron scatter angle and recoil energy. If forward-scattering angles are used, proton light output can be measured. Two particularly promising potential applications are characterization of deuterated detectors at backscatter angles to isolate the deuteron response, and full characterization of the anisotropic light output of stilbene [20,71], for example by rotating the scatter detector.

4.7 Additional Acknowledgment

Oak Ridge National Laboratory is managed by UT-Battelle LLC for the US Department of Energy under contract DE-AC05-00OR22725.

Chapter 5 Detector Resolution

5.1 Previous Resolution Functions

Enqvist et al [31] presented fitted detector resolution functions for the 3 in. x 3 in. (referred to as 3x3) and 5 in. x 5 in. (referred to as 5x5) EJ-309 detectors. The data used to generate these fits are the same as discussed in Chapter 4. Recall that neutrons from the time-of-flight experiment conducted at Ohio University's Edwards Accelerator Facility were binned into 100-keV width bins. Then, following Kornilov [43], the binned PHDs were smoothed, differentiated, and a Gaussian was fitted to the rightmost peak of the derivative. In addition to taking the mean of the Gaussian as the pulse height corresponding to a single full-energy scatter on hydrogen, the full-width at half-maximum (FWHM) of the Gaussian was determined. The resolution was defined as the FWHM divided by the pulse height, and fitted to the relationship and coefficients identified in Chapter 2, and reproduced here for convenience.

Table 5-1 presents the resolution coefficients for the detector energy resolution for 3x3 and 5x5 EJ-309 detectors, determined in [31]. The resolution function is of the form,

$$\frac{\Delta L}{L} = \sqrt{\alpha^2 + \frac{\beta^2}{L} + \left(\frac{\gamma}{L}\right)^2}, \tag{5-1}$$

where ΔL is the full-width at half-maximum (FWHM) and L is the light in MeVee. However, in MPPost, the implementation is of a different form, adapted from [37] where L is now in keVee:

$$\frac{\Delta L}{L} = \frac{AL+B\sqrt{L}+C}{100L}, \tag{5-2}$$

with coefficients presented in Table 5-1.

Table 5-1. Previous resolution coefficients.

Detector Size	α	β	γ		A	B	C
3x3	*0.113*	*0.065*	*0.060*		*9.8532*	*0*	*4738.6643*
5x5	*0.102*	*0.102*	*0.035*		*10.6092*	*11.2033*	*3923.0106*

5.2 Overestimated Resolution at Low Pulse Height

The method used to determine both the light output and resolution data points in [31] relies on the existence of a "rightmost" Gaussian corresponding to single scatters on hydrogen. There is a second Gaussian present in the derivative of the PHDs that corresponds to multiple-scatters (C-H and/or H-H). At high neutron energies and high corresponding light output, these Gaussians are well-separated and readily distinguishable.

However, when considering PHDs corresponding to lower incident neutron energies, two factors cause the Gaussians to begin to overlap and ultimately merge: nonlinear light output, and worsening detector resolution. The slope of the proton light output curve is less steep as neutron energy (in MeV) decreases, causing smaller separation of the mean values of the Gaussians (in MeVee). At the same time, the

detector resolution is worsening, increasing the width of the Gaussians. At some point the algorithm is no longer fitting the rightmost Gaussian but a superposition of the two, causing two effects: an underestimate of the single-scatter light output, and an overestimate of the resolution.

5.3 New Resolution Function

The experiment at ORNL to measure carbon light output also resulted in eight resolution data points. The FWHMs of the peaks shown in Figs 4-9 – 4-12 were divided by the mean values of the peaks; the values are presented in Table 4-1. It should be noted that these values are upper bounds; there is a peak-broadening component that is due to the energy spread induced by the experimental geometry. This additional spread is small and no attempt was made to deconvolve it.

In order to generate a new estimated resolution curve, the fits from Table 5-1 were used to generate dummy data points corresponding to the interval of 1 to 2 MeVee with 0.1 MeVee spacing. These data points and the carbon data points were used to generate new fit coefficients for Eq 5-2.

Fig 5-1 shows the two previous fits, the dummy data points, the carbon data points, and the two new fits. The new resolution coefficients are presented in Table 5-2.

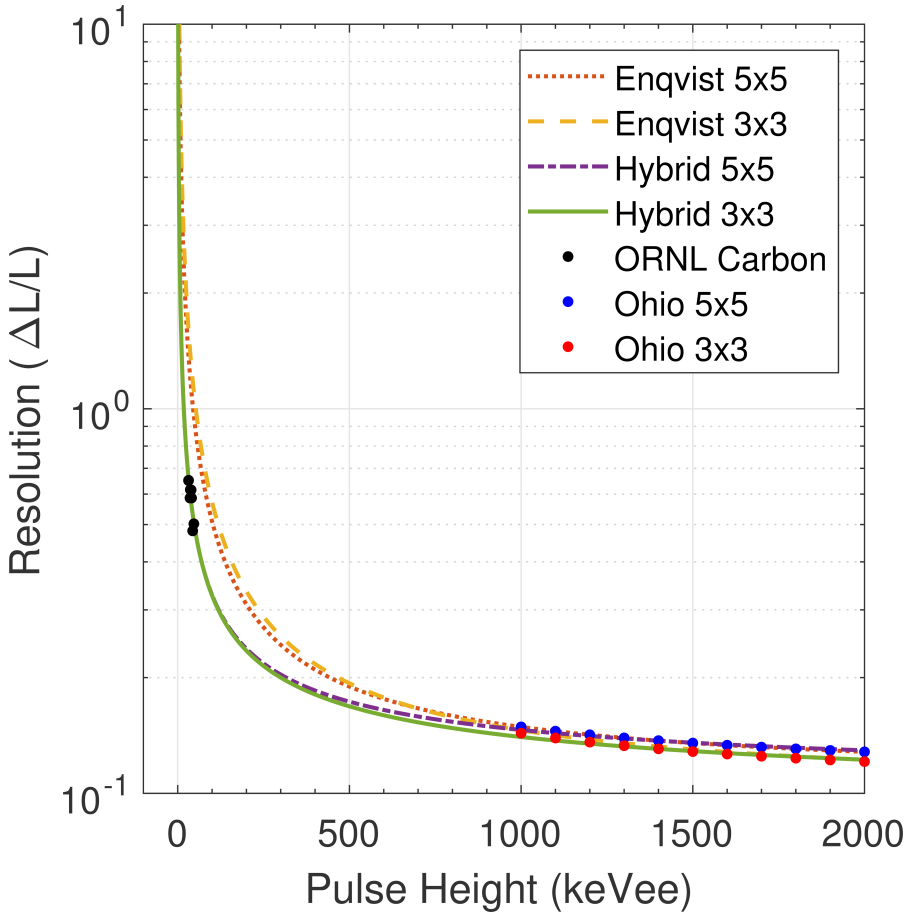

Figure 5-1. Previous (Enqvist) and new (hybrid) detector resolution fits for EJ-309. The black data points are taken from the carbon light output data of Chapter 5, while the red and blue data points are generated using the published fits of [31].

Table 5-2. New resolution coefficients.

Detector Size	*A*	*B*	*C*
3x3	*8.674*	*135.9*	*1043*
5x5	*9.639*	*123.2*	*1084*

5.4 Discussion

Several caveats should be mentioned in this estimate: the carbon light output data points are from the 3x3 detector size, with the gain set such that the Cs-137 Compton edge corresponds to 0.575 V. The dummy data correspond to either the 3x3 or 5x5 detector sizes, calibrated to approximately 0.3V. (The calibration issue with the 3x3 data from the Ohio experiment, discussed in Chapter 3, was corrected here as well). The

combination of different detector sizes and gain settings introduces some uncertainty into the resolution functions; however, these new estimates are substantial improvements over the previous fits, which will be demonstrated in the next Chapter.

Chapter 6 Application of Improvements: Proton Therapy

6.1 Introduction to Chapter

In Chapters 3 through 5, I presented improvements to proton light output models, carbon light output data, as well as a new detector resolution function for EJ-309 organic scintillator detectors. The aim of this chapter is to demonstrate the improvements in the agreement between simulation and measurement that can be obtained by employing these new relationships. The chapter expands on selected elements of a draft journal article titled, "Organic Scintillator Detector Response to Neutrons Produced During Proton Therapy: Comparison of Experimental and MCNPX-PoliMi Simulated Results," authored by M. A. Norsworthy[1], S. D. Clarke[1], C. A. Green[1], S. A. Pozzi[1], M. Pankuch[2], R. W. Schulte.[3]

6.2 Introduction

Proton beam therapy is becoming increasingly common in the United States and worldwide and is considered a preferred modality for cancers in which the sparing of normal tissues is particularly important. The primary advantage of proton beam therapy is the effective dose localization, compared to photon-based radiation therapies, with no primary dose delivered beyond the Bragg peak. While the protons deposit dose very effectively, the interaction of protons with beamline materials, or the patients themselves, produces secondary neutrons, charged particles, and photons that can propagate dose outside of the planned treatment volume [72]. Neutrons are of particular concern due to

their higher biological effectiveness, compared to photons, which may lead to higher risk of secondary tumors later in life.

Historically, neutron dose has not been monitored during proton therapy and not been taken into account during treatment planning; however, this additional dose should be minimized, especially in patients at higher risk for secondary tumors such as children [73],[74]. Traditional neutron dose instruments, such as rem-meters, rely on neutron moderation with pre-calibrated response functions [75]. This approach can be unreliable if the source neutron energy spectrum is different from the calibration spectrum, which could be the case in proton therapy applications.

Previously, we have demonstrated an approach using organic scintillators to measure the secondary neutron production from biological phantoms irradiated with therapeutic-energy proton beams [17,52,76]. Here, we extended this work to an absolute comparison with Monte Carlo simulations: experiments that were performed at the Northwestern Medicine Chicago Proton Center (CPC) were compared to simulations performed with the MCNPX-PoliMi code [33,63] and processed with the MPPost post-processing code [34].

6.3 Methods and Materials

6.3.1 Description of the Experiment

Experimental measurements of neutron doses were conducted in the horizontal beam patient treatment room 2 at the CPC using a soft tissue phantom. The phantom was manufactured by CIRS, Inc; the isotopic composition and density is listed in Table 6-1. It should be noted that the fractions of carbon and oxygen in the phantom are approximately

reversed compared to real tissue (~65% oxygen, ~20% carbon [77]). This may affect the proton-induced neutron spectrum; this is discussed further in the Section 6.6.

Table 6-1. Isotopic composition (in weight percent) and density of the soft tissue phantom manufactured by CIRS, Inc. used in the experiment.

	Soft Tissue 1.055 g/cm³
Hydrogen	*8.47*
Carbon	*57.44*
Nitrogen	*1.65*
Oxygen	*24.59*
Magnesium	*7.62*
Chlorine	*0.19*

The phantom dimensions were 30 cm by 30 cm by 14 cm. An overhead view of the detector placement is shown in Fig. 6-1. Spot beams of 155- and 200-MeV protons were used to irradiate the phantom, consistent with a previous experiment at Loma Linda University Medical Center (LLUMC) [17]. The proton energy was defined as the exit energy leaving the distal nozzle. The proton spot was held static in position targeted to the isocenter. All nozzle components including scatterers, range shifters, and apertures were removed of the beam path. The only beamline device in the path of the proton beam was the transmission monitor chamber of ~7 mm of water-equivalent thickness. The beam spots in air, measured at isocenter were near Gaussian in profile with approximately 3 cm FWHM.

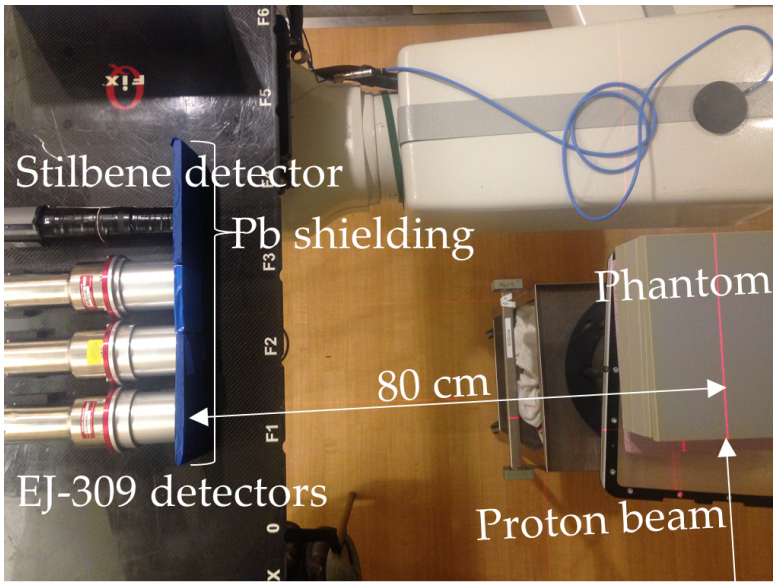

Figure 6-1. Photograph of the experimental setup, with the soft tissue phantom in place, viewed from the top.

Three 7.62 cm diameter by 7.62 cm thick EJ-309 liquid detectors and one 5.08 cm diameter by 7.62 cm thick crystalline stilbene organic scintillator detector were placed orthogonal to the phantom, 80 cm from isocenter, perpendicular to the incident beam direction, consistent with a previous experiment at LLUMC [17]. A 12-mm lead shield was placed in front of the detectors to reduce photon count rates. The voltage signals from the photomultiplier tubes were digitized using a CAEN DT5720 250-MHz 12-bit desktop digitizer connected using a fiberoptic cable to the data acquisition PC in the control room.

The proton beam fluences used in this experiment were approximately 1000 times below clinical intensity to avoid saturation of the digital data acquisition system. Because the usual beamline ion chamber monitors are not routinely calibrated for low beam fluences, an additional ionization chamber was placed directly in front of the phantom. Cross-calibrations were performed to ensure accurate estimates of the proton fluence and

flux incident on the phantom. These fluence estimates are critical for absolute validation of neutron counts and dose rates.

6.3.2 MCNPX-PoliMi Model of the Experiment

The proton beam was simulated as a 3-cm diameter, uniform cylindrical beam. The phantom was modeled using the compositions described in Table 6-1. Details of the rest of the room and equipment were omitted in the simulation model for simplicity and to protect proprietary information. Figure 6-2 shows the model geometry overlaid on the top-down photo.

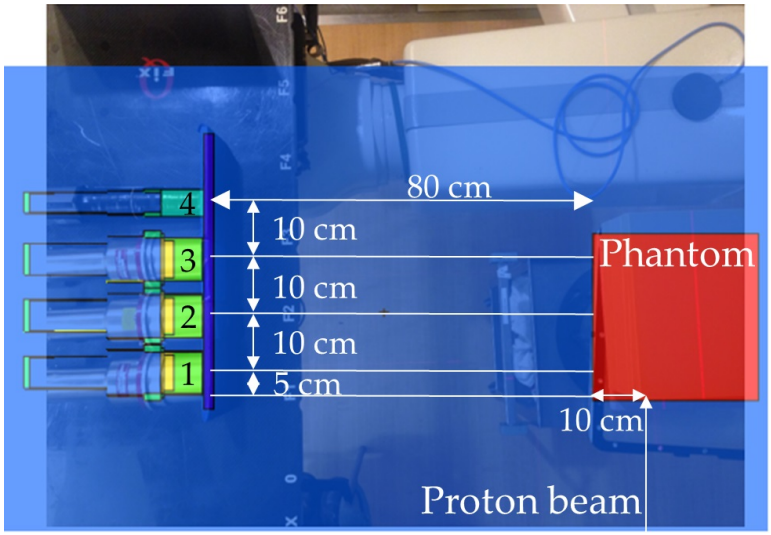

Figure 6-2. Top down photograph of the experimental setup with MCNPX-PoliMi geometry overlaid. The phantom is shown in red, and the detectors are numbered 1-4 in order of increasing depth with respect to the front face of the phantom. Relevant dimensions are shown.

MCNPX-PoliMi enables accurate simulations of organic scintillator detector response. The code and the MPPost post-processing tools have been extensively tested and used for applications in nuclear nonproliferation and safeguards, nuclear physics, and

medical physics [32–34]. The MCNPX-PoliMi code generates a data file of all neutron and photon events in specified cells. Using accurate calibration and light output, one can generate a histogram of pulse heights, referred to as a "PHD," or PHD. These PHDs can then be validated against the experimental PHDs.

6.4 Results and Discussion

The primary purpose of this chapter in this dissertation is to highlight the effects of adopting the new relationships derived for proton light output, carbon light output, and detector resolution developed in Chapters 3, 4, and 5. Proton therapy is not a typical use case for our detectors, the neutron spectrum is quite different from a fission neutron spectrum, and the modeling is complex. In short, demonstrating improvements in modeling this exotic case will build confidence in the relationships developed above.

6.4.1 Effects of Different Models

Figure 6-3 shows the absolute-scale neutron PHDs from the experiment and the simulation of neutron production in soft tissue using the 200 MeV proton beam. Results for only Detector 3 is shown for clarity. The results are shown in units of neutron counts per incident proton, as a function of light output in the detector. The post-processing settings used are the original settings from Tables 2-3 and 2-4.

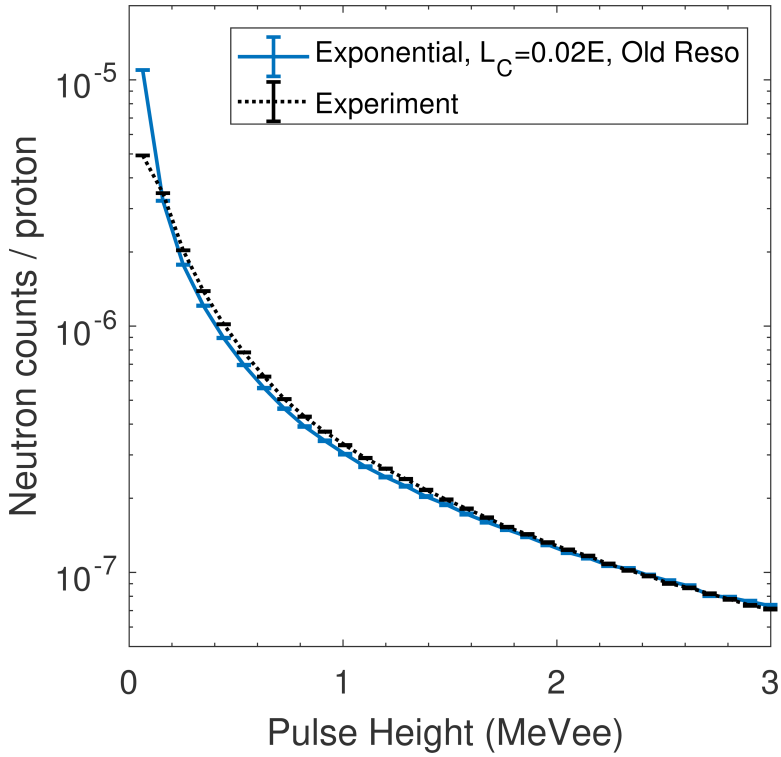

Figure 6-3 Simulated and measured PHDs in the Detector 3 due to 200-MeV protons incident on the soft tissue phantom. Statistical error bars are shown. Post-processing settings employed do not incorporate the changes suggested in this dissertation.

In Fig 6-3, the simulated PHD exhibits substantial discrepancies from the experiment. The log-scale can sometimes hide the amount of disagreement, as well as make trend analysis difficult, so we again present the data as a fractional difference plot in Fig 6-4.

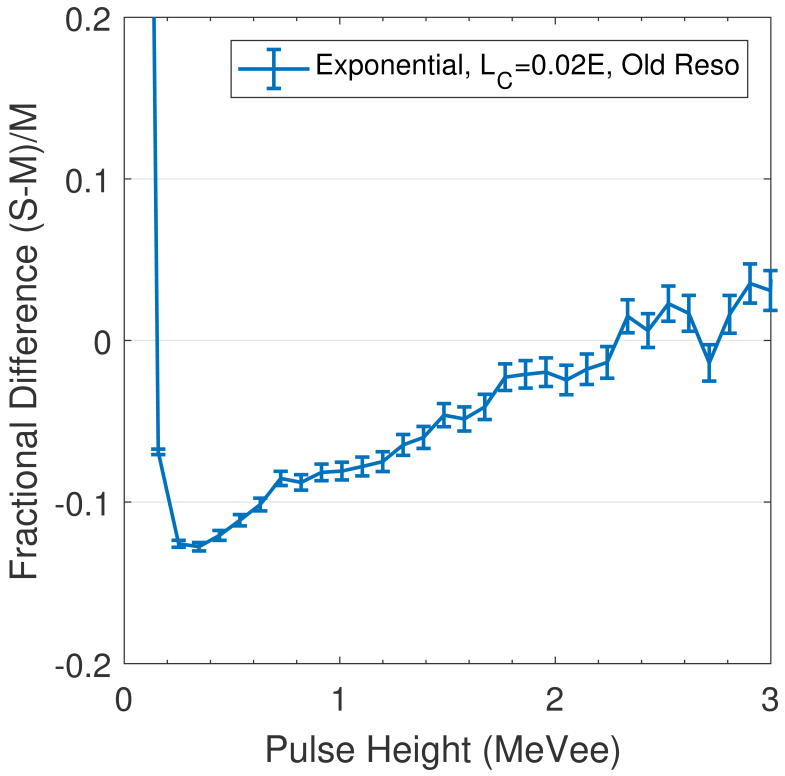

Figure 6-4. Fractional difference plot of data presented in Fig. 6-3.

Figure 6-4 shows a similar error trend to that shown in Fig 3-8 as Exponential1, using the same post-processing settings. (Figure 3-8 showed the fractional difference plot of the ^{252}Cf neutron measurement and simulation.)

Now, we examine the improvements that arise from making three changes in sequence. First, we show the change from Exponential1 to Birks. Then, we apply the new carbon light output relationship of L_C=0.01139E. Finally, we apply the new resolution coefficients from Chapter 5. The fractional difference plot for each case is shown on Fig 6-5. Figure 6-6 shows the same curves as Fig 6-5, but zoomed in.

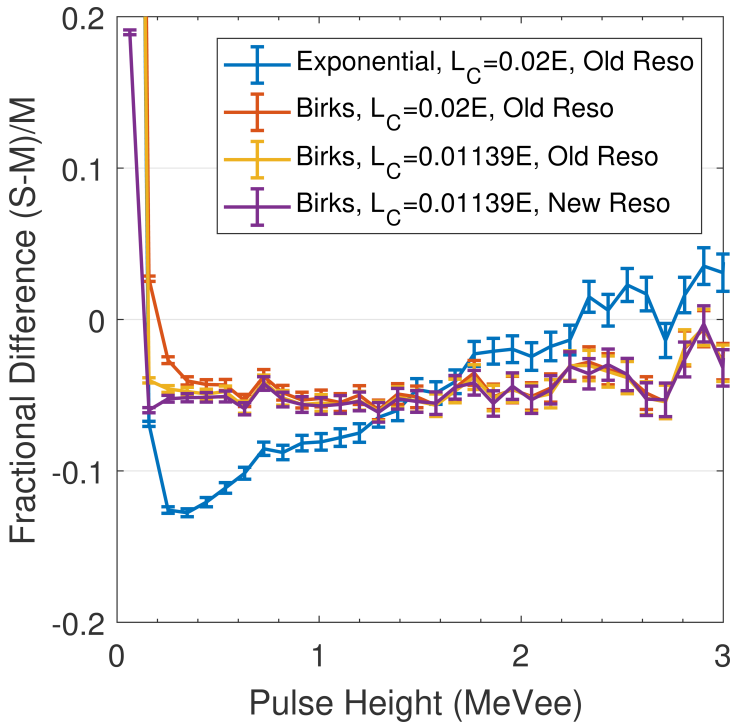

Figure 6-5 Fractional difference plots of simulated PHDs using various processing settings compared to experiment.

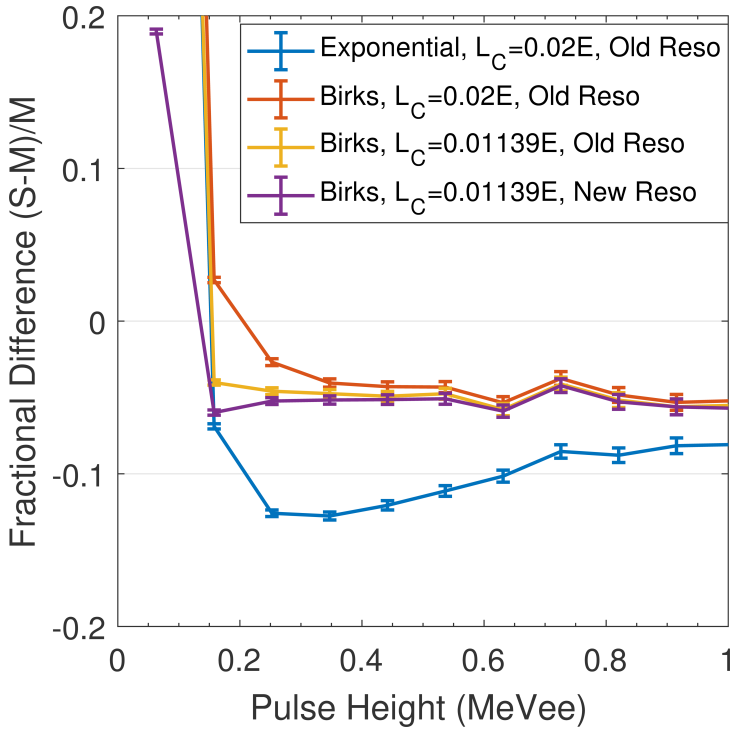

Figure 6-6. Fractional difference plots of simulated PHDs using various processing settings compared to experiment, zoomed in for better legibility in the small pulse height regime.

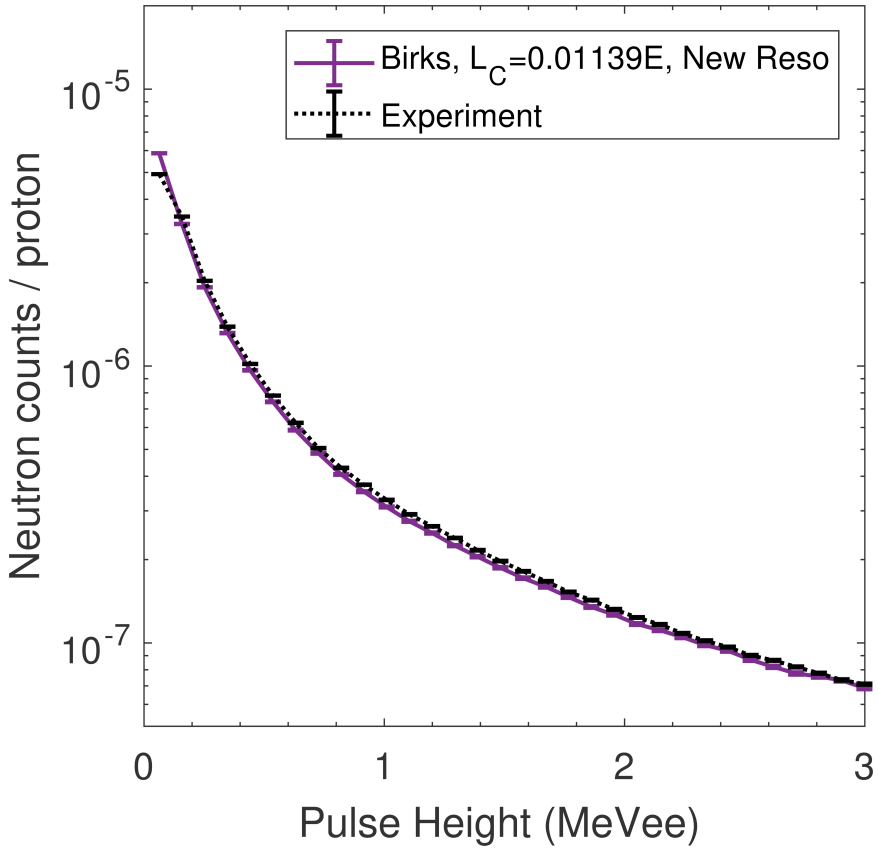

Figure 6-7. Simulated and measured PHDs in Detector 3 due to 200-MeV protons incident on the soft tissue phantom. Statistical error bars are shown. Best agreement achieved, using updated proton light, carbon light, and resolution settings.

6.5 Full Soft Tissue Phantom Results

Figures 6-8 and 6-10 show the absolute-scale neutron PHDs from the experiment and the simulation of neutron production in soft tissue by the 200 and 155 MeV proton beams. The results are shown in units of neutron counts per incident proton, as a function of light output in the detector. As expected, 200-MeV protons produced approximately 50% more neutron counts per proton than 155-MeV protons. The relative random error due to counting statistics in the bins with the fewest counts is approximately 4%; error bars are shown on the figures, but are smaller than the marker size.

Figures 6-9 and 6-11 show the fractional difference plots, enabling assessment of the quality of agreement between the simulations and measurements. Perfect agreement would be a flat line at a fractional difference of zero. Constant offsets indicate good agreement with a discrepancy in source strength or normalization. Slopes or features are generally undesirable. In all cases, the new, updated postprocessing settings result in improved agreement.

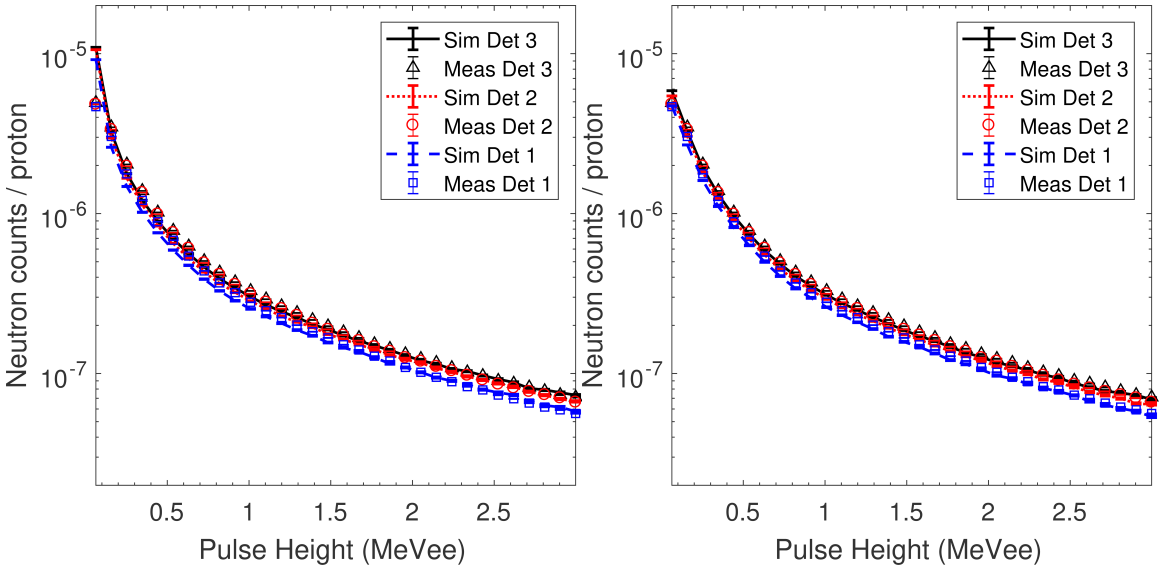

Figure 6-8 Simulated and measured PHDs in the EJ-309 detectors due to 200-MeV protons incident on the soft tissue phantom. Left: Original settings. Right: Updated settings. The measured data points are represented by open markers and the simulated distributions are represented by lines. Statistical error bars are shown, but are smaller than the marker sizes.

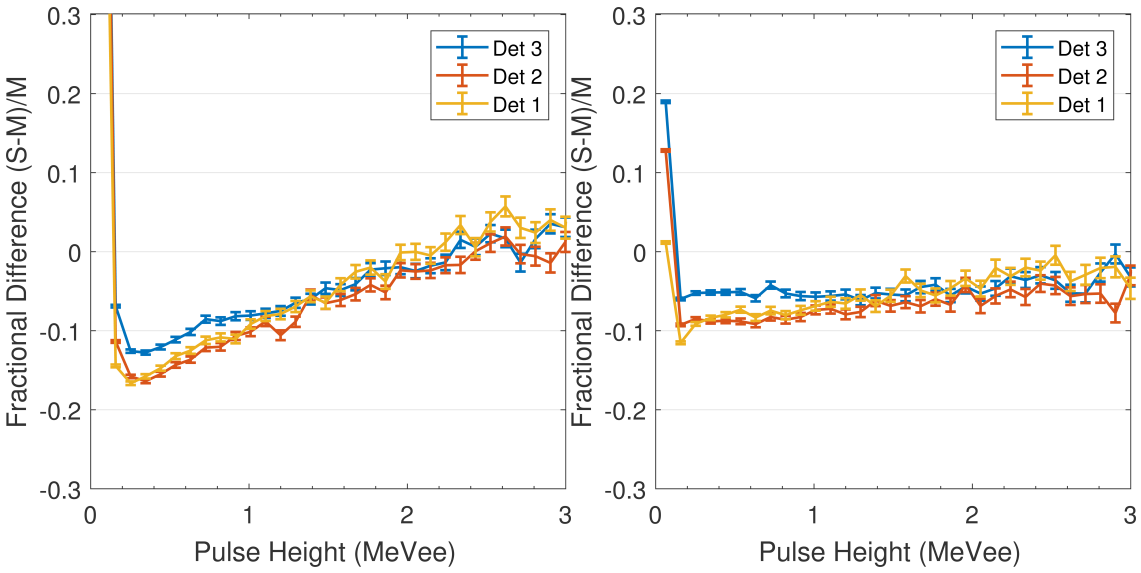

Figure 6-9 Fractional difference plots of simulated and measured PHDs in the EJ-309 detectors due to 200-MeV protons incident on the soft tissue phantom. Left: Original settings. Right: Updated settings. Statistical error bars are shown.

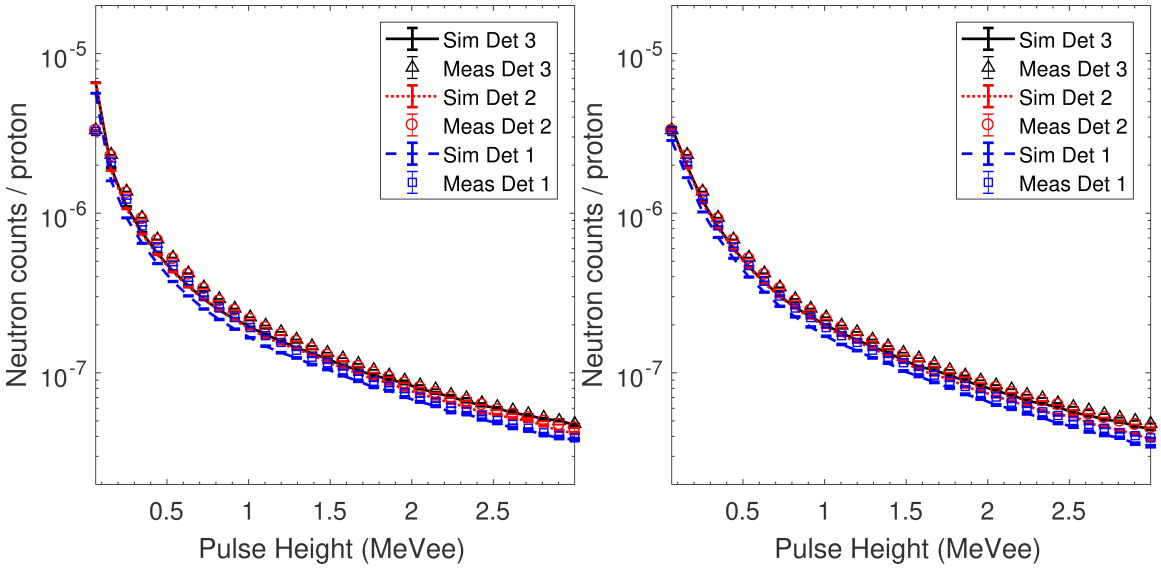

Figure 6-10 Simulated and measured PHDs in the EJ-309 detectors due to 155-MeV protons incident on the soft tissue phantom. Left: Original settings. Right: 1Updated settings. The measured data points are represented by open markers and the simulated distributions are represented by lines. Statistical error bars are shown, but are smaller than the marker sizes.

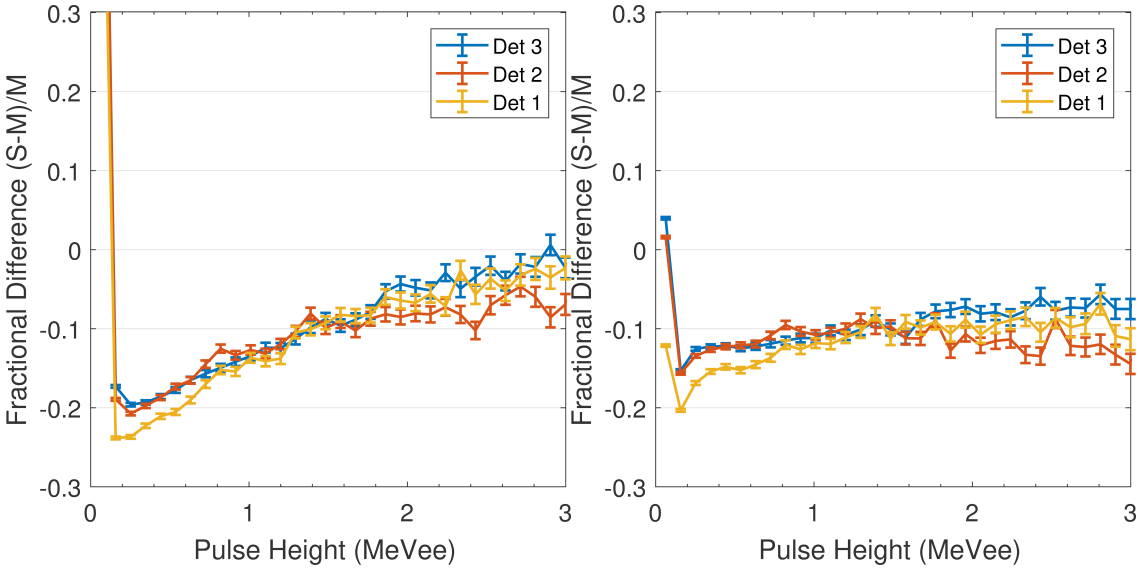

Figure 6-11 Fractional difference plots of simulated and measured PHDs in the EJ-309 detectors due to 155-MeV protons incident on the soft tissue phantom. Left: Original settings. Right: Updated settings. Statistical error bars are shown.

Table 6-2 presents the ratios of the simulated and experimental total counts over the range 0.110 MeVee to 3.045 MeVee, which corresponds to proton recoils of 0.8 to 6.7 MeV. The agreement between the simulated and experimental PHDs is of order 5-15% for the soft tissue phantom. The most probable sources of this disagreement are inaccuracies in the source strength normalization and the simplified model geometry.

Table 6-2 Comparison of simulated (ΣS) and measured (ΣM) total counts from 0.110 to 3.045 MeVee (0.8 to 6.7 MeV proton recoils) for the EJ-309 detectors.

	$\frac{\Sigma S}{\Sigma M}$			
Detector	**Soft Tissue, 200 MeV, ExpOld**	**Soft Tissue, 200 MeV, BirksNew**	**Soft Tissue, 155 MeV, ExpOld**	**Soft Tissue, 155 MeV, BirksNew**
Detector 3	0.915±0.001	0.947±0.001	0.845±0.001	0.878±0.001
Detector 2	0.883±0.001	0.917±0.001	0.837±0.001	0.872±0.001
Detector 1	0.881±0.001	0.917±0.001	0.811±0.001	0.847±0.001

The lower threshold for the measurements was 47 keVee, which corresponds to 450-keV neutrons. The upper proton recoil energy limit of the PHD does not mean that the detector is insensitive to neutrons above a that energy. In fact, neutron elastic scatters on hydrogen, which are the dominant contribution to measured light, can deposit anywhere from 0 to 100% of the neutron energy to a recoil proton. Figure 12 of Clarke and colleagues [17] shows the energy dependent neutron detection efficiency in simulation of 200 MeV protons on the soft tissue phantom – neutrons as high as 200 MeV have an intrinsic efficiency of approximately 2-3%

6.6 Summary and Conclusions

We have further validated a previously reported method [17] to measure secondary neutron production in proton therapy treatments. The current work expands upon previous work by demonstrating agreement between simulated and measured neutron PHDs on an absolute basis. Using organic scintillator detectors, we measured neutron PHDs due to secondary neutron production by 155-MeV and 200-MeV proton beams incident on a tissue-equivalent phantom. The measured PHDs were compared to simulated PHDs modeled with the MCNPX-PoliMi code.

In this chapter, we have demonstrated that the MCNPX-PoliMi code and MPPost post-processing tools can be used to simulate the neutron production and detector response in good agreement with both the shape and absolute magnitude of the measured PHDs. The neutron spectrum produced by protons incident on the phantom used in the experiment is expected to be similar to that of real tissue, but additional research would be required to evaluate the possible impact of the differing fractions of carbon and oxygen before using these specific results for dose calculations.

The results shown in this chapter demonstrate the importance of accurate light output models for experiments in atypical conditions. The neutron spectra measured at the Chicago Proton Center are quite different from a ^{252}Cf fission spectrum. The initial efforts to simulate the experiment produced poor agreement, but after application of the proton light output, carbon light output, and resolution functions presented in Chapters 3 through 5, substantially better agreement was achieved.

Chapter 7 Summary and Conclusion

7.1 Importance of Safeguards

The IAEA safeguards program is a component of the broader nuclear non-proliferation and counter-proliferation regime. To date, "no NPT non-nuclear-weapon state subject to safeguards has diverted any meaningful amount of declared nuclear material or significantly misused a safeguarded nuclear facility [1]." The relative effectiveness of the safeguards regime in detecting and deterring diversions of nuclear material is difficult to assess, but it is safe to assert that preventing the misuse of nuclear material is as important as ever. The threat of nuclear terrorism, in particular, is difficult to overstate.

With this motivation, the research presented in this dissertation had an overall objective that is simply-stated: to improve the agreement between simulated and measured EJ-309 neutron detector response. Achieving this objective would have a positive impact on ongoing research projects to develop the next generation of safeguards instrumentation, such as the Fast Neutron Multiplicity Counter, advanced portal monitors, dual-particle imaging systems, and others. Robust modeling of these systems will be required before any real-world safeguards deployment is possible. The work presented in Chapters 3 through 6 achieved the stated objective, as evidenced by the improved agreement shown in Figs. 3-5, 3-8, and 6-6 through 6-11. The improvements made pertain to proton light output, carbon light output, and detector resolution.

7.2 Summary: Contributions of the Dissertation

This dissertation presented contributions in three areas: proton light output, carbon light output, and detector resolution. Improvements in each of these areas were shown that improve the accuracy of simulated detector response.

Proton light output is the dominant detector response of organic scintillators to neutrons in the fission energy range. The key improvement made in this area was to shift from a purely empirical exponential form to the semiempirical Birks' Law form for the proton light output model. The semiempirical form extrapolates more reliably to low energy proton depositions, improving overall agreement. The choice among the several available empirical and semiempirical models for neutron light output can profoundly impact the accuracy of simulated PHDs. The best agreement between simulated and measured neutron PHDs is achieved by using the Birks model.

The first measurements of energy-dependent light output from carbon recoils in the liquid organic scintillator EJ-309 were presented. For this measurement, neutrons were produced by an associated particle deuterium-tritium generator and scattered by a volume of EJ-309 scintillator into stop detectors positioned at four fixed angles. Carbon recoils in the scintillator were isolated using triple coincidence among the associated particle detector, scatter detector, and stop detectors. The kinematics of elastic and inelastic scatter allowed data collection at eight specific carbon recoil energies between 2.86 and 3.95 MeV. The light output caused by carbon recoils in this energy range is found to be approximately 1.14% of that caused by electrons of the same energy, which is comparable to the values reported for other liquid organic scintillators. The small pulse

height peaks of the carbon recoil measurement were used to refine previous estimates of detector resolution.

The application of semiempirical proton light output models and accurate carbon light output and resolution functions were shown to substantially improve agreement between simulated and experimental detector response of EJ-309 organic liquid scintillators. Neutrons produced during proton therapy were measured and used as a test case. Employing the light output and resolution functions developed in this work resulted in substantially improved agreement between simulation and measurement.

The improvements demonstrated in this dissertation have been adopted by my colleagues, and have improved several sets of their results. The Voltz semiempirical model was used to accurately simulate the light output from stilbene [78]; the Birks model was used to improve the agreement of simulations of radiation portal monitors [79]; the Birks light output data presented in Chapter 3 was used in the imaging reconstruction algorithms of the dual-particle imager [80–82]; the latest data are being used for ongoing work on the FNMC [8]; and semiempirical models are being explored for organic scintillator-based dosimeter work [52].

7.2.1 Current Best Estimate EJ-309 Detector Response Models

Table 7-1 presents the current best estimates for EJ-309 neutron light output, based on Chapters 3 and 4. Table 7-2 presents the new resolution coefficients found in Chapter 5.

Table 7-1. New recommended light output coefficients.

Detector Size	*Recoil*	*Form*	*a*	*b*
3x3	*Proton*	*Birks*	*1.903*	*26.03*
5x5	*Proton*	*Birks*	*2.277*	*33.84*
Any	*Carbon*	*Linear*	*0.01139*	

Table 7-2. New resolution coefficients.

Detector Size	*A*	*B*	*C*
3x3	*8.674*	*135.9*	*1043*
5x5	*9.639*	*123.2*	*1084*

7.3 Conclusion: Specific Problem, Revisited

In Chapter 1, Section 1.3, I showed two cases where discrepancies were noted between simulated and measured neutron PHDs, that served as the specific impetus for the work presented in this dissertation. This section summarizes the reduction of those discrepancies when the new models and coefficients are applied.

Figure 7-1 shows the simulated and measured PHDs for the case of ^{252}Cf spontaneous fission neutrons, measured with a 5 in. by 5 in. EJ-309 organic liquid scintillator. The simulated results using the original coefficients as well as the simulated results using the new coefficients are shown. Figure 7-2 shows the same data, in a fractional difference plot format. The changes are broken down further into two intermediate steps to allow the effect of each change to be seen.

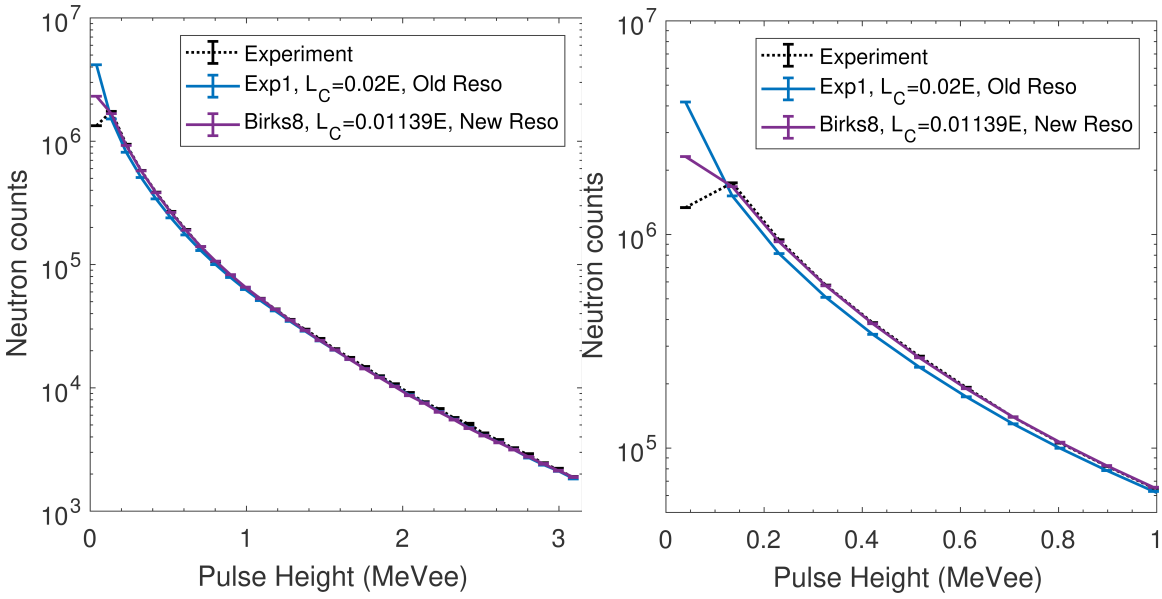

Figure 7-1 Simulated and measured PHDs, 5 in. by 5 in. EJ-309 detector, ^{252}Cf spontaneous fission neutron source. The second panel shows a zoomed in plot of the same data.

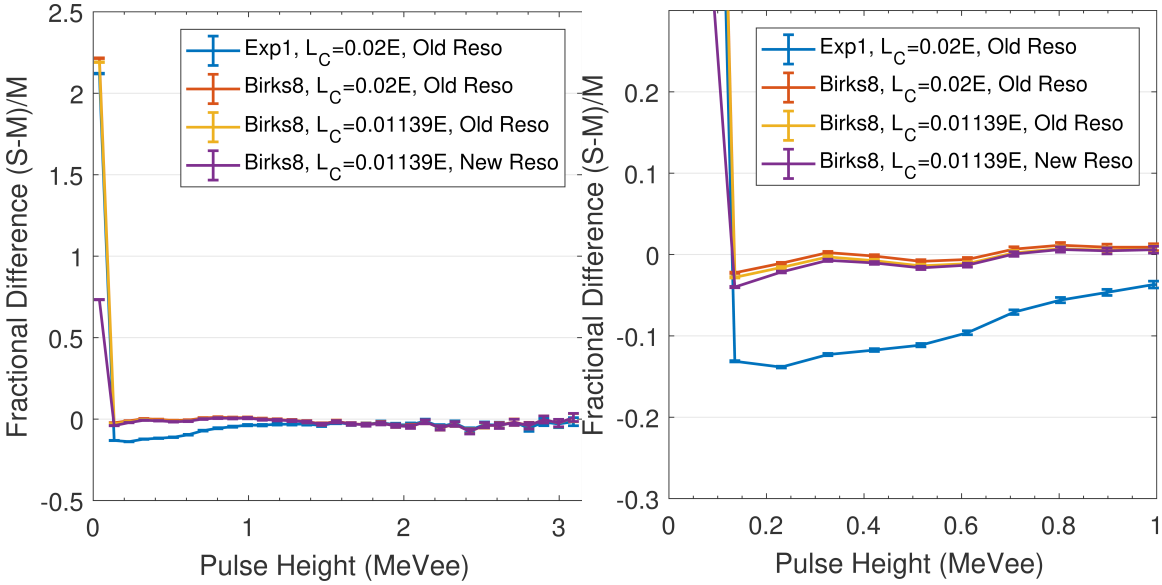

Figure 7-2 Fractional difference plot of simulated (S) and measured (M) PHDs, 5 in. by 5 in. EJ-309 detector, ^{252}Cf spontaneous fission neutron source. The second panel shows a zoomed in plot of the same data.

Figure 7-3 shows the simulated and measured PHDs for the case of secondary neutrons produced by 200-MeV protons incident on a soft tissue phantom, measured with a 3 in. by 3 in. EJ-309 organic liquid scintillator. The simulated results using the original coefficients as well as the simulated results using the new coefficients are shown. Figure

7-4 shows the same data, in a fractional difference plot format. The changes are broken down further into two intermediate steps to allow the effect of each change to be seen.

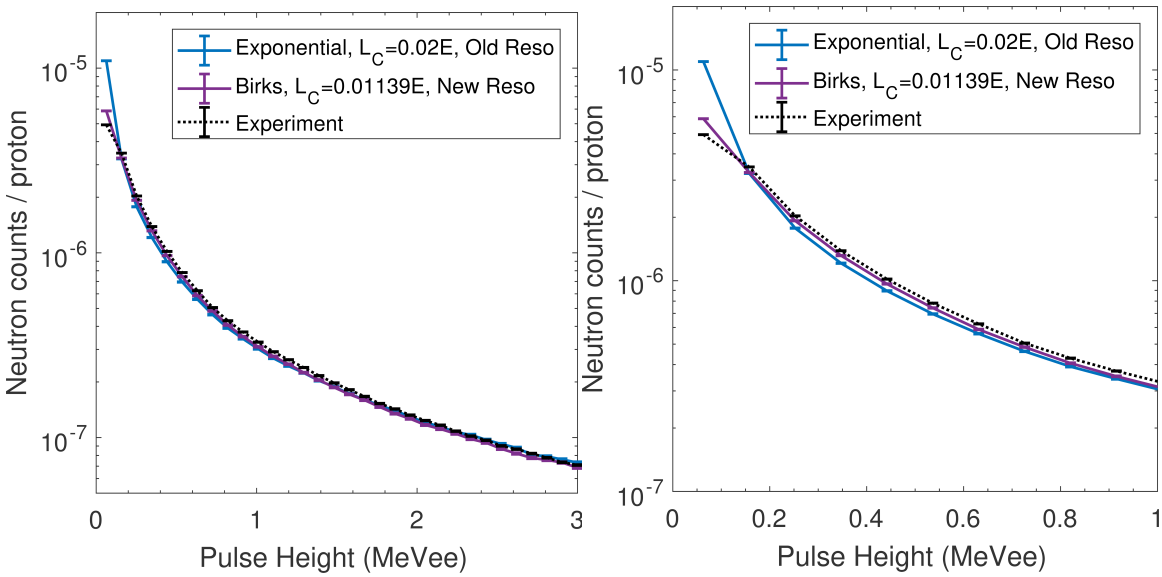

Figure 7-3 Simulated and measured PHDs, 3 in. by 3 in. EJ-309 detector, secondary neutrons produced by 200-MeV protons incident on a soft tissue phantom. The second panel shows a zoomed in plot of the same data.

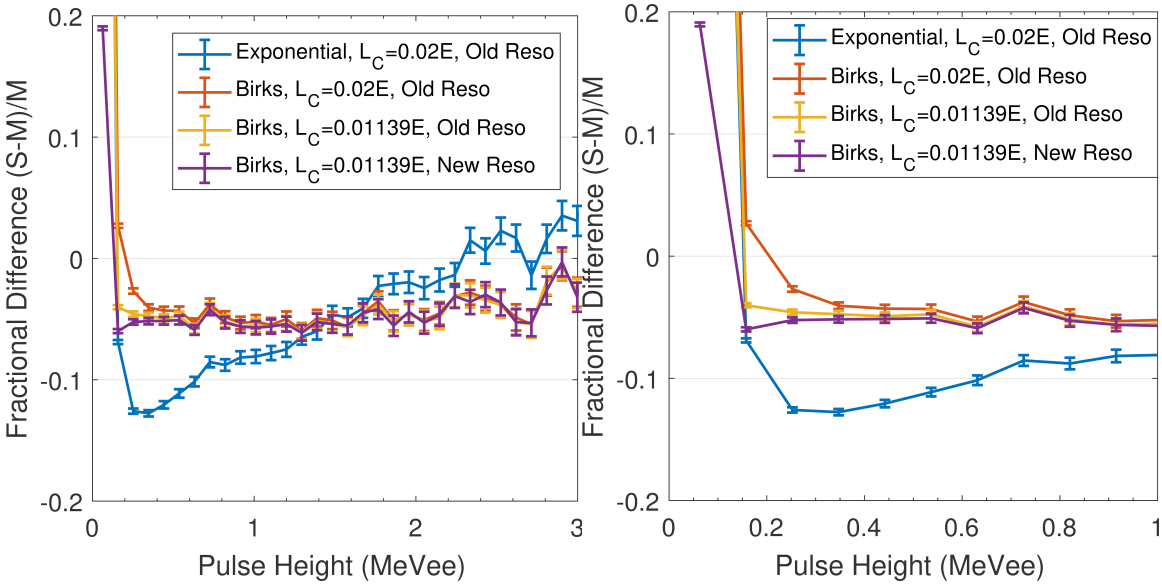

Figure 7-4. Fractional difference plot of simulated (S) and measured (M) PHDs, 3 in. by 3 in. EJ-309 detector, secondary neutrons produced by 200-MeV protons incident on a soft tissue phantom. The second panel shows a zoomed in plot of the same data.

Figures 7-1 through 7-4 clearly demonstrate that the new light output models and resolution coefficients developed in this research have a significant positive impact on the agreement of simulated and measured neutron PHDs in two significantly different cases. The biggest change and most significant improvement comes from applying the Birks semiempirical model for proton light output. Changing the carbon light coefficient and resolution function have effects that are more localized to the small pulse height regime. It can be seen that in the proton therapy case, the carbon light output change makes a bigger difference than in the ^{252}Cf case; this is consistent with the fact that the proton therapy case has much higher-energy neutrons available to create detectable pulses due to carbon interactions. It might be tempting to dismiss the carbon light output change as insignificant for safeguards applications, however, it is important to be as accurate as possible to improve confidence in the modeling of organic scintillators. Moreover, carbon light output could be important for future safeguards applications employing higher-energy neutrons (such as from D-T generators or nuclear reactions).

7.4 Future Work

In this section, I present suggestions for future work to build upon existing simulation capabilities for neutron detector response. Continuing to improve the accuracy of these simulations will bolster efforts to advance the state of the art in nuclear safeguards instrumentation.

7.4.1 MPPost Modifications

The MPPost tool, as modified to allow the use of the Birks and Voltz models, should be expanded in a few important ways.

Currently, using typical DNNG simulation settings, ^{12}C reactions such as $^{12}C(n, \alpha)^{9}Be$ are treated the same as carbon scatter reactions in the MPPost code. In other words, the value in the energy deposited column in the .d file is processed by the carbon recoil light equation. However, the light in these reactions would be produced by alpha particles and the recoiling ^{9}Be nucleus.

Fortunately, these reactions are not significant factors in most safeguards applications involving the detection of fission neutrons. The reaction thresholds are above 6 MeV, and the cross sections do not become significant until greater than 9 MeV. However, in D-T interrogation applications they could be important, and an effort should be made to properly account for them even as the high-energy tail of the fission spectrum.

MCNPX-PoliMi has an option on the RPOL card, RPOL(4)=1, that turns on charged particle fragments following neutron absorption reactions. This card, combined with existing alpha light output data from the literature (e.g. Verbinski) as an initial guess, would allow approximately accurate treatment of these reactions. Further work would be required to address the approximations, such as applying all of the light in the $^{12}C(n,n')3\alpha$ reaction to one alpha recoil instead of three.

7.4.2 Expanded Birks Models

A fit of the Birks model to the carbon light output data of Chapter 4 yielded coefficients that fit the data well, but likely do not extrapolate well. For example, the fitted *kB* value was negative, which is not expected from physical reasoning.

The literature contains several expansions on the Birks model, some of which are suggested to perform better for low-energy carbon data. For example, [18] presents a

model that treats the electronic and nuclear components of stopping power with separate terms, while other modifications include quadratic terms; these should be explored.

7.4.3 Additional Response Data Collection

The technique demonstrated in Chapter 4, and the model fitting and validation methods presented in Chapter 3, should be applied to other ongoing detector response characterization efforts, such as deuteron response for deuterated detectors, and stilbene anisotropy characterization. Additional data collection will be required, ideally using D-D and D-T neutron generators.

Bibliography

[1] L. Fishbone, L. Gallini, A. Krass, K. Myron, J. Sanborn, B. Ward, et al., Deterring Nuclear Proliferation: The Importance of IAEA Safeguards, 2013. https://www.bnl.gov/NNS/IAEAtextbook.php.

[2] U. Nations, Treaty on the Non-Proliferation of Nuclear Weapons, Off. Disarm. Aff. (1968). https://www.un.org/disarmament/wmd/nuclear/npt/ (accessed January 1, 2017).

[3] IAEA, IAEA Safeguards Leaflet, (2016). https://www.iaea.org/sites/default/files/16/08/iaea_safeguards_introductory_leaflet.pdf (accessed January 1, 2017).

[4] H.M.G. Nackaerts, IAEA Department of Safeguards Long-Term Strategic Plan (2012-2023), Vienna, 2013. https://www.bnl.gov/ISPO/docs/STR-375-IAEA-Safeguards-Long-Term-Plan.pdf.

[5] D. Henzlova, R. Kouzes, R. McElroy, P. Peerani, M. Aspinall, K. Baird, et al., Current Status of Helium-3 Alternative Technologies for Nuclear Safeguards, Los Alamos, NM (United States), 2015. doi:10.2172/1227248.

[6] J.L. Dolan, M. Flaska, A. Poitrasson-Riviere, A. Enqvist, P. Peerani, D.L. Chichester, et al., Plutonium measurements with a fast-neutron multiplicity counter for nuclear safeguards applications, Nucl. Instruments Methods Phys. Res. Sect. A Accel. Spectrometers, Detect. Assoc. Equip. 763 (2014) 565–574. doi:10.1016/j.nima.2014.06.028.

[7] D.L. Chichester, S.J. Thompson, M.T. Kinlaw, J.T. Johnson, J.L. Dolan, M. Flaska, et al., Statistical estimation of the performance of a fast-neutron multiplicity system for nuclear material accountancy, Nucl. Instruments Methods Phys. Res. Sect. A Accel. Spectrometers, Detect. Assoc. Equip. 784 (2015) 448–454. doi:10.1016/j.nima.2014.09.027.

[8] A. Di Fulvio, T.H. Shin, T. Jordan, C. Sosa, M.L. Ruch, S.D. Clarke, et al., Passive assay of plutonium metal plates using a fast-neutron multiplicity counter, Nucl. Instruments Methods Phys. Res. Sect. A Accel. Spectrometers, Detect. Assoc. Equip. 855 (2017) 92–101. doi:10.1016/j.nima.2017.02.082.

[9] M.G. Paff, M.L. Ruch, A. Poitrasson-Riviere, A. Sagadevan, S.D. Clarke, S. Pozzi, Organic liquid scintillation detectors for on-the-fly neutron/gamma alarming and radionuclide identification in a pedestrian radiation portal monitor, Nucl. Instruments Methods Phys. Res. Sect. A Accel. Spectrometers, Detect. Assoc. Equip. 789 (2015) 16–27. doi:10.1016/j.nima.2015.03.088.

[10] M.G. Paff, S.D. Clarke, S.A. Pozzi, Organic liquid scintillation detector shape and volume impact on radiation portal monitors, Nucl. Instruments Methods Phys. Res. Sect. A Accel. Spectrometers, Detect. Assoc. Equip. 825 (2016) 31–39. doi:10.1016/j.nima.2016.03.102.

[11] A. Poitrasson-Rivière, J.K. Polack, M.C. Hamel, D.D. Klemm, K. Ito, A.T. McSpaden, et al., Angular-resolution and material-characterization measurements for a dual-particle imaging system with mixed-oxide fuel, Nucl. Instruments Methods Phys. Res. Sect. A Accel. Spectrometers, Detect. Assoc. Equip. 797 (2015) 278–284. doi:10.1016/j.nima.2015.06.045.

[12] A. Poitrasson-Rivière, M.C. Hamel, J.K. Polack, M. Flaska, S.D. Clarke, S.A. Pozzi, Dual-particle imaging system based on simultaneous detection of photon and neutron collision events, Nucl. Instruments Methods Phys. Res. Sect. A Accel. Spectrometers, Detect. Assoc. Equip. 760 (2014) 40–45. doi:10.1016/j.nima.2014.05.056.

[13] A. Poitrasson-Rivière, B. a. Maestas, M.C. Hamel, S.D. Clarke, M. Flaska, S.A. Pozzi, et al., Monte Carlo investigation of a high-efficiency, two-plane Compton camera for long-range localization of radioactive materials, Prog. Nucl. Energy. 81 (2015) 127–133. doi:10.1016/j.pnucene.2015.01.009.

[14] M.L. Ruch, J. Nguyen, M. Flaska, S.A. Pozzi, Time Resolution of Stilbene Coupled to Silicon Photomultipliers for use in a Handheld Dual Particle Scatter Camera, in: 2015 IEEE Nucl. Sci. Symp. Med. Imaging Conf., 2015.

[15] M.L. Ruch, Silicon Photomultipliers for Compact Neutron ScatterCameras, University of Michigan, 2017.

[16] M.A. Norsworthy, A. Poitrasson-Rivière, M.L. Ruch, S.D. Clarke, S.A. Pozzi, Evaluation of neutron light output response functions in EJ-309 organic scintillators, Nucl. Instruments Methods Phys. Res. Sect. A Accel. Spectrometers, Detect. Assoc. Equip. 842 (2017) 20–27. doi:10.1016/j.nima.2016.10.035.

[17] S.D. Clarke, E. Pryser, B.M. Wieger, S.A. Pozzi, R.A. Haelg, V.A. Bashkirov, et al., A scintillator-based approach to monitor secondary neutron production during proton therapy, Med. Phys. 43 (2016) 5915–5924. doi:10.1118/1.4963813.

[18] S. Yoshida, T. Ebihara, T. Yano, A. Kozlov, T. Kishimoto, I. Ogawa, et al., Light output response of KamLAND liquid scintillator for protons and 12C nuclei, Nucl. Instruments Methods Phys. Res. Sect. A Accel. Spectrometers, Detect. Assoc. Equip. 622 (2010) 574–582. doi:10.1016/j.nima.2010.07.087.

[19] J. Hong, W.W. Craig, P. Graham, C.J. Hailey, N.J.C. Spooner, D.R. Tovey, The scintillation efficiency of carbon and hydrogen recoils in an organic liquid scintillator for dark matter searches, Astropart. Phys. 16 (2002) 333–338. doi:10.1016/S0927-6505(01)00114-1.

[20] H. Sekiya, M. Minowa, Y. Shimizu, Y. Inoue, W. Suganuma, Measurements of anisotropic scintillation efficiency for carbon recoils in a stilbene crystal for dark matter detection, Phys. Lett. Sect. B Nucl. Elem. Part. High-Energy Phys. 571

(2003) 132–138. doi:10.1016/j.physletb.2003.07.077.

[21] V.I. Tretyak, Semi-empirical calculation of quenching factors for ions in scintillators, Astropart. Phys. 33 (2010) 40–53. doi:10.1016/j.astropartphys.2009.11.002.

[22] E. Technology, EJ-301/EJ-309 Product Website, EJ-301/EJ-309 Prod. Website. (2017). http://www.eljentechnology.com/products/liquid-scintillators/ej-301-ej-309.

[23] G.F. Knoll, Radiation Detection and Measurement, Fourth, John Wiley & Sons, 2010.

[24] J.B. Birks, The Theory and Practice of Scintillation Counting, Pergamon Press Ltd., 1964.

[25] J.F. Ziegler, SRIM-2013, SRIM-2013. (2013). srim.org.

[26] J.F. Ziegler, J.P. Biersack, M.D. Ziegler, SRIM: The Stopping and Range of Ions in Matter, 15th Ed., 2015.

[27] NIST, ESTAR: Stopping-power and Range Tables for Electrons, ESTAR: Stopping-Power and Range Tables for Electrons. (2015). physics.nist.gov/PhysRefData/Star/Text/ESTAR.html.

[28] F.D. Brooks, Development of organic scintillators, Nucl. Instruments Methods. 162 (1979) 477–505. doi:10.1016/0029-554X(79)90729-8.

[29] E. King, M. Norsworthy, S. Clarke, S. Pozzi, Pulse Shape Fitting for Pulse Shape Discrimination and Light Output Applications Emily King, Mark Norsworthy, Shaun Clarke, Sara Pozzi, (n.d.).

[30] J.K. Polack, M. Flaska, A. Enqvist, C.S. Sosa, C.C. Lawrence, S.A. Pozzi, An algorithm for charge-integration, pulse-shape discrimination and estimation of neutron/photon misclassification in organic scintillators, Nucl. Instruments Methods Phys. Res. Sect. A Accel. Spectrometers, Detect. Assoc. Equip. 795 (2015) 253–267. doi:10.1016/j.nima.2015.05.048.

[31] A. Enqvist, C.C. Lawrence, B.M. Wieger, S.A. Pozzi, T.N. Massey, Neutron light output response and resolution functions in EJ-309 liquid scintillation detectors, Nucl. Instruments Methods Phys. Res. Sect. A Accel. Spectrometers, Detect. Assoc. Equip. 715 (2013) 79–86. doi:10.1016/j.nima.2013.03.032.

[32] S.A. Pozzi, E. Padovani, M. Marseguerra, MCNP-PoliMi: A Monte-Carlo code for correlation measurements, Nucl. Instruments Methods Phys. Res. Sect. A Accel. Spectrometers, Detect. Assoc. Equip. 513 (2003) 550–558. doi:10.1016/j.nima.2003.06.012.

[33] S.A. Pozzi, S.D. Clarke, W.J. Walsh, E.C. Miller, J.L. Dolan, M. Flaska, et al., MCNPX-PoliMi for nuclear nonproliferation applications, Nucl. Instruments Methods Phys. Res. Sect. A Accel. Spectrometers, Detect. Assoc. Equip. 694 (2012) 119–125. doi:10.1016/j.nima.2012.07.040.

[34] E.C. Miller, S.D. Clarke, M. Flaska, S.A. Pozzi, E. Padovani, MCNPX-PoliMi Post-processing Algorithm for Detector Response Simulations, J. Nucl. Mater. Manag. 40 (2012).

[35] S.A. Pozzi, E. Padovani, M. Marseguerra, MCNP-PoliMi: A Monte-Carlo code for correlation measurements, Nucl. Instruments Methods Phys. Res. Sect. A Accel. Spectrometers, Detect. Assoc. Equip. 513 (2003) 550–558. doi:10.1016/j.nima.2003.06.012.

[36] M. Marseguerra, E. Padovani, S.A. Pozzi, M. Da Ros, Phenomenological simulation of detector response for safeguards experiments, Nucl. Instruments Methods Phys. Res. Sect. B Beam Interact. with Mater. Atoms. 213 (2004) 289–293. doi:10.1016/S0168-583X(03)01620-3.

[37] K. Roemer, G. Pausch, C.-M. Herbach, Y. Kong, R. Lentering, C. Plettner, et al., A technique for measuring the energy resolution of low-Z scintillators, 2009 IEEE Nucl. Sci. Symp. Conf. Rec. (2009) 6–11. doi:10.1109/NSSMIC.2009.5401909.

[38] R.C. Byrd, W.T. Urban, LA-12833-MS: Calculations of the Neutron Response of Boron-Loaded Scintillators, 1994.

[39] R.J. Kurz, UCRL-11339: A 709/7090 Fortran II Program to Compute the Neutron-Detection Efficiency of Plastic Scintillator for Neutron Energies from 1 to 300 MeV, Berkeley, CA, 1964.

[40] R. Voltz, J. Lopes da Silva, G. Laustriat, A. Coche, Influence of the Nature of Ionizing Particles on the Specific Luminescence of Organic Scintillators, J. Chem. Phys. 45 (1966) 3306–3311. doi:10.1063/1.1728106.

[41] S.P. Ahlen, B.G. Cartwright, G. Tarlé, Return to unsaturated response of polymeric scintillators excited by relativistic heavy ions, Nucl. Instruments Methods. 147 (1977) 321–328. doi:10.1016/0029-554X(77)90264-6.

[42] R.L. Craun, D.L. Smith, Analysis of response data for several organic scintillators, Nucl. Instruments Methods. 80 (1970) 239–244. doi:10.1016/0029-554X(70)90768-8.

[43] N. V. Kornilov, I. Fabry, S. Oberstedt, F.J. Hambsch, Total characterization of neutron detectors with a 252Cf source and a new light output determination, Nucl. Instruments Methods Phys. Res. Sect. A Accel. Spectrometers, Detect. Assoc. Equip. 599 (2009) 226–233. doi:10.1016/j.nima.2008.10.032.

[44] MATLAB and Curve Fitting Toolbox Release 2016a, The MathWorks, Inc., Natick, Massachusetts, United States, (2016).

[45] M. Takada, K. Yajima, S. Kamada, Simulated Neutron Response Functions of Phoswich-Type Neutron Detector and Thin Organic Liquid Scintillator, Aesj.or.Jp. 2 (2011) 274–279. http://www.aesj.or.jp/publication/pnst002/data/274-279.pdf.

[46] R. Madey, F.M. Waterman, A.R. Baldwin, J.N. Knudson, J.D. Carlson, J. Rapaport, The response of NE-228A, NE-228, NE-224, and NE-102 scintillators to protons from 2.43 to 19.55 MeV, Nucl. Instruments Methods. 151 (1978) 445–

450. doi:10.1016/0029-554X(78)90154-4.

[47] L.F. Miller, J. Preston, S. Pozzi, M. Flaska, J. Neal, Digital pulse shape discrimination, Radiat. Prot. Dosimetry. 126 (2007) 253–255. doi:10.1093/rpd/ncm052.

[48] V.V. Verbinski, W.R. Burrus, T.A. Love, W. Zobel, N.W. Hill, R. Textor, Calibration of an organic scintillator for neutron spectrometry, Nucl. Instruments Methods. 65 (1968) 8–25. doi:10.1016/0029-554X(68)90003-7.

[49] G. Dietze, H. Klein, Gamma-calibration of NE 213 scintillation counters, Nucl. Instruments Methods. 193 (1982) 549–556. doi:10.1016/0029-554X(82)90249-X.

[50] M.A. Norsworthy, M.L. Ruch, M.C. Hamel, S.D. Clarke, P.A. Hausladen, S.A. Pozzi, Light Output Response of EJ-309 due to Neutron Elastic and Inelastic Scatter on Carbon, Submitt. Publ. (2017).

[51] J. Hong, W.W. Craig, P. Graham, C.J. Hailey, N.J.C. Spooner, D.R. Tovey, The scintillation efficiency of carbon and hydrogen recoils in an organic liquid scintillator for dark matter searches, Astropart. Phys. 16 (2002) 333–338. doi:10.1016/S0927-6505(01)00114-1.

[52] C.A. Miller, M.A. Norsworthy, S.D. Clarke, S.A. Pozzi, R.W. Schulte, Scintillator-based Measurement of off-Axis Neutron and Photon Dose Rates during Proton Therapy, in: IEEE Med. Imaging Conf., Strasbourg, France, 2016.

[53] V.V. Verbinski, J.C. Courtney, W.R. Burrus, T.A. Love, The Response of Some Organic Scintillators to Fast Neutrons, in: J. Greenborg (Ed.), Proc. Spec. Sess. Fast Neutron Spectrosc., American Nuclear Society, San Francisco, CA, 1964.

[54] C.C. Lawrence, M. Febbraro, T.N. Massey, M. Flaska, F.D. Becchetti, S.A. Pozzi, Neutron response characterization for an EJ299-33 plastic scintillation detector, Nucl. Instruments Methods Phys. Res. Sect. A Accel. Spectrometers, Detect. Assoc. Equip. 759 (2014) 16–22. doi:10.1016/j.nima.2014.04.062.

[55] A. Tomanin, J. Paepen, P. Schillebeeckx, R. Wynants, R. Nolte, A. Lavietes, Characterization of a cubic EJ-309 liquid scintillator detector, Nucl. Instruments Methods Phys. Res. Sect. A Accel. Spectrometers, Detect. Assoc. Equip. 756 (2014) 45–54. doi:10.1016/j.nima.2014.03.028.

[56] F. Pino, L. Stevanato, D. Cester, G. Nebbia, L. Sajo-Bohus, G. Viesti, The light output and the detection efficiency of the liquid scintillator EJ-309., Appl. Radiat. Isot. 89 (2014) 79–84. doi:10.1016/j.apradiso.2014.02.016.

[57] R. Batchelor, W.B.B. Gilboy, J.B.B. Parker, J.H.H. Towle, The response of organic scintillators to fast neutrons, Nucl. Instruments Methods. 13 (1961) 70–82. doi:10.1016/0029-554X(61)90171-9.

[58] M.F. Steuer, B.E. Wenzel, Carbon recoil detection and the response of organic scintillators in C12(n,n)C12 scattering, Nucl. Instruments Methods. 33 (1965) 131–135. doi:10.1016/0029-554X(65)90226-0.

[59] N. Soppera, M. Bossant, E. Dupont, JANIS 4: An improved version of the NEA Java-based nuclear data information system, Nucl. Data Sheets. 120 (2014) 294–296. doi:10.1016/j.nds.2014.07.071.

[60] C.C. Lawrence, A. Enqvist, M. Flaska, S.A. Pozzi, A.M. Howard, J.J. Kolata, et al., Nuclear Instruments and Methods in Physics Research A Response characterization for an EJ315 deuterated organic-liquid scintillation detector for neutron spectroscopy, Nucl. Inst. Methods Phys. Res. A. 727 (2013) 21–28. doi:10.1016/j.nima.2013.05.172.

[61] E. Technology, Response of EJ-301 Liquid Scintillator, Response EJ-301 Liq. Scintill. (2017). http://www.eljentechnology.com/images/technical_library/EJ301_Resp.pdf.

[62] J.K. Shultis, R.E. Faw, Radiation Shielding, Prentice Hall, Upper Saddle River, NJ, 1996.

[63] D.B. Pelowitz, MCNPX User's Manual Version 2.7.0, Los Alamos, NM (United States), 2011.

[64] L.F. Miller, J. Preston, S.A. Pozzi, M. Flaska, J. Neal, Digital pulse shape discrimination, Radiat. Prot. Dosimetry. 126 (2007) 253–255. doi:10.1093/rpd/ncm052.

[65] K. Shibata, O. Iwamoto, T. Nakagawa, N. Iwamoto, A. Ichihara, S. Kunieda, et al., JENDL-4.0: A New Library for Nuclear Science and Engineering, J. Nucl. Sci. Technol. 48 (2011) 1–30. doi:10.1080/18811248.2011.9711675.

[66] M.B. Chadwick, M. Herman, P. Obložinský, M.E. Dunn, Y. Danon, A.C. Kahler, et al., ENDF/B-VII.1 Nuclear Data for Science and Technology: Cross Sections, Covariances, Fission Product Yields and Decay Data, Nucl. Data Sheets. 112 (2011) 2887–2996. doi:10.1016/j.nds.2011.11.002.

[67] G. Börker, W. Mannhart, B.R.L. Siebert, Elastic and Inelastic Neutron Scattering on Carbon-12, in: S.M. Qaim (Ed.), Proc. Int. Conf. Nucl. Data Sci. Technol., Springer Berlin Heidelberg, Jülich, Germany, 1991: pp. 317–319. doi:10.1007/978-3-642-58113-7_90.

[68] G. Haouat, J. Lachkar, J. Sigaud, Y. Patin, F. Coçu, CEA-R-4641 - Differential Cross Sections for Carbon Neutron Elastic and Inelastic Scattering from 8,0 to 14,5 MeV, Centre d'Etudes de Bruyères-le-Châtel, 1975. https://www.ipen.br/biblioteca/rel/R35241.pdf.

[69] D.H. Kim, C.-S. Gil, Y.-O. Lee, Current Status of ACE Format Libraries for MCNP at Nuclear Data Center of KAERI, ISORD-8", in: 8th Int. Symp. Radiat. Detect. Saf. Detect. Technol., Jeju, Korea, 2015. http://atom.kaeri.re.kr/applibs/1_KN-Lib/reference/app_JENDL_a_KNJ40/DHKim,ISORD-8,ppt,Jul,2015.pdf.

[70] M. Drosg, DROSG-2000, Codes and database for 60 neutron source reactions, documented in the IAEA report IAEA-NDS-87 Rev. 10 (January 2016),

downloaded from the homepage of IAEA Nuclear Data Section., n.d.

[71] P. Schuster, E. Brubaker, Investigating the Anisotropic Scintillation Response in Anthracene through Neutron, Gamma-Ray, and Muon Measurements, IEEE Trans. Nucl. Sci. 63 (2016) 1942–1954. doi:10.1109/TNS.2016.2542589.

[72] S. Matsumoto, Y. Koba, R. Kohno, C. Lee, W.E. Bolch, M. Kai, Secondary Neutron Doses to Pediatric Patients During Intracranial Proton Therapy, Health Phys. 110 (2016) 380–386. doi:10.1097/HP.0000000000000461.

[73] C. Zacharatou Jarlskog, C. Lee, W.E. Bolch, X.G. Xu, H. Paganetti, Assessment of organ-specific neutron equivalent doses in proton therapy using computational whole-body age-dependent voxel phantoms., Phys. Med. Biol. 53 (2008) 693–717. doi:10.1088/0031-9155/53/3/012.

[74] S. Garwicz, H. Anderson, J.H. Olsen, H. Døllner, H. Hertz, G. Jonmundsson, et al., Second malignant neoplasms after cancer in childhood and adolescence: a population-based case-control study in the 5 Nordic countries. The Nordic Society for Pediatric Hematology and Oncology. The Association of the Nordic Cancer Registries., Int. J. Cancer. 88 (2000) 672–8. http://www.ncbi.nlm.nih.gov/pubmed/11058888.

[75] H. Paganetti, ed., Proton Therapy Physics, CRC/Taylor & Francis, Boca Raton, FL, 2012.

[76] C.A. Miller, S.D. Clarke, S.A. Pozzi, WE-AB-BRB-11: Portable Fast Neutron and Photon Dose Meter, Med. Phys. 42 (2015) 3652–3652. doi:10.1118/1.4925852.

[77] H.S. Stoker, General, Organic, and Biological Chemistry, 6, revised ed., Cengage Learning, 2012.

[78] M.M. Bourne, S.D. Clarke, M. Paff, A. DiFulvio, M. Norsworthy, S.A. Pozzi, Digital pile-up rejection for plutonium experiments with solution-grown stilbene, Nucl. Instruments Methods Phys. Res. Sect. A Accel. Spectrometers, Detect. Assoc. Equip. 842 (2017) 1–6. doi:10.1016/j.nima.2016.10.023.

[79] M.G. Paff, Organic Scintillation Detectors for Spectroscopic Radiation Portal Monitors, University of Michigan, 2017. doi:10.13140/RG.2.2.25287.29605.

[80] A.P.V. Poitrasson-Rivière, Development of a Dual-Particle Imaging System for Nonproliferation Applications, University of Michigan, 2016. http://hdl.handle.net/2027.42/120727.

[81] J.K. Polack, A Maximum-Likelihood Approach for Localizing and Characterizing Special Nuclear Material with a Dual-Particle Imager, University of Michigan, 2016. http://hdl.handle.net/2027.42/133291.

[82] M.C. Hamel, A stochastic imaging technique for spatio-spectral characterization of special nuclear material, University of Michigan, 2017.